Dipl.-Ing. Klaus Allmaier

Computation of neoclassical transport in stellarators using a Monte Carlo method with reduced variance

DOCTORAL THESIS

to achieve the university degree of

Doktor der technischen Wissenschaften

submitted to

Graz University of Technology

Supervisor

Ao.Univ.-Prof. Dipl.-Ing. Dr.phil. Martin Heyn

Institute of Theoretical and Computational Physics

Co-Supervisor:
Ass.Prof. Dipl.-Ing. Dr.techn. Winfried Kernbichler

Graz, March 2017

AFFIDAVIT

I declare that I have authored this thesis independently, that I have not used other than the declared sources/resources, and that I have explicitly indicated all material which has been quoted either literally or by content from the sources used. The text document uploaded to TUGRAZonline is identical to the present doctoral thesis.

Date

Signature

Abstract

In this work a specific δf Monte Carlo method for the computation of neoclassical transport coefficients related to the bootstrap current, the radial particle transport and the parallel conductivity in stellarators has been developed. Those three mono-energetic transport coefficients, which are flux-surface-averaged moments of solutions to the linearized drift kinetic equation, are needed for a complete neoclassical description of stellarator plasmas. The bootstrap current can affect the equilibrium, the stability and the confinement properties of a stellarator and therefore the development of an improved method for its evaluation is of special interest. Existing methods either have big statistical errors in the computations or introduce a bias in the results if they use filtering techniques (limitation of the radial test particle motion by an annulus). Usually, these methods only have a good convergence for tokamaks where the variance of all transport coefficients has no strong dependence on the plasma collisionality. In stellarators the varying magnetic field strength along the field lines causes a fraction of the particles to be trapped in helical ripples of the magnetic field due to the magnetic mirror effect. These particles can be displaced far from their original flux surfaces between collisions and give rise to plasma currents as well as to enhanced particle and energy transport. The minimization of this so-called neoclassical transport is a requirement for the optimization of stellarators. The method developed in this work allows to compute transport coefficients with low statistical errors and without introducing a bias due to the usage of filtering techniques. This is achieved by combining a standard δf method with an algorithm employing constant particle weights and re-discretizations of the test particle distribution in phase space. The developed method allows for simultaneous computations of bootstrap and diffusion coefficients which is not possible with existing methods if they use filtering techniques. Results of computations stay in good agreement with results from other codes in various non-axisymmetric magnetic field configurations and new results have been obtained for confinement regimes which have hardly or not at all been accessible with existing methods.

Kurzfassung

In dieser Arbeit wurde eine spezielle δf Monte Carlo Methode für die Berechnung neoklassischer Transportkoeffizienten (Bootstrapstromkoeffizient, Diffusionskoeffizient und Leitfähigkeitskoeffizient) in Stellaratoren entwickelt. Diese drei mono-energetischen Transportkoeffizienten sind über die Flussflächen gemittelte Momente von Lösungen der linearisierten Driftkinetischen Gleichung und deren Berechnung ist eine Voraussetzung für eine vollständige neoklassische Beschreibung von Stellarator Plasmen. Der Bootstrapstrom beeinflusst die Gleichgewichts-, Stabilitäts- und Einschlusseigenschaften einer Konfiguration, daher ist die Entwicklung einer leistungsfähigen Methode für seine Berechnung von großem Interesse für die Optimierung von Stellaratoren. Existierende Methoden weisen entweder große statistische Fehler in den Resultaten auf oder führen systematische Fehler in die Berechnungen ein wenn Filtertechniken (Einschränkung der Testteilchenbewegung auf einen radial begrenzten Bereich) verwendet werden. Diese Methoden haben gewöhnlich nur für Tokamaks ein gutes Konvergenzverhalten, weil dort die Varianz aller Transportkoeffizienten keine starke Abhängigkeit vom Kollisionsparameter aufweist. Durch die entlang der Feldlinien variierende magnetische Feldstärke wird in Stellaratoren ein Teil der Teilchen in helikalen Rippeln des magnetischen Feldes aufgrund des magnetischen Spiegeleffektes gefangen. Diese Teilchen können sich zwischen den Stößen weit von den ursprünglichen Flussflächen entfernen und verursachen sowohl Ströme im Plasma als auch erhöhten Teilchen- und Energietransport. Die Minimierung dieses sogenannten neoklassischen Transportes ist eine Voraussetzung für die Optimierung von Stellaratoren. Die in dieser Arbeit entwickelte Methode ermöglicht die numerische Berechnung von Transportkoeffizienten mit kleinen statistischen Fehlern und ohne systematische Fehler von Filtertechniken. Dabei wird eine Standard δf Methode mit einem Algorithmus kombiniert, der auf der Verwendung von konstanten Teilchengewichten und Re-Diskretisierungen der Testteilchenverteilung im Phasenraum beruht. Die Methode erlaubt die gleichzeitige Berechnung von Bootstrap- und Diffusionskoeffizienten, dies ist mit herkömmlichen Methoden die

Filtertechniken verwenden nicht möglich. Die Ergebnisse der Berechnungen für verschiedene nicht-axisymmetrische magnetische Konfigurationen stimmen mit den Resultaten anderer Methoden gut überein und neue Ergebnisse wurden für Einschlussregime erhalten, die mit herkömmlichen Methoden nur unter großem numerischen Aufwand oder überhaupt nicht berechenbar waren.

Chaos often breeds life,
when order breeds habit

Henry Brooks Adams, 1838-1918

Acknowledgments

This work could never have been completed without the support, advice, assistance and encouragement of the following people:

First of all I would like to thank my supervisor *Prof. Dr. Martin Heyn* and my co-supervisor *Prof. Dr. Winfried Kernbichler* who gave me the opportunity to perform this research, for supervising my thesis, for stimulating discussions and for hints and help at any stage of this work.

I would like to express my sincere gratitude to *Dr. Sergei V. Kasilov* for his enormously valuable ideas and inputs at all stages of this work, for many fruitful discussions and comments, for answering many questions and for giving me insights into plasma physics also far beyond the scope of this work.

I want to thank my colleagues at the institute *Dr. Georg Leitold*, *Dr. Bernhard Seiwald* and *Dr. Andreas Martitsch* for many discussions on physical topics, for hints and help with computer problems and for the good atmosphere at the institute.

Many thanks to *Andreas Hirczy* for providing the computer infrastructure at the institute which I extensively used for the computations in this work.

I would like to thank the Association between EURATOM and the Austrian Academy of Sciences (ÖAW) as well as the Austrian Science Fund (FWF) for funding this research.

I am very grateful to *Prof. Dr. Theo Neger* and *Prof. Dr. Klaus Schöpf* for serving on my thesis committee.

Contents

Chapter 1

Introduction

Stellarators are devices which aim to confine hot plasmas with non-axisymmetric magnetic fields in order to sustain controlled nuclear fusion reactions. The magnetic fields necessary to confine the plasma are completely generated by external coils but can be modified by internal equilibrium currents such as the so-called bootstrap current. The evaluation of transport coefficients associated to this current has been a key issue of this work. Also, the computation of transport coefficients related to the radial particle transport and to the parallel conductivity for various magnetic configurations has been a goal of this thesis. The main task of this PhD work has been the development of the code NEO-MC which computes the normalized mono-energetic bootstrap current coefficient, the mono-energetic radial diffusion coefficient and the mono-energetic parallel conductivity coefficient in various confinement regimes relevant for fusion experiments. Parts of this thesis have been published in Ref. [1].

The toroidal curvature of the confining magnetic fields in stellarators gives rise to plasma currents as well as to enhanced particle and energy transport (the so-called neoclassical transport). In order to analyse measurements and experimental results, to carry out predictive simulations and to improve the confinement behaviour of a device it is essential to evaluate the neoclassical transport properties of a configuration. The minimization of this transport is a requirement for the optimization of stellarators. Typically, a large number of toroidal and poloidal modes contribute to the magnetic field spectrum in stellarators and causes complicated magnetic field geometries. Particles trapped in local magnetic field ripples give rise to enhanced neoclassical transport. The three-dimensional geometry in stellarators allows for sophisticated constructions and various possibilities for optimizations of the configurations, on the other hand the analytical and numerical modeling becomes more difficult due to the missing symmetry. Kinetic processes in plasmas can be modeled with particle simulations where the distribution function is defined as the particle density in phase space. Following the orbits of plasma particles allows to compute the distribution function itself as well as a variety of macroscopic parameters of the plasma. Usually, this can be achieved with a relatively small number of test particles. Nevertheless, this number has to be big enough to make sure that each "elementary" volume of phase space is covered with an adequate number of test particles. The elementary volumes should be small compared to the scale of the distribution function but not too small in order to keep the total number of simulation particles within a reasonable range [2].

Full f Monte Carlo codes typically have a low efficiency when calculating plasma currents as they compute the total distribution function rather than computing just the part of the distribution function which is relevant for the currents. A variety of so-called δf Monte Carlo methods [3–10] which directly address to the computation of the perturbation of the distribution function is used for the numerical modeling in stellarators (as well as in tokamaks where the modeling is considerably facilitated due to symmetries in the magnetic field geometry). These methods solve the linearized drift-kinetic equation and compute the evolution of the particles in a series of subsequent time steps by changing the pitch parameters in accordance with a Monte Carlo model of the Lorentz collision operator and by integrating the particle drift equations over time in order to update the positions and momenta of the particles. In tokamaks the variance of all transport coefficients including the bootstrap coefficient does not strongly depend on the plasma collisionality. There, the original δf method [3] (this method is named below "standard δf method") has a good convergence for the computation of all transport coefficients. However, if this method is applied to stellarators, the variance of the bootstrap coefficient increases as a square of the mean free path because large random contributions to the test particle weights are accumulated in phase space regions occupied by trapped particles. In the standard δf method the test particle weight is defined by the test particle displacement from the magnetic surface where transport coefficients are computed. Particles with large weights are trapped particles with a finite bounce averaged radial drift velocity. These particles can make large radial displacements far away from their original flux surfaces in the long mean free path regime. In order to avoid the problem of large noise in the bootstrap coefficient there have been methods developed (see e.g. Ref. [7]) which filter out those particles which acquire large weights and replace them by particles with zero weight. In these computations particles with large deviations from the magnetic surface are put back to this original surface. In order to do so an annulus is introduced which limits the radial movement of the particles. The radial size of this annulus has to be much smaller than the displacement of a trapped particle during a collision time. Although this procedure improves the convergence in computations of the bootstrap coefficient significantly it is unsatisfactory because it introduces a bias in the results which has to be checked additionally.

In this work a method with reduced variance which overcomes this problem has been developed. The standard δf method is combined with an algorithm employing constant particle weights and re-discretizations of the test particle distribution in phase space. This method is formally free of bias introduced by particle filters and allows to compute bootstrap coefficients and diffusion coefficients simultaneously which is not possible with methods which use filtering techniques. Results for various confinement regimes are presented for different stellarator configurations. A part of the results and results from benchmarking with other methods have been published in Ref. [11–23]. For the numerical computations the Fortran code NEO-MC has been developed which can be run on batch systems, e.g. Condor, as well as on parallel clusters, e.g. MPI (Message Passing Interface). NEO-MC is an effective tool for computations in new fusion experiments (e.g. W7-X [24] which is currently in the start-up phase at Greifswald, Germany) as well as for existing experiments where other methods did not provide satisfying results (e.g. TJ-II [25], in operation at Madrid, Spain). Research activities in plasma physics with regard to fusion are basically not stand-alone projects. The numerical simulation of various aspects of plasma confinement in toroidal devices is of wide interest for stellarator research in universities and research centers within Europe and worldwide. Several collaborations exist between the plasma physics group of the Institut für Theoretische Physik – Computational Physics at TU Graz and institutions such as, e.g., the IPP in Germany or the research center CIEMAT in Spain. The last one employs the code NEO-MC for the creation of a neoclassical database.

The structure of the thesis is as follows. In chapter 2 a brief introduction to stellarators is given. The most common stellarator confinement concepts as well as the advantages and difficulties of stellarators are presented. In chapter 3 an introduction to neoclassical transport theory is given and the drift kinetic equation, which is one of the fundamental equations in neoclassical transport theory, as well as thermodynamical forces, neoclassical fluxes and neoclassical transport coefficients are presented. In chapter 4 a brief description of a full f method is given which has been tested at the beginning of this work and shown to give unsatisfactory results with huge error bars. In chapter 5 the standard δf method is discussed and some drawbacks of its application in stellarators are outlined. It is shown how to formulate the δf method in the form of an integral equation. This is equivalent to the usual formulation of the δf Monte Carlo method and provides the advantage for a direct use of various variance reduction methods which are usually applied to integral equations. In chapter 6 an advanced δf method is described which uses a new algorithm. This method achieves a considerable reduction of statistical errors by employing constant particle weights and re-discretizations of the particle distribution function. In chapter 7 the code NEO-MC is presented and results of computations for general confinement regimes are shown for different types of stellarators. In the Appendices an outlook on further possibilities of the method developed in this work can be found. An overview of the steps necessary to implement a linearized Coulomb collision operator in the procedure is given. For a further improvement of the computation efficiency of neoclassical transport coefficients a δf method for the implementation in the Stochastic Mapping Technique [2] is outlined. A conclusion and a summary of the work can be found in chapter 8.

1.1 Publications

In this section the articles contributed to peer reviewed journals, to European Physical Society conferences and to International Stellarator Heliotron Workshops authored and co-authored by the author of this thesis are presented.

1.1.1 Peer reviewed journal articles

- K. Allmaier, S. V. Kasilov, W. Kernbichler and G. O. Leitold, Variance reduction in computations of neoclassical transport in stellarators using a δf method, Phys. Plasmas 15, 072512–1–072512–8, 2008.

- W. Kernbichler, S. V. Kasilov, G. O. Leitold, V. V. Nemov and K. Allmaier, Recent progress in NEO-2 - A code for neoclassical transport computations based on field line tracing, Plasma and Fusion Research 3, S1061–1–S1061–4, 2008.

- C. D. Beidler, K. Allmaier, M. Yu. Isaev, S. V. Kasilov, W. Kernbichler, G. O. Leitold, H. Maaßberg, D. R. Mikkelsen, S. Murakami, M. Schmidt, D. A. Spong, V. Tribaldos and A. Wakasa, Benchmarking Results From the International Collaboration on Neoclassical Transport in Stellarators ICNTS, Nucl. Fusion 51, 076001–1–076001–28, 2011.

- J. L. Velasco, K. Allmaier, A. López-Fraguas, C. D. Beidler, H. Maaßberg, W. Kernbichler and F. Castejón, Calculation of the bootstrap current profile for the stellarator TJ-II, Plasma Phys. Control. Fusion 53(11), 115014–1–115014–16, 2011.

1.1.2 Conference proceedings

- W. Kernbichler, S. V. Kasilov, G. O. Leitold, V. V. Nemov and K. Allmaier, Computation of neoclassical transport in stellarators with finite collisionality, in 15th International Stellarator Workshop, Madrid, 3-7 October 2005, P2-15, 2005.

- W. Kernbichler, S. V. Kasilov, G. O. Leitold, V. V. Nemov and K. Allmaier, Computation of neoclassical transport in stellarators using the full linearized Coulomb collision operator, in 33^{rd} EPS Conference on Plasma Physics, Rome, 19-23 June 2006, ECA 30I, P-2.189, 2006.

- K. Allmaier, S. V. Kasilov, W. Kernbichler, G. O. Leitold and V. V. Nemov, Variance reduction in computations of neoclassical transport in stellarators using a δf method, in 34^{th} EPS Conference on Plasma Physics, Warsaw, Poland, July 2-6 2007, ECA 31F, P-4.041, 2007.

- K. Allmaier, S. V. Kasilov, W. Kernbichler, G. O. Leitold and V. V. Nemov, Computations of neoclassical transport in stellarators using a δf method with reduced variance, in 16^{th} International Stellarator/Heliotron Workshop 2007, Toki, Japan, 15-19 October 2007, P2-021, 2007.

- K. Allmaier, C. D. Beidler, M. Yu. Isaev, S. V. Kasilov, W. Kernbichler, H. Maassberg, S. Murakami, D. A. Spong and V. Tribaldos, ICNTS - Benchmarking of Bootstrap Current Coefficients, in 16^{th} International Stellarator/Heliotron Workshop 2007, Toki, Japan, 15-19 October 2007, P2-029, 2007.

- W. Kernbichler, S. V. Kasilov, G. O. Leitold, V. V. Nemov and K. Allmaier, Recent progress in NEO-2 - A code for neoclassical transport computations based on field line tracing, in 16^{th} International Stellarator/Heliotron Workshop 2007, Toki, Japan, 15-19 October 2007, P2-022, 2007.

- K. Allmaier, S. V. Kasilov, W. Kernbichler, G. O. Leitold and J. L. Velasco, δf Monte Carlo computations of neoclassical transport in stellarators with reduced variance, in 35^{th} EPS Conference on Plasma Physics, Hersonissos, 9-13 June 2008, ECA 32D, P-4.017, 2008.

- J. L. Velasco, K. Allmaier, W. Kernbichler and F. Castejón, Calculation of the bootstrap current profile for the stellarator TJ-II, 37th EPS Conference on Plasma Physics, Dublin, Ireland, 21-25 June 2010, ECA 34A, P1.1099, 2010.

- J. L. Velasco, J .M. García-Regaña, F. Castejón, K. Allmaier, A. Cappa, W. Kernbichler, N. B. Marushchenko and M. Tereshchenko, Electron Bernstein driven and Bootstrap current estimations in the TJ-II stellarator, in 23rd IAEA Fusion Energy Conference, Daejon, Korea Rep. of, 11-16 October 2010, THW/P7-16, 2010.

- V. V. Nemov, S. V. Kasilov, W. Kernbichler, V. N. Kalyuzhnyj and K. Allmaier, Calculations of high energy particle losses for stellarators in real space coordinates, 38th EPS Conference on Plasma Physics, Strasbourg, France, June 27th - July 1st, 2011, ECA 35G, P1.113, 2011.

- K. Allmaier, S. V. Kasilov and W. Kernbichler, Delta f Monte Carlo computations of parallel conductivity in stellarators, 38th EPS Conference on Plasma Physics, Strasbourg, France, June 27th - July 1st, 2011, ECA 35G, P1.112, 2011.

1.2 Preamble

In this thesis parts of the publication [1]

> K. Allmaier, S. V. Kasilov, W. Kernbichler and G. O. Leitold, *Variance reduction in computations of neoclassical transport in stellarators using a δf method*, Phys. Plasmas 15, 072512–1–072512–8 (2008)

have been included in chapter 5, chapter 6 and chapter 7. Contributions of the author and the co-authors to this publication are listed below.

The author K. Allmaier has drafted and written the manuscript, has developed the physical model and the computational method (analytical calculations, development of the numerical scheme, implementation of the code, testing, running of the simulations, analyzing of the computational results and development of visualizations).

Co-author S. V. Kasilov has contributed to analytical calculations, has written a subroutine which computes the movement of particles in the magnetic fields, has revised the manuscript and has contributed expertise and advice in all stages of the development of the method.

Co-author W. Kernbichler has contributed computational results from the NEO-2 code which have been used for benchmarking, has revised the manuscript and has contributed to discussions during the development of the method.

Co-author G. O. Leitold has contributed to discussions in certain phases in the analytical calculations and to the interpretation of the results.

Chapter 2

Confinement in Stellarators

The stellarator is one of the oldest confinement concepts in fusion research and has been invented by Lyman Spitzer in Princeton in 1951 [26, 27]. The word stellarator means ‘star generator’ and is a term for non-axisymmetric toroidal devices. In stellarators fusion plasmas are confined by magnetic fields which are completely generated by external coils (but they can be modified by currents which flow in the plasma itself). Unlike tokamaks stellarators do not need toroidal currents for confinement and the vacuum magnetic field in a stellarator (the magnetic configuration without the plasma) has already confinement properties [28].

As there exist no large plasma currents in stellarators there is the possibility of steady state operation and there are no problems due to current driven instabilities like current disruptions. Stellarators are usually heated by electron cyclotron resonance heating (ECRH), ion cyclotron resonance heating (ICRH) and neutral beam injection (NBI) [29]. The helically wound field lines in a stellarator are created by external coils which are fixed around the plasma torus as shown in figure 2.1. These external currents make the plasma shape non circular. Figures 2.1 and 2.2 show so-called “classical” stellarators (see section 2.1) which combine planar coils and helical coils. An advanced type of stellarator is the “modular” stellarator (see section 2.3) shown in figure 2.3 where complex non-planar coils replace the planar toroidal coils and the helical coils. One advantage of the non-planar coils is that the specific coil geometry can be used to shape the magnetic field geometry which makes an optimization of the magnetic field possible [31].

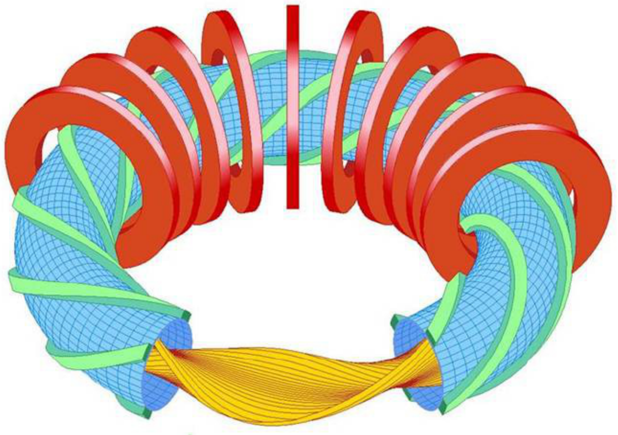

Figure 2.1: Schematic drawing of a classical stellarator with planar coils (red) and four helical coils (green) wound around the vacuum vessel (blue). The plasma is depicted in orange. Figure taken from [30].

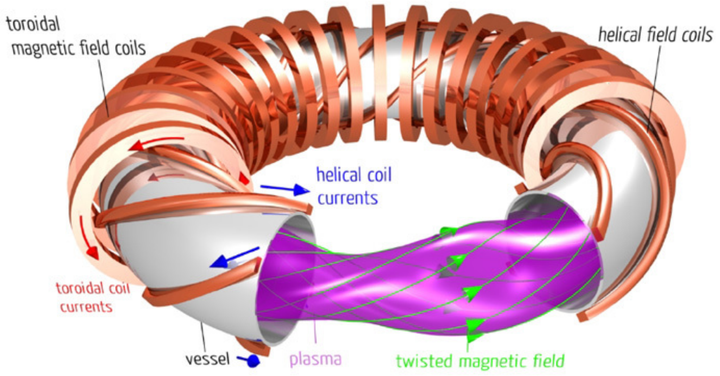

Figure 2.2: Schematic view of a classical stellarator. The magnetic field coils are indicated in brown. The plasma is colored in magenta. The helically twisted magnetic field lines are indicated by green arrows. The red arrows represent the currents in the planar toroidal coils, the blue arrows indicate the currents in the helical coils. Figure taken from [32].

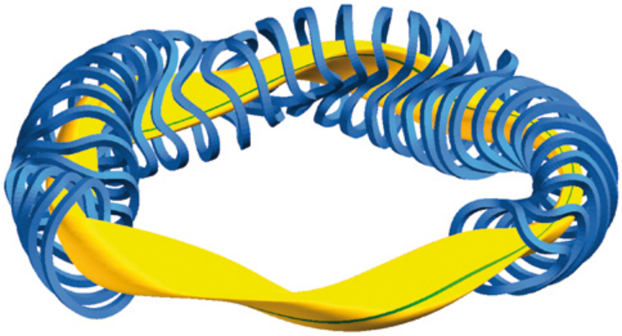

Figure 2.3: Schematic view of the plasma (yellow) and a part of the modular magnetic field coils (blue) of the stellarator Wendelstein 7-X. Figure taken from [33].

Due to the helicity, in helical devices the magnetic field strength depends on both the poloidal and the toroidal angle [34,35]. In helical configurations the magnetic field strength can be approximated by

$$\frac{B}{B_0} = 1 - \varepsilon_t(r)\cos\vartheta - \varepsilon_h(r)\cos\left(l\vartheta - m\varphi\right), \tag{2.1}$$

where r, ϑ and φ are the radius, poloidal and toroidal angle of flux coordinates, respectively, $\varepsilon_t = r/R_0$ is the inverse aspect ratio, R_0 is the major radius of the device, ε_h is the magnitude of the stellarators helical ripple, l is the multipolarity and m denotes the number of field periods. The magnetic field in helical devices can be expressed as the superposition of the helical ripple and the toroidal field component. The equations which are satisfied by the magnetic field $\mathbf{B}$ in equilibrium are given by

$$\begin{aligned} \nabla\cdot\mathbf{B} &= 0\,, && (2.2)\\ \nabla\times\mathbf{B} &= \mu_0\,\mathbf{j}\,, && (2.3)\\ \mathbf{j}\times\mathbf{B} &= \nabla p\,, && (2.4) \end{aligned}$$

where μ_0 is the vacuum permeability, $\mathbf{j}$ is the current density and p is the plasma pressure. Equation (2.4) says that the plasma pressure gradient is balanced by the Lorentz force, it follows that $\mathbf{B}\cdot\nabla p = 0$ and $\mathbf{j}\cdot\nabla p = 0$, which means that the magnetic flux surfaces are surfaces of constant pressure and that currents flow in these flux surfaces. In the case of axisymmetry as in a tokamak a system of cylindrical coordinates (R, φ, z) can be used and all quantities do not depend on φ. This is not true for stellarators where no axisymmetry is present. There, so-called magnetic coordinates may be used, which are defined to conform to the shape of the magnetic flux surfaces. The magnetic field is given by [36–39]

$$\mathbf{B} = \nabla\psi \times \nabla\vartheta + \nabla\varphi \times \nabla\chi \,, \tag{2.5}$$

where φ is a toroidal angle and ϑ is a poloidal angle, respectively. The quantity ψ is called flux surface label and is given by the toroidal magnetic flux $2\pi\psi$ that goes through a poloidal cross-section (φ = constant) between a surface ψ = constant and the magnetic axis. Accordingly, the poloidal magnetic flux $2\pi\chi$ goes through a surface of ϑ = constant between a certain flux surface ψ and the magnetic axis. This magnetic coordinate system has the property that χ is only a function of ψ. The quantity ι measuring the number of poloidal turns of a field line during a toroidal turn is given by [39, 40]

$$\begin{aligned} \iota &= \frac{\mathrm{d}\vartheta}{\mathrm{d}\varphi} = \frac{\mathbf{B}\cdot\nabla\vartheta}{\mathbf{B}\cdot\nabla\varphi} && (2.6)\\ &= \frac{1}{2\pi}\frac{1}{N}\lim_{N\to\infty}\sum_{i=1}^{N}\Delta\vartheta_i \,. && (2.7)\end{aligned}$$

The quantity ι is called rotational transform and is given by the rotational transform angle divided by 2π. Here, i counts the number of toroidal turns and $\Delta\vartheta_i$ is the difference in the poloidal angle after each toroidal turn. Using χ and ψ the rotational transform can be rewritten as [39]

$$\iota(\psi) = \frac{\mathrm{d}\chi}{\mathrm{d}\psi} \,. \tag{2.8}$$

Using ι the relationship between ϑ and φ on a given field line is

$$\vartheta - \iota\varphi = k \,, \tag{2.9}$$

where k is a constant. In the (ϑ, φ) plane the magnetic field lines are straight lines in this coordinate system. The quantity s which is used in

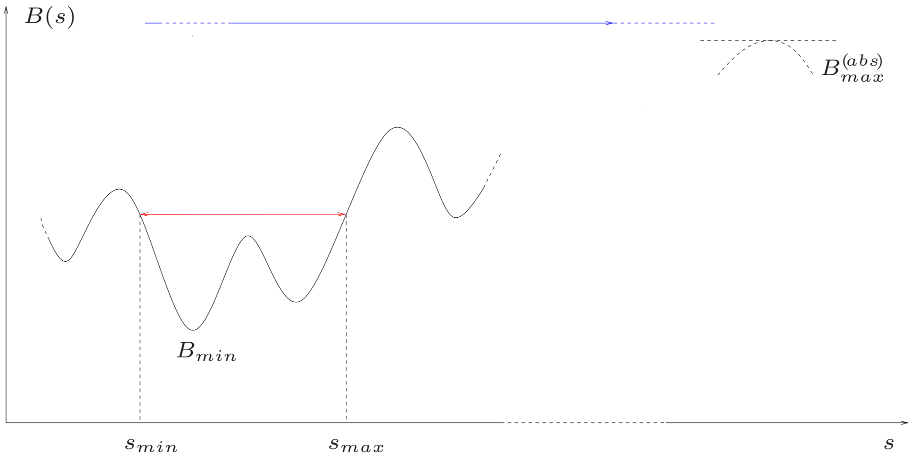

Figure 2.4: Module of the magnetic field B along the path s. There exist different classes of trapped particles. The movement of trapped particles (red) is limited due to reflections caused by the magnetic mirror effect. Locally trapped particles (red) bounce in one (single trapped) or several (multiply trapped) ripples of the magnetic field. Passing particles (blue) are located above the absolute maximum of the magnetic field and travel around the torus.

the following to indicate the flux surfaces is called flux surface label. It is defined by the ratio of the normalized toroidal flux ψ and the normalized toroidal flux ψ_0 at the edge (outermost flux surface)

$$s = \frac{\psi}{\psi_0}\,. \tag{2.10}$$

The quantity s ranges from zero at the magnetic axes to one at the outermost flux surface.

The 3D magnetic field configuration in stellarators has consequences for the particle confinement [28]. Due to the modulation of the magnetic field strength along the magnetic field lines plasma particles can be trapped in local ripples of the magnetic field because of the magnetic mirror effect (see figure 2.4). These trapped particles can drift outwards across the magnetic surfaces which leads to increased particle losses in stellarators due to the so-called neoclassical transport (see chapter 3 and [41–46]).

Some of the advantages of stellarator confinement concepts are summarized below [47, 48]:

- Stellarators have an intrinsically steady-state magnetic field, as there is no need to drive a plasma current.

- Due to the absence of a plasma current there are no current driven instabilities.

- External coils (and not currents in the plasma) are responsible for the position and the rotational transform of the plasma. Also, in stellarators no violent disruptions show up. This makes the design of the plasma facing components (e.g. breeding blankets) more easy.

- "Sawteeth", neoclassical tearing modes or edge-localised modes do not show up in stellarators.

- There are much more possibilities for designs in stellarators than in tokamaks, this gives more chances for optimisations.

- As the plasma density is not limited by a current profile instability (Greenwald density limit) operation at very high densities can take place.

- Due to the 3D shape of the magnetic configuration, there is a greater degree of control over the plasma.

There are not only advantages but also several difficulties with stellarators [47, 48] :

- Stellarators are generally more difficult to build and to understand.

- The coils are very complicated, difficult to design and expensive to build. They must be very precise, withstand huge forces and carry currents in the order of Mega-Amperes.

- Experimentation becomes more difficult because stellarator configurations cannot be varied so much as tokamaks can.

- Due to the lack of symmetry good particle confinement is more difficult to achieve in stellarators than in tokamaks.

- Up to now, stellarators have not reached the same pressures and densities as tokamaks.
- The engineering becomes more difficult because the geometry of the divertor, heat-handling regions and other plasma facing components is more complicated than in tokamaks.
- Especially in classical stellarators there are problems such as bad α-particle confinement, low equilibrium beta limit (large Shafranov-shift) and large neoclassical transport.

In order to improve the stellarator confinement so-called advanced stellarators have been constructed. The first first step was the construction of the stellarator Wendelstein 7-AS. The next experiment will be Wendelstein 7-X which is currently in the start-up phase in Greifswald, Germany, and should give a proof of the reactor potential of advanced stellarators. The design criteria of advanced stellarators are according to H. Wobig [49, p. A160–A161]:

- "A coil system which is technically feasible. The coil system should consist of components which are small enough to be manufactured and tested separately. The concept of modular coils fulfills these conditions.
- Good magnetic surfaces of the vacuum field. This means nested magnetic surfaces without islands and stochastic regions in the interior. Magnetic islands at the edge, which can be used for divertor action, should be somewhat immune against field perturbations.
- Favourable equilibrium properties. With rising plasma pressure modification of the vacuum field should be as small as possible. In particular, the Shafranov shift should be minimized.
- Magnetohydrodynamic stability up to an average beta of 5%. In a fusion reactor the power output grows roughly with the square of beta. This value of 5% is sufficient to achieve a fusion power of 3000 MW in a Helias reactor [50] (Helias = helical advanced stellarator).

- Sufficiently low neoclassical losses of the plasma. Neoclassical losses must be small enough to allow for ignition of the fusion plasma.

- Small or zero bootstrap currents. Bootstrap currents depend on the plasma pressure and change the topology of magnetic surfaces during the start-up phase. Furthermore, they provide a source for tearing mode instabilities as does the induced toroidal current in tokamaks.

- Good confinement of alpha-particles. The loss of highly energetic alpha particles reduces the heating power and provides a risk to the ignition capability. Furthermore, the impact of these α-particles may cause severe damage on the first wall. This issue determines the number of modular coils per period since alpha particles trapped in the modular ripple may rapidly escape from the confinement region."

Here, beta is the plasma pressure $p = nk_BT$ normalized by the magnetic pressure $p_{mag} = B^2/(2\mu_0)$ averaged over the total plasma volume where B is the module of the magnetic field, μ_0 is the vacuum permeability, n is the particle density, k_B is the Boltzmann constant and T is the temperature [31].

Using the above design criteria for advanced stellarators, the magnetic field and plasma geometry of Wendelstein 7-X has been obtained. The modulus of the magnetic field at the last closed flux surface can be seen in figure 2.5 together with the 50 non-planar coils of the magnetic field coil system. There exist five different coil geometries and the coils are mounted in a five- fold symmetry. Each coil type can be controlled separately, which makes it possible to obtain various magnetic field configurations. A set of 20 planar coils create an additional toroidal field, which makes the device even more flexible.

Additional objectives for the stellarator Wendelstein 7-X are according to R. Wolf [52, p. 88]:

- "Steady state operation including particle and energy exhaust with island divertor concept.

- Superconducting coils.

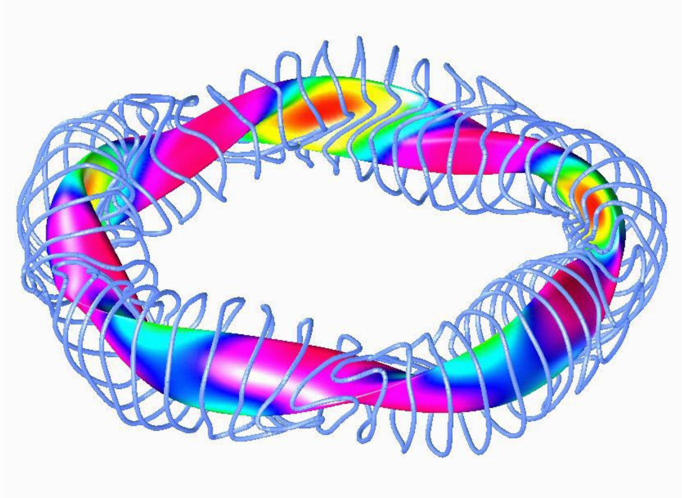

Figure 2.5: Modular stellarator Wendelstein 7-X with non-planar magnetic field coils (light blue). The multicolored area shows the plasma surface. Regions where the module of the magnetic field is high are indicated with red color and regions where the module of the magnetic field is low are indicated with magenta and blue color. Figure taken from [51].

- Actively cooled divertor and first wall components.
- Low magnetic shear with large islands at the plasma boundary.
- ι as much as possible independent of beta.

→ Plasma and magnetic field are as much as possible decoupled.

→ Other optimization criteria are thinkable (e.g. NCSX: tokamak-stellarator hybrid with maximum bootstrap current)."

One of the next steps in the line of stellarator devices would be the construction of a stellarator reactor. The main features of a stellarator reactor according to C. Beidler [53, p. 1] are listed below:

- "Steady-state magnetic fields. No induced eddy currents. No enhanced fatigue of the structure due to pulsed thermal load.
- Steady-state operation at high Q, where Q is the ratio of fusion power to heating power.
- No energy storage and low recirculating power requirements.
- Moderate plasma aspect ratio (8-12) which offers good access to the reactor core.
- Start-up on existing magnetic surfaces with good confinement at all instances.
- No positioning or field shaping coils necessary.
- No major disruptions that could lead to an energy dump on the first wall or on the divertor target plates.
- Several potential methods for impurity control and ash removal exist. Magnetic islands at the plasma edge can be used for divertor action.
- No toroidal current drive is required."

Sections 2.1 – 2.3 give an overview of different types of stellarator concepts following F. Wagner and H. Wobig in reference [34, p. 157–160].

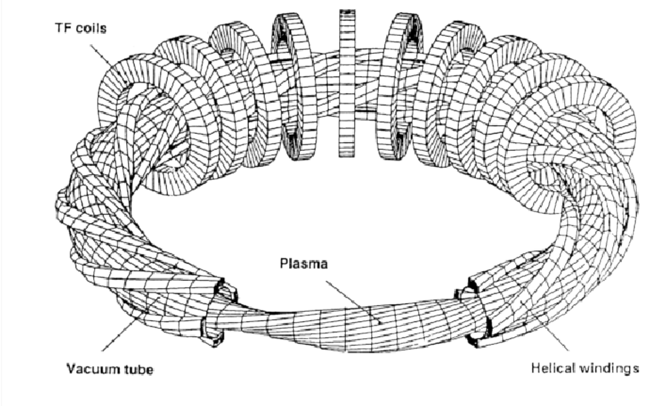

Figure 2.6: The classical stellarator Wendelstein 7-A with helical windings and plain coils. Figure taken from [54].

2.1 The Classical Stellarator

The surfaces of a straight helical system are invariant surfaces ($\mathbf{B} \cdot \nabla\psi = 0$). If the coil system goes away from helical symmetry destruction of the surfaces and stochasticity occur [34]. If a straight helical stellarator is bent into a torus undesired perturbations occur. Magnetic surfaces with stochastic regions and islands appear because the helical symmetry is destroyed by the torus curvature. The axial field $B_0\mathbf{e}_z$ is created by circular coils, in order to be flexible in the experiments these coils are detached from the helical windings. The dominating helical harmonic in the equation for a scalar potential Φ satisfying the Laplace equation $\Delta\Phi = 0$ determines the notation of the helical windings. There are $l = 1$, $l = 2$ and $l = 3$-systems. In a $l = 1$-system the cross sections of the magnetic surfaces roughly are shifted circles, in $l = 2$-systems the shapes are ellipses and in $l = 3$-systems the cross sections of the magnetic surfaces are nearly triangular. The currents in the main field coils and in the helical windings can be varied independently, therefore the cross sections of the magnetic surfaces and the rotational transform can be modified in the experiment. A $l = 2$ stellarator can be seen in figure 2.6. It has plain coils as well as two pairs of helical coils with currents in opposite directions.

2.2 The Torsatron

In the torsatron configuration [55] there are unidirectional currents in the helical windings (see figure 2.7) [34]. In the torsatron some of the problems of the classical stellarator are reduced. l helical windings with currents in the same direction create a field with l-fold poloidal symmetry. Thus both toroidal and poloidal field components are created, in principle further coils are not needed. Problems associated with the two sets of interwoven windings are avoided. Because of the toroidal continuity of the helical coils complications related to maintenance and disassembly still are there but they are less severe. There is a better access in torsatrons because one set of l-windings is used (instead of the $2\,l$ windings of a classical stellarator).

An average vertical field is typically established by the torsatron coils, this field may open the vacuum flux surfaces. Therefore, additional vertical field coils are needed which compensate this effect. As there is used only a single set of windings, the experimental flexibility of the basic torsatron configuration is limited (i.e. well depth, variation of rotational transform, etc.). By using an additional small toroidal field, an additional small vertical field or by variation in the helical harmonic content more flexibility can be obtained.

Achieving a reduction of the forces acting on the helical windings is one advantage of the torsatron configuration. The support structure is no longer a big problem because the forces are directed radially outward. The average outward forces can be directed onto external Helmholtz-type coils far away from the plasma. The radial force averaged over a field period for a torsatron with a particular winding law of the helical coils even may be reduced to zero. Big forces act on the compensation coils in this case, but these forces can be located in regions with enough space for support structure.

2.3 The Modular Stellarator

The helical windings concept provides much flexibility and is therefore useful for experiments, but it presents technical problems because of the interaction between the main field coils and the helical windings in large experiments or in a stellarator reactor [34]. The modular coils concept,

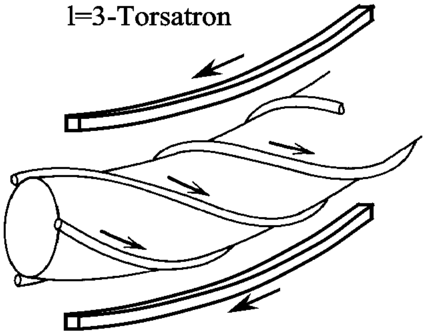

Figure 2.7: Helical windings with parallel currents and plain coils which compensate the vertical field of the helical coils in a torsatron. Figure taken from [56].

which has been realized somehow already in the figure-8 stellarators, overcomes these problems and opens the possibility to build coils with feasible size for larger devices or for a stellarator reactor. Modular coils [57] result from the idea that a current sheath on a surface can produce a toroidal vacuum field in a domain Ω and tangential to the surface $\partial\Omega$. A set of modular and poloidally closed coils which reproduce with high accuracy the magnetic field in the domain Ω can be obtained by discretizing this current sheath to current lines. In order to model these twisted coils and to create the desired magnetic field and the rotational transform by an adequate arrangement of these coils analytic winding laws are used. This concept has been put into reality in the Wendelstein 7-AS stellarator which is shown in figure 2.8. Summarizing this method, on can first optimize the magnetic field configuration according to the requirements of optimum plasma confinement and then, when the result is satisfactory, compute the coil system. In this sense so-called advanced stellarators have been developed [58, 59].

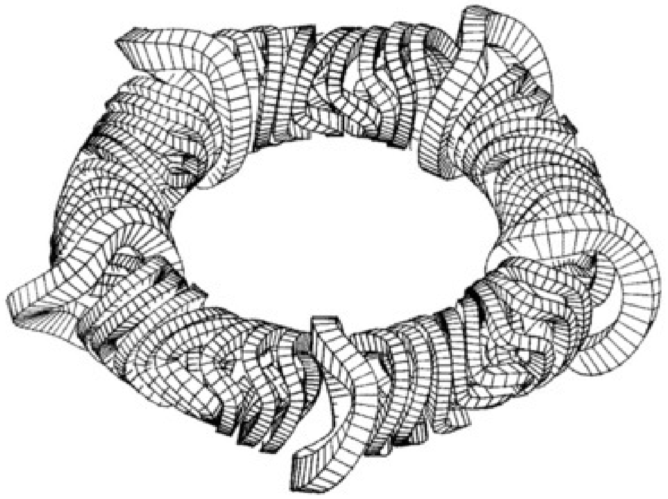

Figure 2.8: Coil system of the first optimized stellarator Wendelstein 7-AS. Figure taken from [60].

Chapter 3

Neoclassical transport coefficients

Transport theory allows to calculate transport coefficients in a collisional plasma which is close to equilibrium by investigating flows corresponding to so-called thermodynamic forces. These forces are generated when the plasma slightly deviates from the equilibrium state. For example, the heating of a plasma which is in thermodynamic equilibrium (same temperature everywhere) in a restricted area causes the plasma to depart from its equilibrium state. In this case, the corresponding thermodynamic force is the temperature gradient. This driving force gives rise to a heat flux which is related to the temperature gradient by the thermal conductivity coefficient. In a general case, a set of driving forces generates a corresponding set of fluxes. These fluxes are linked to the thermodynamic forces by the so-called transport matrix which is composed of the entire set of transport coefficients [41, 42, 61–64].

Neoclassical transport can be described as a diffusive process taking into account a random walk model. In a homogeneous magnetic field the step size of the random walk is determined by the Larmor radius and the whole process is called classical diffusion. If an inhomogeneous toroidal field is present the particles experience drifts which are caused by the magnetic field gradient, by the curvature of the magnetic field and by electric fields. In this case the step size of the random walk is given by the distance that a particle can move away from a magnetic flux surface between collisions. In the low collisionality regime this quantity becomes much larger than the Larmor radius. The associated transport process is called neoclassical diffusion. In tokamaks as well as in stellarators the magnetic field strength B is higher at the inner side (smaller major radius R) than at the outer side (larger major radius R) of the torus. This causes the vertical ($\mathbf{B} \times \nabla B$) drift and a variation of the magnetic field strength along the field lines. Particles following the magnetic field lines therefore may be trapped in magnetic ripples due to the magnetic mirror effect. Particles with large parallel momentum follow the helical trajectories around the torus and are called passing particles. Particles with small parallel momentum may bounce between reflection points and are called trapped particles (see figure 2.4). If no collisions occur trapped particles as well as passing particles are ideally confined in axisymmetric systems because the outward directed drifts are averaged and do not cause net displacements. In collisional regimes trapped particles can move far away from the original flux surfaces (the typical distance is given by the "banana width") and are no longer ideally confined. Due to the 3-dimensional geometry and the complex structure of the magnetic fields in stellarators additional ripples exist (helical ripples) which are responsible for the existence of various classes of trapped particles. If particles are trapped in a single ripple they are called single-trapped particles, if they are trapped in more than one ripple they are called multiply-trapped particles. For particles trapped in the ripples of the magnetic field the vertical drifts do not cancel and these particles may be lost if the collisionality is low. The consequence is a regime in stellarators which does not exist in tokamaks, the so-called $1/\nu$-regime where diffusion coefficients increase as lower the collisionality gets (see figure 3.1). The collisional transport generated by a relatively small number of trapped particles can become much larger than the transport caused by the majority of untrapped particles. The other regimes in figure 3.1 are the Pfirsch-Schlüter-regime where the bounce frequency of trapped particles is much smaller than the collision frequency, therefore the particles can not complete their orbits before they experience collisions. In this regime the diffusion is enhanced with increasing collision frequency depending on a factor related to the geometry of the magnetic configuration. In the so-called plateau-regime the diffusion of particles is almost independent of the collisionality.

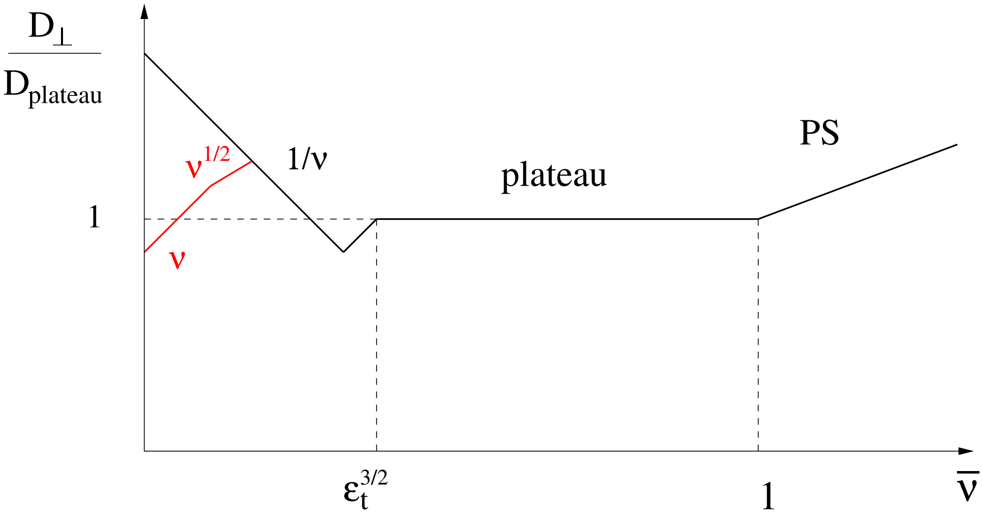

Figure 3.1: Normalized radial transport coefficient $D_\perp/D_{\text{plateau}}$ depicted as a function of the normalized collision frequency $\bar{\nu} = L_c/l_c = 2\pi R\nu/(\iota v_T)$, with the collision frequency ν, the major radius of the torus R, the rotational transform ι and the thermal velocity v_T for tokamaks and stellarators (see e.g. [63]) The radial transport coefficient is independent of the collision frequency in the plateau regime and proportional to the collision frequency in the Pfirsch-Schlüter (PS) regime. At low collisionalities (banana regime) the radial transport coefficient is proportional to ν in tokamaks while in stellarators (red) the $1/\nu$ regime arises. The two axes are depicted in logarithmic scale.

3.1 Drift kinetic equation

The linearized drift kinetic equation (LDKE) determines the evolution of the first-order guiding center (averaged over the gyro motion) distribution function $\tilde{f} = f - f_M$

$$\mathbf{V}_{g0} \cdot \nabla \tilde{f} + \mathbf{v}_d \cdot \nabla f_M - \frac{e v_\parallel E_\parallel}{T} f_M = \mathcal{C} \tilde{f} \,, \tag{3.1}$$

where the total energy and the perpendicular adiabatic invariant are used as velocity space variables and

$$\mathbf{V}_{g0} = v_\parallel \mathbf{n} + \frac{c}{B^2} \mathbf{E} \times \mathbf{B} \,. \tag{3.2}$$

The guiding center drift velocity $\mathbf{V}_g$ is given by

$$\mathbf{V}_g = \mathbf{V}_{g0} + \mathbf{v}_d \,, \tag{3.3}$$

where $\mathbf{v}_d$ is the magnetic drift velocity (see e.g. [65, 66]). Equation (3.1) is linearized with respect to the Larmor radius ρ_L according to

$$\mathbf{v}_d \sim \frac{\rho_L}{L} \ll 1 \,, \tag{3.4}$$

where L is a macroscopic length. In equation (3.1) $\mathcal{C}$ is the linearized Coulomb collision operator, f is the particle distribution function, f_M is a Maxwellian

$$f_M(\psi, v) = n(\psi) \left(\frac{m}{2\pi T(\psi)} \right)^{3/2} \exp \left(- \frac{W - e\Phi(\psi)}{T(\psi)} \right) \,, \tag{3.5}$$

B is the module of the magnetic field $\mathbf{B}$, $\mathbf{n} = \mathbf{B}/B$ is the unit vector along the magnetic field line, $\mathbf{E}$ is the electric field, ψ denotes the flux surface label, e is the particle charge, T is the temperature, n denotes the particle density, W is the energy, Φ is the electrostatic potential, v denotes the module of the test particle velocity and $v_\parallel$ is the parallel velocity. The contra-variant ψ-component of the guiding center drift velocity is given by

$$\dot{\psi} = \mathbf{V}_g \cdot \nabla \psi = \mathbf{v}_d \cdot \nabla \psi = \frac{1}{2\omega_c} (v^2 + v_\parallel^2) k_G |\nabla \psi| \,, \tag{3.6}$$

where $\omega_c = eB/(mc)$ is the cyclotron frequency, m is the particle mass, c is the velocity of light and k_G is the geodesic curvature

$$k_G = \mathbf{n}_\psi \cdot (\mathbf{n} \times (\mathbf{n} \cdot \nabla)\mathbf{n}) \, , \tag{3.7}$$

where $\mathbf{n}_\psi = \nabla\psi/|\nabla\psi|$ (see App. A). Below a simplified version of (3.1) is introduced which is used in the NEO-2 code limited to the case of weak radial electric field (this code is used for benchmarking the results of the NEO-MC code). Neglecting the $\mathbf{E} \times \mathbf{B}$ drift equation (3.1) is reduced to

$$v_\parallel \mathbf{n} \cdot \nabla \tilde{f} + \mathbf{v}_d \cdot \nabla f_M - \frac{e v_\parallel E_\parallel}{T} f_M = \mathcal{C} \tilde{f} \, , \tag{3.8}$$

Note that this simplification effects only the kinetic equation but does not effect the thermodynamic forces, neoclassical fluxes and transport coefficients in the following sections. The second term in equation (3.8) represents a driving term related to the cross-field drift and the third term is associated to the drive by a parallel electric field $E_\parallel$. Introducing a Lorentz collision model

$$\mathcal{L} = \frac{1}{2} \frac{\partial}{\partial \lambda} (1 - \lambda^2) \frac{\partial}{\partial \lambda} \, , \tag{3.9}$$

the drift kinetic equation is given by

$$v_\parallel \frac{\partial \tilde{f}}{\partial s} + \dot{\psi} \frac{\partial f_M}{\partial \psi} - \frac{e v_\parallel E_\parallel}{T} f_M = \nu_d \mathcal{L} \tilde{f} \, , \tag{3.10}$$

where s is the distance along the magnetic field line and ν_d is the deflection collision frequency. If no parallel electric field is taken into account equation (3.10) takes the form

$$v_\parallel \frac{\partial \tilde{f}_G}{\partial s} + \dot{\psi} \frac{\partial f_M}{\partial \psi} = \nu_d \mathcal{L} \tilde{f}_G \, , \tag{3.11}$$

If parallel electric field is present but no radial gradients are taken into account the drift kinetic equation (3.10) becomes

$$v_\parallel \frac{\partial \tilde{f}_E}{\partial s} - \frac{e v_\parallel E_\parallel}{T} f_M = \nu_d \mathcal{L} \tilde{f}_E \, . \tag{3.12}$$

In neoclassical theory the parallel electric field $E_\parallel$ may be replaced in good approximation by the modified parallel electric field $B\langle E_\parallel B\rangle/\langle B^2\rangle$ (see e.g. [67]). The lower indices at the distribution functions in equations (3.11) and (3.12), respectively, indicate the driving forces radial gradient (index G) and parallel electric field (index E). The normalized quantity η is introduced as

$$\eta = \frac{1-\lambda^2}{\hat{B}} \,, \tag{3.13}$$

where $\lambda = v_\parallel/v$ is the pitch angle variable and $\hat{B} = B/B_0$ with B_0 being the reference magnetic field. Using η the Lorentz collision operator (3.9) can be written as

$$\mathcal{L} = 2\lambda \frac{\partial}{\partial \eta}\left(\frac{\lambda\eta}{\hat{B}}\frac{\partial}{\partial \eta}\right) \,, \tag{3.14}$$

and the radial component of the drift velocity (3.6) is given by

$$\dot{\psi} = -\frac{v^2}{\omega_{c0}}\lambda\frac{\partial}{\partial\eta}\left(\frac{\lambda}{\hat{B}}\hat{V}_G\right) \,, \tag{3.15}$$

where

$$\hat{V}_G = \frac{1}{3}\left(\frac{4}{\hat{B}} - \eta\right)|\nabla\psi| k_G \,, \tag{3.16}$$

and

$$\omega_{c0} = \frac{\omega_c}{\hat{B}} = \frac{eB_0}{mc} \,. \tag{3.17}$$

Defining normalized perturbed distribution functions $\hat{f}_G$ and $\hat{f}_E$

$$\hat{f}_G = \frac{\omega_{c0}}{v}\left(\frac{\partial f_M}{\partial \psi}\right)^{-1}\tilde{f}_G \,, \tag{3.18}$$

and

$$\hat{f}_E = \frac{T\hat{B}}{eE_\parallel}(f_M)^{-1}\tilde{f}_E \,, \tag{3.19}$$

equations (3.11) and (3.12) take the form

$$\sigma\frac{\partial \hat{f}_G}{\partial s} - \nu_d \frac{2}{v}\frac{\partial}{\partial \eta}\left(\frac{|\lambda|\eta}{\hat{B}}\frac{\partial \hat{f}_G}{\partial \eta}\right) = -\frac{\omega_{c0}}{v^2|\lambda|}\dot{\psi} \,, \tag{3.20}$$

and

$$\sigma \frac{\partial \hat{f}_E}{\partial s} - \nu_d \frac{2}{v} \frac{\partial}{\partial \eta} \left(\frac{|\lambda| \eta}{\hat{B}} \frac{\partial \hat{f}_E}{\partial \eta} \right) = \sigma \hat{B} \,, \tag{3.21}$$

respectively, where σ denotes the sign of $v_\parallel$. Introducing the sources q_G^σ and q_E^σ according to

$$q_G^\sigma = \frac{\partial}{\partial \eta} \left(\frac{|\lambda|}{\hat{B}} \hat{V}_G \right) = -\frac{\omega_{c0}}{v^2 |\lambda|} \dot{\psi} \,, \tag{3.22}$$

and

$$q_E^\sigma = \sigma \hat{B} \,, \tag{3.23}$$

these equations can be written as

$$\sigma \frac{\partial \hat{f}_G}{\partial s} - \frac{\nu_d}{|v_\parallel|} \mathcal{L} \hat{f}_G = q_G^\sigma \,, \tag{3.24}$$

and

$$\sigma \frac{\partial \hat{f}_E}{\partial s} - \frac{\nu_d}{|v_\parallel|} \mathcal{L} \hat{f}_E = q_E^\sigma \,, \tag{3.25}$$

respectively. Multiplying equations (3.20) and (3.21) with $v_\parallel$ and introducing

$$f_G = -\frac{v}{\omega_{c0}} \hat{f}_G \,, \tag{3.26}$$

and

$$f_E = B_0 \hat{f}_E \,, \tag{3.27}$$

the kinetic equation taking into account the drive by radial gradients can be written as

$$v_\parallel \frac{\partial f_G}{\partial s} - \nu_d \mathcal{L} f_G = \dot{\psi} \,, \tag{3.28}$$

and the kinetic equation taking into account the drive by parallel electric fields is given by

$$v_\parallel \frac{\partial f_E}{\partial s} - \nu_d \mathcal{L} f_E = v_\parallel B \,, \tag{3.29}$$

respectively.

3.2 Flux surface average

Flux surface averages (averages over the volume δV between two neighbouring flux surfaces) can be represented as

$$\begin{aligned}
\langle A(\psi_0)\rangle &\equiv \lim_{\delta V\to 0}\frac{1}{\delta V}\int\limits_{\delta V}\mathrm{d}^3 r A(\mathbf{r}) && (3.30)\\
&= \left(\int \mathrm{d}^3 r\delta\left(\psi(\mathbf{r})-\psi_0\right)\right)^{-1}\int \mathrm{d}^3 r\ \delta\left(\psi(\mathbf{r})-\psi_0\right) A && (3.31)\\
&= \left(\int\limits_{\psi_0-\delta\psi}^{\psi_0+\delta\psi}\mathrm{d}\psi\int\limits_0^{2\pi}\mathrm{d}\vartheta\int\limits_0^{2\pi}\mathrm{d}\varphi\sqrt{g}\delta\left(\psi-\psi_0\right)\right)^{-1}\\
&\times \int\limits_{\psi_0-\delta\psi}^{\psi_0+\delta\psi}\mathrm{d}\psi\int\limits_0^{2\pi}\mathrm{d}\vartheta\int\limits_0^{2\pi}\mathrm{d}\varphi\sqrt{g}\, A\delta\left(\psi-\psi_0\right) && (3.32)\\
&= \left(\int\limits_0^{2\pi}\mathrm{d}\vartheta\int\limits_0^{2\pi}\mathrm{d}\varphi\sqrt{g}\right)^{-1}\int\limits_0^{2\pi}\mathrm{d}\vartheta\int\limits_0^{2\pi}\mathrm{d}\varphi\sqrt{g}\, A && (3.33)\\
&= \frac{1}{4\pi^2\left(\sqrt{g}\right)_{00}}\int\limits_0^{2\pi}\mathrm{d}\vartheta\int\limits_0^{2\pi}\mathrm{d}\varphi\sqrt{g}\, A && (3.34)\\
&= \lim_{L\to\infty}\left(\int\limits_0^{L}\frac{\mathrm{d}s}{B}\right)^{-1}\int\limits_0^{L}\frac{\mathrm{d}s}{B}\, A\,, && (3.35)
\end{aligned}$$

where ϑ and φ are the poloidal and toroidal angles of flux coordinates, respectively, s denotes the distance along the magnetic field line, $\sqrt{g}$ is the metric determinant of flux coordinates (ψ,ϑ,φ)

$$\begin{aligned}
\sqrt{g} &= \frac{1}{\nabla\psi\cdot\nabla\vartheta\times\nabla\varphi} && (3.36)\\
&= \frac{\partial\mathbf{r}}{\partial\psi}\cdot\frac{\partial\mathbf{r}}{\partial\vartheta}\times\frac{\partial\mathbf{r}}{\partial\varphi}\,, && (3.37)
\end{aligned}$$

and

$$(\sqrt{g})_{00} = \frac{1}{4\pi^2}\int_0^{2\pi} \mathrm{d}\vartheta \int_0^{2\pi} \mathrm{d}\varphi \sqrt{g}\,. \tag{3.38}$$

Surface averages can be represented as

$$\frac{1}{S}\int \mathrm{d}\mathbf{S}\cdot\mathbf{A} = \frac{1}{\langle|\nabla\psi|\rangle}\langle\nabla\psi\cdot\mathbf{A}\rangle\,, \tag{3.39}$$

and the flux surface S is given by

$$\begin{aligned}
S &= \langle|\nabla\psi|\rangle \frac{\mathrm{dV}}{\mathrm{d}\psi} && (3.40)\\
&= \int \mathrm{d}^3 r\, \delta(\psi(\mathbf{r})-\psi_0)\,|\nabla\psi| && (3.41)\\
&= \int_0^{2\pi} \mathrm{d}\vartheta' \int_0^{2\pi} \mathrm{d}\varphi' \int \mathrm{d}\psi' \sqrt{g}|\nabla\psi|\delta(\psi'-\psi) && (3.42)\\
&= \int_0^{2\pi} \mathrm{d}\vartheta \int_0^{2\pi} \mathrm{d}\varphi \sqrt{g}|\nabla\psi| && (3.43)\\
&= 4\pi^2\,(\sqrt{g})_{00}\,\langle|\nabla\psi|\rangle\;. && (3.44)
\end{aligned}$$

The surface element d**S** can be represented as

$$\begin{aligned}
\mathrm{d}\mathbf{S} &= \frac{\partial\mathbf{r}}{\partial\vartheta}\times\frac{\partial\mathbf{r}}{\partial\varphi}\mathrm{d}\vartheta\mathrm{d}\varphi && (3.45)\\
&= \frac{\partial\mathbf{r}}{\partial\psi}\cdot\frac{\partial\mathbf{r}}{\partial\vartheta}\times\frac{\partial\mathbf{r}}{\partial\varphi}\,\nabla\psi\,\mathrm{d}\vartheta\,\mathrm{d}\varphi && (3.46)\\
&= \nabla\psi\,\sqrt{g}\,\mathrm{d}\vartheta\,\mathrm{d}\varphi\,. && (3.47)
\end{aligned}$$

3.3 Thermodynamic forces

The radial derivation of the Maxwellian at constant total energy can be represented as

$$\frac{\partial f_M}{\partial\psi} = \frac{\partial r}{\partial\psi}\frac{\partial f_M}{\partial r} = \frac{1}{\langle|\nabla\psi|\rangle}\frac{\partial f_M}{\partial r}\,, \tag{3.48}$$

and equation (3.5) yields

$$\frac{\partial f_M}{\partial r} = f_M \left(\frac{1}{n}\frac{\partial n}{\partial r} - \frac{3}{2T}\frac{\partial T}{\partial r} + \frac{e}{T}\frac{\partial \Phi}{\partial r} + \frac{1}{T}\frac{\partial T}{\partial r} x \right) . \tag{3.49}$$

Introducing the thermodynamic forces A_1, A_2 and A_3

$$\begin{aligned} A_1 &= \frac{1}{n}\frac{\partial n}{\partial r} - \frac{3}{2T}\frac{\partial T}{\partial r} + \frac{e}{T}\frac{\partial \Phi}{\partial r} , & (3.50) \\ A_2 &= \frac{1}{T}\frac{\partial T}{\partial r} , & (3.51) \\ A_3 &= \frac{eE_\parallel}{T\hat{B}} = \frac{e}{T}\frac{\langle E_\parallel \hat{B}\rangle}{\langle \hat{B}^2\rangle} = \frac{eB_0}{T}\frac{\langle \mathbf{E}\cdot\mathbf{B}\rangle}{\langle B^2\rangle} , & (3.52) \end{aligned}$$

equation (3.49) can be represented as

$$\frac{\partial f_M}{\partial r} = f_M (A_1 + A_2\, x) , \tag{3.53}$$

where $x = mv^2/(2T) = v^2/v_T^2$ and $v_T = \sqrt{2T/m}$. The drift kinetic equation (3.10) can be written as

$$v_\parallel \frac{\partial \tilde{f}}{\partial s} - \nu_d \mathcal{L} \tilde{f} = Q^\sigma , \tag{3.54}$$

where the source Q^σ can be represented in terms of the thermodynamic forces (3.50) – (3.52) as

$$\begin{aligned} Q^\sigma &= -\frac{\dot{\psi}}{\langle|\nabla\psi|\rangle}\frac{\partial f_M}{\partial r} + \frac{ev_\parallel E_\parallel}{T} f_M & (3.55) \\ &= -\frac{\dot{\psi}}{\langle|\nabla\psi|\rangle}(A_1 + A_2\, x) f_M + A_3 v_\parallel \hat{B} f_M & (3.56) \\ &= -f_M \sum_{I=1}^{3} Q_I^\sigma A_I . & (3.57) \end{aligned}$$

The sources Q_I in equation (3.57) are given by

$$\begin{aligned} Q_1^\sigma &= \frac{\dot{\psi}}{\langle|\nabla\psi|\rangle} , & (3.58) \\ Q_2^\sigma &= Q_1^\sigma\, x , & (3.59) \\ Q_3^\sigma &= -v_\parallel \hat{B} = -\sigma |v_\parallel| \hat{B} . & (3.60) \end{aligned}$$

Theses sources may be expressed as

$$Q_I^\sigma = \alpha_I q_I^\sigma |v_\parallel| \,, \tag{3.61}$$

where the index $I = 1 \ldots 3$. Normalized sources q_I^σ have been introduced according to

$$\begin{aligned} q_1^\sigma &= \frac{\dot{\psi}}{|v_\parallel| \rho_L} \,, &(3.62)\\ q_2^\sigma &= q_1^\sigma \,, &(3.63)\\ q_3^\sigma &= -\sigma \hat{B} \,, &(3.64) \end{aligned}$$

and the quantities α_I are defined as

$$\begin{aligned} \alpha_1 &= \frac{\rho_L}{\langle |\nabla \psi| \rangle} = \frac{v}{\omega_{c0} \, \langle |\nabla \psi| \rangle} \,, &(3.65)\\ \alpha_2 &= \alpha_1 \, x \,, &(3.66)\\ \alpha_3 &= 1 \,. &(3.67) \end{aligned}$$

Using (3.61) the source (3.57) is given by

$$Q^\sigma = -|v_\parallel| f_M \sum_{I=1}^{3} \alpha_I q_I^\sigma A_I \,, \tag{3.68}$$

and the drift kinetic equation (3.54) can be written as

$$\sigma |v_\parallel| \frac{\partial \tilde{f}}{\partial s} - \nu_d \mathcal{L} \tilde{f} = -|v_\parallel| f_M \sum_{I=1}^{3} \alpha_I q_I^\sigma A_I \,. \tag{3.69}$$

Introducing the normalized perturbed distribution functions $\hat{f}_I^\sigma$ via

$$\tilde{f} = -f_M \sum_{I=1}^{3} \alpha_I A_I \hat{f}_I^\sigma \,, \tag{3.70}$$

single drive problems can be represented as

$$\sigma \frac{\partial \hat{f}_I^\sigma}{\partial s} - \frac{\nu_d}{|v_\parallel|} \mathcal{L} \hat{f}_I^\sigma = q_I^\sigma \,. \tag{3.71}$$

In terms of the sources Q_I^σ (3.61) this equation can be written as

$$\alpha_I v_\parallel \frac{\partial \hat{f}_I^\sigma}{\partial s} - \alpha_I \nu_d \mathcal{L} \hat{f}_I^\sigma = Q_I^\sigma \,. \tag{3.72}$$

3.4 Neoclassical fluxes

Using equations (3.39), (3.58), (3.59) and (3.61) the neoclassical flux densities of particles F_n and energy F_W can be expressed as

$$\begin{aligned}
F_n &= \frac{1}{S}\int \mathrm{d}\mathbf{S}\cdot\int \mathrm{d}^3v\,\mathbf{V}_g\tilde{f} && (3.73)\\
&= \frac{1}{\langle|\nabla\psi|\rangle}\left\langle\int \mathrm{d}^3v\,\dot{\psi}\tilde{f}\right\rangle && (3.74)\\
&= \left\langle\int \mathrm{d}^3v\,Q_1^\sigma\tilde{f}\right\rangle && (3.75)\\
&= \alpha_1\left\langle\int \mathrm{d}^3v\,|v_\parallel|\,q_1^\sigma\tilde{f}\right\rangle && (3.76)\\
&= -\alpha_1\sum_{I'=1}^{3}\alpha_{I'}\left\langle\int \mathrm{d}^3v\,f_M|v_\parallel|\,q_1^\sigma\hat{f}_{I'}^\sigma\right\rangle A_{I'}\,, && (3.77)
\end{aligned}$$

and

$$\begin{aligned}
F_W &= \frac{1}{S}\int \mathrm{d}\mathbf{S}\cdot\int \mathrm{d}^3v\,\frac{mv^2}{2}\mathbf{V}_g\tilde{f} && (3.78)\\
&= \frac{1}{\langle|\nabla\psi|\rangle}\left\langle\int \mathrm{d}^3v\,\frac{mv_T^2}{2}x\,\dot{\psi}\tilde{f}\right\rangle && (3.79)\\
&= T\left\langle\int \mathrm{d}^3v\,Q_2^\sigma\tilde{f}\right\rangle && (3.80)\\
&= T\,\alpha_2\left\langle\int \mathrm{d}^3v\,|v_\parallel|q_2^\sigma\tilde{f}\right\rangle && (3.81)\\
&= -T\,\alpha_2\sum_{I'=1}^{3}\alpha_{I'}\left\langle\int \mathrm{d}^3v\,f_M|v_\parallel|\,q_2^\sigma\hat{f}_{I'}^\sigma\right\rangle A_{I'}\,, && (3.82)
\end{aligned}$$

respectively, where equation (3.70) has been substituted in the last equalities. Using equations (3.60) and (3.61) the flux surface average of the parallel current density $j_\parallel$ multiplied by the module of the magnetic field

B can be represented as

$$\langle j_\parallel B \rangle = e \left\langle B \int \mathrm{d}^3 v \, v_\parallel \tilde{f} \right\rangle \tag{3.83}$$

$$= e B_0 \left\langle \int \mathrm{d}^3 v \, Q_3^{-\sigma} \tilde{f} \right\rangle \tag{3.84}$$

$$= e B_0 \alpha_3 \left\langle \int \mathrm{d}^3 v \, |v_\parallel| q_3^{-\sigma} \tilde{f} \right\rangle \tag{3.85}$$

$$= -e B_0 \, \alpha_3 \sum_{I'=1}^{3} \alpha_{I'} \left\langle \int \mathrm{d}^3 v \, f_M |v_\parallel| \, q_3^{-\sigma} \hat{f}_{I'}^{\sigma} \right\rangle A_{I'} \, , \tag{3.86}$$

where equation (3.70) has been substituted in the last step. Note, that the sources Q_1^σ, Q_2^σ, q_1^σ and q_2^σ, respectively, do not depend on σ and the index σ is only formal here. The flux densities (3.75), (3.80) and (3.84) can be written in a general form as

$$I_I = \left\langle \int \mathrm{d}^3 v \, Q_I^{-\sigma} \tilde{f} \right\rangle \, , \tag{3.87}$$

where the fluxes I_I have been defined as

$$I_1 = F_n \tag{3.88}$$

$$I_2 = \frac{F_W}{T} \tag{3.89}$$

$$I_3 = \frac{\langle j_\parallel B \rangle}{e B_0} \, . \tag{3.90}$$

3.5 Transport Coefficients

From equations (3.77), (3.82) and (3.86) it follows that the fluxes I_I can be expressed as

$$I_I = -\alpha_I \sum_{I'=1}^{3} \alpha_{I'} \left\langle \int \mathrm{d}^3 v \, f_M |v_\parallel| \, q_I^{-\sigma} \hat{f}_{I'}^{\sigma} \right\rangle A_{I'} \tag{3.91}$$

$$= -n \sum_{I'=1}^{3} L_{II'} \, A_{I'} \, , \tag{3.92}$$

where the transport coefficients $L_{II'}$ are given by

$$\begin{aligned} L_{II'} &= \alpha_I \alpha_{I'} \left\langle \int \mathrm{d}^3 v \, \frac{f_M}{n} |v_\parallel| \, q_I^{-\sigma} \hat{f}_{I'}^{\sigma} \right\rangle \qquad (3.93) \\ &= \alpha_{I'} \left\langle \int \mathrm{d}^3 v \, \frac{f_M}{n} \, Q_I^{-\sigma} \hat{f}_{I'}^{\sigma} \right\rangle , \qquad (3.94) \end{aligned}$$

and the sources Q_I^σ are defined by (3.58) – (3.60). Equation (3.92) summarizes the relations between fluxes, transport coefficients and thermodynamic forces and can be written with the transport matrix as

$$\left(\begin{array}{c} \langle F_n \rangle \\ \langle F_W \rangle / T \\ -\langle j_\parallel \hat{B} \rangle / e \end{array} \right) = -n \left(\begin{array}{ccc} L_{11} & L_{12} & L_{13} \\ L_{21} & L_{22} & L_{23} \\ L_{31} & L_{32} & L_{33} \end{array} \right) \left(\begin{array}{c} A_1 \\ A_2 \\ A_3 \end{array} \right) . \qquad (3.95)$$

Taking into account that the velocity space integration can be expressed as

$$\begin{aligned} \int \mathrm{d}^3 v &= 2\pi \int_0^\infty \mathrm{d}v \, v^2 \int_0^\pi \mathrm{d}\chi \sin\chi \qquad (3.96) \\ &= 2\pi \int_0^\infty \mathrm{d}v \, v^2 \int_{-1}^{1} \mathrm{d}\lambda \, , \qquad (3.97) \end{aligned}$$

where χ is the pitch angle, the transport coefficients $L_{II'}$ can be represented as

$$\begin{aligned} L_{II'} &= \frac{1}{\sqrt{2\pi}} \left(\frac{m}{T} \right)^{3/2} \alpha_I \alpha_{I'} \\ &\times \left\langle \int_0^\infty \mathrm{d}v \, v^2 \, \exp\left(-\frac{m v^2}{2T} \right) \int_{-1}^{1} \mathrm{d}\lambda \, |v_\parallel| q_I^{-\sigma} \hat{f}_{I'}^{\sigma} \right\rangle \qquad (3.98) \\ &= \frac{1}{\sqrt{\pi}} \int_0^\infty \mathrm{d}x \, \sqrt{x} \, \exp\left(-x\right) \alpha_I \alpha_{I'} \left\langle \int_{-1}^{1} \mathrm{d}\lambda \, |v_\parallel| q_I^{-\sigma} \hat{f}_{I'}^{\sigma} \right\rangle \qquad (3.99) \\ &= \frac{2}{\sqrt{\pi}} \int_0^\infty \mathrm{d}x \, \sqrt{x} \, \exp\left(-x\right) \; D_{II'} \, , \qquad (3.100) \end{aligned}$$

where $x = mv^2/(2T)$. Mono-energetic transport coefficients $D_{II'}$ can be obtained by replacing f_M in (3.93) by the mono-energetic distribution function f_{mono}

$$f_{\mathrm{mono}} = \frac{1}{4\pi v_0^2} \, n \, \delta(v - v_0) \, , \tag{3.101}$$

and integrating over velocity yields

$$D_{II'} \quad = \quad v\alpha_I \alpha_{I'} \left\langle \frac{1}{2} \int\limits_{-1}^{1} \mathrm{d}\lambda \, |\lambda| \, q_I^{-\sigma} \hat{f}_{I'}^{\sigma} \right\rangle . \tag{3.102}$$

Substituting the sources Q_I (3.61) this quantity can be represented as

$$D_{II'} \quad = \quad \alpha_{I'} \left\langle \frac{1}{2} \int\limits_{-1}^{1} \mathrm{d}\lambda \, Q_I^{-\sigma} \hat{f}_{I'}^{\sigma} \right\rangle . \tag{3.103}$$

In terms of η which has been introduced in equation (3.13) the mono-energetic transport coefficients can be expressed as

$$D_{II'} = v\alpha_I \alpha_{I'} \sum_{\sigma=\pm 1} \left\langle \frac{\hat{B}}{4} \int\limits_{0}^{1/\hat{B}} \mathrm{d}\eta \, q_I^{-\sigma} \hat{f}_{I'}^{\sigma} \right\rangle . \tag{3.104}$$

Using (3.35) the mono-energetic transport coefficients may be also presented as field line averages according to

$$D_{II'} \quad = \quad \frac{1}{4} v\alpha_I \alpha_{I'} \lim_{L \to \infty} \left(\int\limits_0^L \frac{\mathrm{d}s}{\hat{B}} \right)^{-1} \int\limits_0^L \mathrm{d}s \sum_{\sigma=\pm 1} \int\limits_0^{1/\hat{B}} \mathrm{d}\eta \, q_I^{-\sigma} \hat{f}_{I'}^{\sigma} \, . \tag{3.105}$$

In order to define the mono-energetic diffusion coefficient D_{mono} and the normalized bootstrap current coefficient λ_{bb} the drift kinetic equation is rewritten as follows

$$V^i \frac{\partial \tilde{f}}{\partial Z^i} - \nu_d \mathcal{L} \tilde{f} = -V^i \frac{\partial f_M}{\partial Z^i} \, , \tag{3.106}$$

where $f = f_M + \tilde{f}$ and Z^i is a set of phase space variables and V^i is a drift motion velocity. Introducing the sources Q and $\hat{Q}$ according to

$$\begin{aligned} Q &= -V^i \frac{\partial f_M}{\partial Z^i} = -\dot{\psi}\frac{\partial f_M}{\partial \psi} &\quad (3.107)\\ &= -\hat{Q}\frac{v^2}{v_0^2}\frac{1}{\langle|\nabla\psi|\rangle}\frac{\partial f_M}{\partial r} &\quad (3.108)\\ \hat{Q} &= \frac{v_0^2}{v^2}\dot{\psi}\,, &\quad (3.109)\end{aligned}$$

equation (3.106) can be written as

$$v_0\lambda\frac{\partial \hat{f}}{\partial s} - \frac{v_0}{v}\nu_d\mathcal{L}\hat{f} = \hat{Q}\,, \tag{3.110}$$

where $\hat{f}$ is given by

$$\hat{f} = -\tilde{f}\frac{v_0}{v}\langle|\nabla\psi|\rangle\left(\frac{\partial f_M}{\partial r}\right)^{-1}. \tag{3.111}$$

3.5.1 Diffusion coefficient

The radial diffusion coefficient D relates the gradient of the density n to the particle flux density F_n according to

$$F_n = -D\frac{\partial n}{\partial r}\,. \tag{3.112}$$

Using equation (3.74) the radial diffusion coefficient can be written as

$$\begin{aligned} D &= -\frac{1}{\langle|\nabla\psi|\rangle}\left\langle\int \mathrm{d}^3v\,\dot{\psi}\tilde{f}\right\rangle\left(\frac{\partial n}{\partial r}\right)^{-1} &\quad (3.113)\\ &= -\frac{2\pi}{\langle|\nabla\psi|\rangle^2}\left\langle\int_0^\infty \mathrm{d}v\frac{v^3}{v_0}\int_{-1}^{1}\mathrm{d}\lambda\,\dot{\psi}\hat{f}\frac{f_M}{n}\right\rangle\,, &\quad (3.114)\\ & &\quad (3.115)\end{aligned}$$

where $\tilde{f}$ has been substituted from (3.111)

$$\tilde{f} = \hat{f}\frac{v}{v_0}\frac{1}{\langle|\nabla\psi|\rangle}\frac{\partial n}{\partial r}\frac{f_M}{n}\,. \tag{3.116}$$

Replacing the Maxwellian by a mono-energetic distribution function (3.101) yields for the mono-energetic radial diffusion coefficient D_{mono}

$$\begin{aligned} D_{\text{mono}} &= -\frac{1}{2\left\langle|\nabla\psi|\right\rangle^2}\left\langle\int\limits_{-1}^{1}\mathrm{d}\lambda\int\limits_{0}^{\infty}\mathrm{d}v\,\frac{v^3}{v_0^3}\delta(v-v_0)\dot{\psi}\hat{f}\right\rangle & (3.117)\\ &= -\frac{1}{\left\langle|\nabla\psi|\right\rangle^2}\left\langle\frac{1}{2}\int\limits_{-1}^{1}\mathrm{d}\lambda\,\dot{\psi}\,\hat{f}\right\rangle . & (3.118)\end{aligned}$$

In chapter 7.4.1 mono-energetic radial diffusion coefficients D_{mono} normalized to the plateau diffusion coefficient

$$D_{\text{plateau}} = \frac{\pi v \rho_L^2}{8\sqrt{2}\,\iota R}\,, \tag{3.119}$$

are plotted for a variety of magnetic configurations and confinement regimes versus the collisionality parameter L_c/l_c where $L_c = 2\pi R/\iota$ is the connection length, R is the major radius of the configuration, ι is the rotational transform and l_c is the mean free path.

3.5.2 Bootstrap coefficient

The existence of the bootstrap current in Tokamaks has been first predicted by Bickerton, Connor and Taylor [68] and Galeev [69] in 1971. In experiments the bootstrap current has been first detected by Zarnstorff and Prager in 1984 [70]. In helical geometry neoclassical theory predicts the bootstrap current particularly in collisionless plasmas, first calculations were done by Shaing and Callen [46] applying the Hirshman-Sigmar moment method [41]. Further calculations of the bootstrap current in non-symmetric toroidal devices can be found in e.g. references [44,71–77]. The bootstrap current can affect the transport, the equilibrium and the stability characteristics of toroidal plasmas [78]. In tokamaks it can become a significant part of the total plasma current and is therefore aimed to be maximized in order to reduce the effort for external current drive. In stellarators the confining magnetic fields are generated by external helical coils. There, currents in the plasma may be a disadvantage because they can modify the desired topology. Therefore in stellarators one tries to minimize the bootstrap current because it is responsible for a shift in the rotational transform ι (it can either increase or reduce ι) which might be unfavorable for the confinement properties of the device. It is possible to decrease the bootstrap current in stellarators to zero (it is even possible to reverse its direction [79]). It has been shown by Boozer and Gardner [80] that the bootstrap current in stellarators depends on the magnetic configuration only through the magnetic field strength on each flux surface $B(\psi, \vartheta, \varphi)$ and through the rotational transform $\iota(\psi)$. In case of a small fraction of trapped particles the dependence of the bootstrap current on the device geometry is defined by a constant which can be computed by integration along the field line [81, 82]. The bootstrap current causes a net toroidal current in contrast to the Pfirsch Schlüter current. The Pfirsch Schlüter current j_{PS} evolves in response to a pressure gradient and the flux surface average of the Pfirsch Schlüter current multiplied with the magnetic field is zero $\langle j_{PS} B \rangle = 0$, whereas the flux surface average of the Pfirsch Schlüter current itself $\langle j_{PS} \rangle$ does not vanish.

The physical mechanism driving the bootstrap current can be described in a simplified picture as follows. On the high field side of the torus particles with higher values of the pitch parameter can be reflected and the poloidal orbits of these particles are not closed. The poloidal projections of the trajectories of such particles are shaped like bananas and therefore called banana orbits (see figure 3.2). Regarding two adjacent banana orbits in the poloidal projection co-moving (moving in the direction of the toroidal current) and counter-moving (moving against the direction of the toroidal current) particles are passing by at a flux surface intersecting this orbits. There may be more co-moving than counter-moving particles on this flux surface due to the existence of a density gradient. The particles are charged and therefore a current is generated at this intersection. Due to collisions particles from the more populated inner orbits are transferred to the outer orbits and give rise to a net outward diffusion of particles and finally the current is transferred from the trapped to the passing particles by collisions. The current which is now carried by the passing particles is called bootstrap current. However, no net current is produced by the trapped particles themselves because their only net toroidal movement is the toroidal drift which is usually small compared to the bootstrap current. In summary,

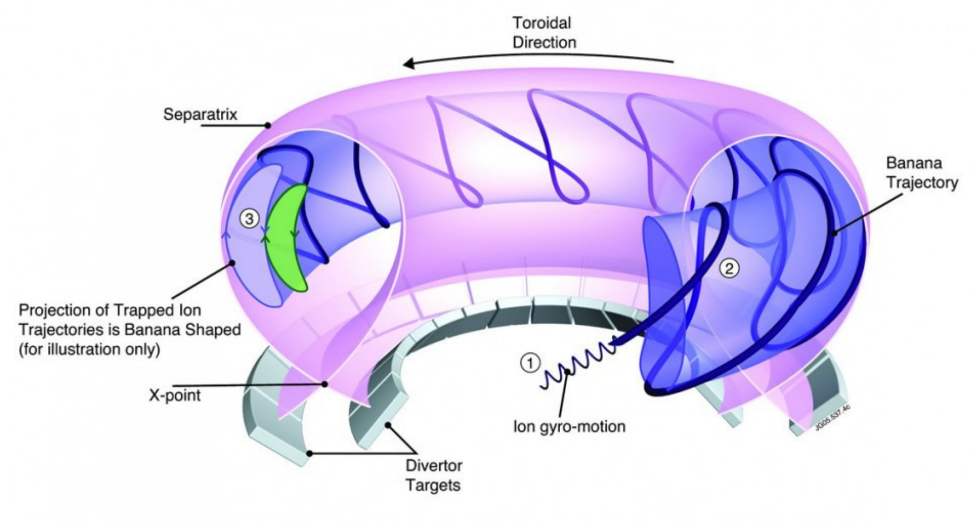

Figure 3.2: Adjacent trapped particle orbits giving rise to the bootstrap current in a tokamak. The plasma boundary is shown as a pink surface and the trajectory of a trapped particle is indicated as a dark blue line. The projection of this orbit on the poloidal plane is banana shaped and called banana orbit. Another banana orbit is depicted in green to show that the particles move in opposite directions (indicated by arrows) where the bananas touch. Due to a density gradient and momentum exchange between trapped and passing particles the bootstrap current is produced. Figure taken from [83].

the bootstrap current arises due to the curvature of the magnetic field, particles moving along banana orbits, the presence of a density gradient and momentum transfer between trapped and untrapped particles [84].

Estimation of the parallel current density

The width δ_b of a banana shaped particle orbit is given by (see e.g. [85])

$$\delta_b \approx \frac{q\rho_L}{\sqrt{\varepsilon_t}}\,, \tag{3.120}$$

where $q = 1/\iota$ is the safety factor, ι is the rotational transform, ρ_L is the Larmor radius and $\varepsilon_t = a/R$ is the inverse aspect ratio where a and R are minor and major radius of the torus, respectively. The parallel current density $j_\parallel$ is given by

$$j_\parallel = e\,\vartriangle\! n\, v_\parallel\,, \tag{3.121}$$

where n is the particle density and $\vartriangle\! n$ can be approximated by

$$\vartriangle\! n = \delta_b \frac{\mathrm{d}n}{\mathrm{d}r}\,. \tag{3.122}$$

Substituting (3.122) and (3.120) into (3.121) one gets

$$j_\parallel = e v_T \frac{q\rho_L}{\sqrt{\varepsilon_t}} \frac{\mathrm{d}n}{\mathrm{d}r}\,, \tag{3.123}$$

where $v_\parallel \approx v_T = \sqrt{2T/m}$ is the thermal velocity, T is the temperature and m is the particle mass. Substituting $\omega_c = v_T/\rho_L = eB/(mc)$, the equation for the parallel current density $j_\parallel$ is given by

$$j_\parallel = 2\frac{q}{\sqrt{\varepsilon_t}} \frac{cT}{B} \frac{\mathrm{d}n}{\mathrm{d}r}\,, \tag{3.124}$$

and contains a factor $q/\sqrt{\varepsilon_t}$ which depends on the geometry of the configuration.

Bootstrap current coefficient

According to (3.83) the flux surface average of the parallel current density $j_\parallel$ multiplied by the absolute value of the magnetic field B can be represented as

$$\langle j_\parallel B\rangle = e\left\langle B\int \mathrm{d}^3v\, v_\parallel \tilde{f}\right\rangle . \tag{3.125}$$

Substituting (3.116) leads to

$$\langle j_\parallel B\rangle = \frac{2\pi e}{\langle|\nabla\psi|\rangle}\left\langle B\int\limits_{-1}^{1}\mathrm{d}\lambda\,\lambda\frac{1}{v_0}\hat{f}\frac{\partial}{\partial r}\int\limits_{0}^{\infty}\mathrm{d}v\,v^4 f_M\right\rangle . \tag{3.126}$$

The integral over the Maxwellian is given by

$$\begin{aligned}\int\limits_0^\infty \mathrm{d}v\,v^4\,f_M &= \int\limits_0^\infty \mathrm{d}v\,v^4\,\frac{n}{\pi^{\frac{3}{2}}}\frac{1}{v_0^3}\,\exp\left\{-\frac{v^2}{v_0^2}\right\} && (3.127)\\ &= \frac{n}{\pi^{\frac{3}{2}}}v_0^2\underbrace{\int\limits_0^\infty \mathrm{d}u\,u^4\,\exp\left\{-u^2\right\}}_{3\sqrt{\pi}/8} && (3.128)\\ &= \frac{3}{4\pi}\frac{nT}{m}\,, && (3.129)\end{aligned}$$

where $v_0=\sqrt{2T/m}$ and equation (3.126) can be written as

$$\langle j_\parallel B\rangle = \frac{3e}{2mv_0}\frac{1}{\langle|\nabla\psi|\rangle}\frac{\partial p}{\partial r}\left\langle\int\limits_{-1}^{1}\mathrm{d}\lambda\,\lambda B\hat{f}\right\rangle . \tag{3.130}$$

If no temperature gradient and no radial electric field is present the gradient of the pressure p is linked to the parallel current density $j_\parallel$ according to (see e.g. [86], where $\lambda_{bb}=\lambda_\parallel\,\langle B^2\rangle\,/\,\langle B^2_{max}\rangle$)

$$\langle j_\parallel B\rangle = -\lambda_{bb}\,c\,\langle|\nabla\psi|\rangle\,\frac{\partial p}{\partial\psi}\,, \tag{3.131}$$

where c is the speed of light. Using equations (3.130) and (3.131) the normalized mono-energetic bootstrap coefficient λ_{bb} can be expressed as

$$\lambda_{bb} = -\frac{3}{\rho_L B_0 \langle|\nabla\psi|\rangle} \left\langle \frac{1}{2}\int\limits_{-1}^{1} \mathrm{d}\lambda\, \lambda B \hat{f} \right\rangle , \tag{3.132}$$

where the Larmor radius $\rho_L = v_0 mc/(eB_0)$ in the reference magnetic field B_0 has been substituted in the last step.

In chapter 7.4.2 normalized mono-energetic bootstrap current coefficients λ_{bb} are plotted for a variety of magnetic configurations and confinement regimes versus the collisionality parameter L_c/l_c where $L_c = 2\pi R/\iota$ is the connection length, R is the major radius of the configuration, ι is the rotational transform and l_c is the mean free path.

3.5.3 Conductivity coefficient

For computations of mono-energetic transport coefficients with methods based on [3] in many cases pitch-angle scattering collision models are used. For the calculation of a variety of plasma quantities therefore it might be necessary to use momentum correction techniques (see e.g. [87–89]). In order to apply these methods the evaluation of the mono-energetic parallel conductivity coefficient is essential.

This coefficient is related to the response of particles to a parallel electric field. The drift kinetic equation (3.72) for the distribution function $\hat{f}_3^\sigma$ is given by

$$v_\parallel \frac{\partial \hat{f}_3^\sigma}{\partial s} - \nu_d \mathcal{L} \hat{f}_3^\sigma = Q_3^\sigma , \tag{3.133}$$

where

$$Q_3^\sigma = -v_\parallel \hat{B} . \tag{3.134}$$

Substituting equations (3.64) and (3.67) into equation (3.102) the mono-energetic parallel conductivity coefficient D_{33} can be written as

$$D_{33} = -v \left\langle \frac{1}{2}\int\limits_{-1}^{1} \mathrm{d}\lambda\, \lambda \hat{B} \hat{f}_3^\sigma \right\rangle . \tag{3.135}$$

In chapter 7.4.3 normalized mono-energetic parallel conductivity coefficients $D_{co} = -D_{33}\, L_c/l_c$ are plotted for a variety of magnetic configurations and confinement regimes versus the collisionality parameter L_c/l_c where $L_c = 2\pi R/\iota$ is the connection length, R is the major radius of the configuration, ι is the rotational transform and l_c is the mean free path.

Chapter 4

Full *f* method

In this chapter a so-called box counting scheme for the computation of transport coefficients related to the bootstrap current is presented. The parallel current density $j_\parallel$ normalized by the module of the magnetic field B is represented as

$$\left\langle \frac{j_\parallel}{B} \right\rangle = \frac{e}{\Delta V} \int\limits_{\Delta V} \mathrm{d}^3 r \int\limits_{\mathbb{R}} \mathrm{d}^3 v \;\; \frac{1}{B(\mathbf{r})} v_\parallel(\mathbf{r},\mathbf{v}) f(\mathbf{r},\mathbf{v}) \; . \tag{4.1}$$

where e is the elementary charge and the distribution function f is approximated by

$$f(\mathbf{r},\mathbf{v}) = \frac{1}{N_s} \sum_{i=1}^{N_s} \delta(\mathbf{r}-\mathbf{r}_i)\delta(\mathbf{v}-\mathbf{v}_i) \; , \tag{4.2}$$

where $\mathbf{r}_i$ and $\mathbf{v}_i$ are particle positions and velocities after the i^{th} numerical step and N_s denotes the total number of numerical steps. In flux surface coordinates $(\psi, \vartheta, \varphi)$ and velocity space variables (λ, v) the normalized parallel current density $j_\parallel$ can be written as

$$\begin{aligned} \left\langle \frac{j_\parallel}{B} \right\rangle &= \frac{e}{\Delta V} \int\limits_{\psi}^{\psi+\delta\psi} \mathrm{d}\psi \int\limits_{\vartheta}^{\vartheta+\delta\vartheta} \mathrm{d}\vartheta \int\limits_{\varphi}^{\varphi+\delta\varphi} \mathrm{d}\varphi \; \sqrt{g} \int\limits_{0}^{\infty} \mathrm{d}v \int\limits_{-1}^{1} \mathrm{d}\lambda \; 2\pi v^2 \\ &\times \frac{1}{B(\psi,\vartheta,\varphi)} \; v_\parallel(\psi,\vartheta,\varphi,v,\lambda) \; f(\psi,\vartheta,\varphi,v,\lambda) \; , \end{aligned} \tag{4.3}$$

and the distribution function can be represented as

$$\begin{aligned} f(\psi,\vartheta,\varphi,v,\lambda) &= \frac{1}{N_s}\sum_{i=1}^{N_s}\frac{1}{\sqrt{g}}\frac{1}{2\pi v^2} \\ &\times\ \delta(\psi-\psi_i)\delta(\vartheta-\vartheta_i)\delta(\varphi-\varphi_i)\delta(v-v_i)\delta(\lambda-\lambda_i), \quad (4.4) \end{aligned}$$

where ψ denotes the flux surface label, ϑ and φ are the poloidal and toroidal angles of flux coordinates, respectively, $\lambda = v_\parallel/v$ is the pitch angle variable and v is the particle velocity. The Jacobian $\sqrt{g}$ and the volume element ΔV are defined as

$$\sqrt{g} = \frac{\partial(x,y,z)}{\partial(\psi,\vartheta,\varphi)}\ , \quad (4.5)$$

$$\Delta V = \int\limits_{\psi}^{\psi+\delta\psi} \mathrm{d}\psi \int\limits_{\vartheta}^{\vartheta+\delta\vartheta} \mathrm{d}\vartheta \int\limits_{\varphi}^{\varphi+\delta\varphi} \mathrm{d}\varphi\ \sqrt{g}\ . \quad (4.6)$$

In order to develop a numerical scheme the particle step density $\langle n\rangle^k$ and the normalized current density $\langle j_\parallel/B\rangle^k$ associated to a subannulus in ψ are introduced as

$$\begin{aligned} \langle n\rangle^k &= \frac{1}{\Delta V}\int\limits_0^{\psi_{max}}\mathrm{d}\psi\int\limits_0^{2\pi}\mathrm{d}\vartheta\int\limits_0^{2\pi}\mathrm{d}\varphi\ \sqrt{g}\ \int\limits_0^{\infty}\mathrm{d}v\int\limits_{-1}^{1}\mathrm{d}\lambda\ 2\pi v^2 \\ &\times\ f(\psi,\vartheta,\varphi,v,\lambda)\ \Theta^k(\psi_i) \quad (4.7) \\ &= \frac{1}{\Delta V}\frac{1}{N_s}\sum_{i=1}^{N_s}\Theta^k(\psi_i)\ , \quad (4.8) \\ \left\langle\frac{j_\parallel}{B}\right\rangle^k &= \frac{e}{\Delta V}\int\limits_0^{\psi_{max}}\mathrm{d}\psi\int\limits_0^{2\pi}\mathrm{d}\vartheta\int\limits_0^{2\pi}\mathrm{d}\varphi\ \sqrt{g}\int\limits_0^{\infty}\mathrm{d}v\int\limits_{-1}^{1}\mathrm{d}\lambda\ 2\pi v^2 \\ &\times\ \frac{1}{B(\psi,\vartheta,\varphi)}v_\parallel(\psi,\vartheta,\varphi,v,\lambda)f(\psi,\vartheta,\varphi,v,\lambda)\ \Theta^k(\psi_i) \quad (4.9) \\ &= \frac{e}{\Delta V}\frac{1}{N_s}\sum_{i=1}^{N_s}\frac{1}{B(\psi_i,\vartheta_i,\varphi_i)}\ v_\parallel(\psi_i,\vartheta_i,\varphi_i,v_i,\lambda_i)\ \Theta^k(\psi_i), \quad (4.10) \end{aligned}$$

where k is the index of a subannulus limited by the flux surfaces ψ_a^k and ψ_b^k and the step function Θ^k is defined as

$$\Theta^k(\psi_i)\begin{cases} = 0 & \psi_i < \psi_a^k \; ; \quad \psi_b^k < \psi_i \\ = 1 & \psi_a^k < \psi_i < \psi_b^k \quad . \end{cases} \tag{4.11}$$

The density gradient $(\partial n/\partial\psi)^k$ in the k^{th} subannulus can be approximated by

$$\left(\frac{\partial n}{\partial \psi}\right)^k = \frac{\langle n\rangle^{k+1} - \langle n\rangle^{k-1}}{2\Delta\psi} \;, \tag{4.12}$$

where $\Delta\psi$ denotes the width of the equidistant subannuli. The bootstrap current coefficient $\hat{\lambda}_b^k$ in the k^{th} subannulus can be calculated from

$$\hat{\lambda}_b^k = \left\langle \frac{j_\parallel}{B} \right\rangle^k \Bigg/ \left(\frac{\partial n}{\partial \psi}\right)^k \;. \tag{4.13}$$

For a total number of particles N_p the particle step density $\langle n\rangle^{k,N_p}$, the current density $\langle j_\parallel/B\rangle^{k,N_p}$, the gradient $(\partial n/\partial\psi)^{k,N_p}$ and the bootstrap current coefficient $\hat{\lambda}_b^{k,N_p}$ in the k^{th} subannulus are given by

$$\langle n\rangle^{k,N_p} = \frac{1}{\Delta V}\frac{1}{N_T}\sum_{j=1}^{N_p}\sum_{i=1}^{N_s^j}\Theta^k(\psi_i^j) \;, \tag{4.14}$$

$$\left\langle \frac{j_\parallel}{B} \right\rangle^{k,N_p} = \frac{e}{\Delta V}\frac{1}{N_T} \times \sum_{j=1}^{N_p}\sum_{i=1}^{N_s^j}\frac{1}{B(\psi_i^j,\vartheta_i^j,\varphi_i^j)} v_\parallel(\psi_i^j,\vartheta_i^j,\varphi_i^j,v_i^j,\lambda_i^j)\Theta^k(\psi_i^j) \tag{4.15}$$

$$\left(\frac{\partial n}{\partial \psi}\right)^{k,N_p} = \frac{1}{2\Delta\psi}\left(\langle n\rangle^{k+1,N_p} - \langle n\rangle^{k-1,N_p}\right) \;, \tag{4.16}$$

$$\hat{\lambda}_b^{k,N_p} = \left\langle \frac{j_\parallel}{B} \right\rangle^{k,N_p} \Bigg/ \left(\frac{\partial n}{\partial \psi}\right)^{k,N_p} \;, \tag{4.17}$$

where j is the particle index and the total number of steps N_T is given by

$$N_T = \sum_{j=1}^{N_p} N_s^j \;. \tag{4.18}$$

$$\Theta^k(\psi_i^j) \begin{cases} = 0 & \psi_i^j < \psi_a^k \; ; \quad \psi_b^k < \psi_i^j \\ = 1 & \psi_a^k < \psi_i^j < \psi_b^k \quad . \end{cases} \tag{4.19}$$

The number of steps N_s^j of an individual particle j depends on when the particle leaves the annulus. N_T is the total number of steps of all particles. It can be seen from (4.14) and (4.15) that the quantities $\langle n\rangle^{k,N_p}$ and $\langle j_\parallel/B\rangle^{k,N_p}$ are obtained by summing up contributions from all steps of all particles in the respective subannulus and then by dividing these quantities by the total number of steps N_T of all particles.

Chapter 5

δf method

The efficiency of standard Monte Carlo (MC) techniques is rather low when calculating plasma currents. In these methods not only the part of the distribution function which determines the plasma currents is involved, instead the total distribution function is computed. Numerical calculations of neoclassical transport coefficients in fusion plasmas can be made much more efficient by using so-called δf methods (see e.g. [90–98]). There the equilibrium part of the distribution function f_0 (which may be mono-energetic or Maxwellian) is expressed analytically, and particle simulations are used to model only the deviation from the equilibrium δf. The principle of these methods is that the particle distribution function is represented as $f = f_0 + \delta f$ and weights are associated to so-called marker particles which evolve in time in such a way that the modification of the equilibrium distribution is correctly reproduced [84]. In the simulations the evolution of the particles is computed in a series of subsequent time steps by changing the pitch parameters in accordance with a Monte Carlo model of the Lorentz collision operator and by integrating the particle drift equations over time in order to update the positions and momenta of the particles [3].

5.1 Basic equations

Mono-energetic transport coefficients are determined by the steady state solution of the linearized drift kinetic equation for the normalized perturbation of the distribution function $\hat{f}$ (which is also named “marker”).

If the total energy and the perpendicular adiabatic invariant are used as velocity space variables this equation takes the following form

$$\mathcal{L}_D \hat{f} \equiv \left(\frac{\partial}{\partial t} + \mathbf{V}_g \cdot \nabla - \mathcal{L}_C \right) \hat{f} = \dot{\psi} \equiv \mathbf{V}_g \cdot \nabla \psi, \tag{5.1}$$

where $\mathbf{V}_g$, and $\dot{\psi}$ are guiding center drift velocity and its contra-variant ψ-component, respectively, ψ is a flux surface label, $\mathcal{L}_C$ is the Lorentz collision operator, and the marker $\hat{f}$ is defined through the local Maxwellian distribution function f_M and the total distribution function f via

$$f = f_M - \hat{f} \, \frac{\partial f_M}{\partial \psi} \, . \tag{5.2}$$

Eq. (5.1) is solved using the orbits in the limit $B \to \infty$ with $E/B = const$ so that $\mathbf{V}_g \to \mathbf{V}_{g0}$ which means that magnetic drifts disappear on the l.h.s. but stay finite on the r.h.s when solving the equations of motion. In the following it is convenient to use instead of the total energy and the perpendicular invariant the velocity module v and the pitch parameter $\lambda = v_\parallel / v$ as velocity space variables. In these variables the collision operator is given as

$$\mathcal{L}_C = \frac{v}{l_c} \frac{\partial}{\partial \lambda} \left(1 - \lambda^2 \right) \frac{\partial}{\partial \lambda}, \tag{5.3}$$

where l_c is the mean free path, and the mono-energetic radial diffusion coefficient and the normalized bootstrap coefficient, respectively, are given by (see equations (3.118) and (3.132))

$$\begin{aligned} D_{\text{mono}} &= -\frac{1}{\langle |\nabla \psi| \rangle^2} \left\langle \frac{1}{2} \int_{-1}^{1} \mathrm{d}\lambda \hat{f} \dot{\psi} \right\rangle, && (5.4) \\ \lambda_{bb} &= -\frac{3}{\rho_L B_0 \langle |\nabla \psi| \rangle} \left\langle \frac{1}{2} \int_{-1}^{1} \mathrm{d}\lambda \hat{f} \lambda B \right\rangle. && (5.5) \end{aligned}$$

Here, ρ_L is the Larmor radius in the reference magnetic field B_0, B is the magnetic field module and

$$\langle A \rangle = \frac{\int \mathrm{d}\vartheta \int \mathrm{d}\varphi \sqrt{g} A}{\int \mathrm{d}\vartheta \int \mathrm{d}\varphi \sqrt{g}} \tag{5.6}$$

denotes the average over the volume between neighboring flux surfaces with ϑ and φ being the poloidal and the toroidal angles of flux coordinates and g is the metric determinant of flux coordinates $(\psi, \vartheta, \varphi)$. In absence of a temperature gradient and a radial electric field the quantity λ_{bb} is linked to the equilibrium (bootstrap) current density $j_{\|}$ and the gradient of the pressure p by

$$\lambda_{bb} = -\left\langle j_{\|} B \right\rangle \left(c \left\langle |\nabla \psi| \right\rangle \frac{\mathrm{d}p}{\mathrm{d}\psi} \right)^{-1} \tag{5.7}$$

if l_c is put to a constant during the energy convolution. In the following D_{mono} is normalized by the plateau diffusion coefficient

$$D_{\mathrm{plateau}} = \frac{\pi v \rho_L^2}{8\sqrt{2}\, \iota R}, \tag{5.8}$$

where ι is the rotational transform and R is the major radius.
It should be noted that the drift motion of test particles is described exactly by the operator $\mathcal{L}_D$ (which includes also the radial motion) in Eq. (5.1). As a result, $\mathcal{L}_D$ conserves the total energy but not the kinetic energy alone. Therefore, strictly speaking, $\hat{f}$ is not mono-energetic if a radial electric field is present. However, the typical change of the kinetic energy of the test particle during a couple of collision times needed to model $\hat{f}$ is small compared to the original test particle energy if the amplitude of the magnetic field modulation on the magnetic surface is small (a usual argument justifying the mono-energetic approach). Therefore this change of the kinetic energy of test particles is ignored in the following and v is treated there as a parameter but not as an independent phase space coordinate. Also, the local approach of neoclassical theory assumes that change of the radial variable ψ during test particle motion is negligible small and, therefore, ψ plays the role of a parameter. This limit can be realized with any accuracy by scaling both, the magnetic field and radial electric field with the same sufficiently large factor. Thus, despite the fact that test particle trajectories are integrated in the full $(\psi, \theta, \varphi, v, \lambda)$ phase space, the dependence of the perturbed distribution function $\hat{f}$ on ψ and v is treated as parametric and the set of independent variables $\mathbf{z}$ is reduced to $(\vartheta, \varphi, \lambda)$ for the solutions of kinetic equation (5.1) in the following.

5.2 Integral formulation of the Monte Carlo procedure

Traditionally [99], the Monte Carlo procedure for the solution of the drift kinetic equation is introduced directly for equation (5.1) by defining a random step over test particle phase space coordinates for a small time interval Δt and by verifying that the Fokker-Planck equation describing test particle orbits advanced by such steps coincides with the original drift kinetic equation. At the same time, a variety of variance reduction methods developed mainly for Monte Carlo solutions of integral equations need some re-formulation in order to develop an algorithm. In order to enable a direct use of these methods, it is convenient to re-write (5.1) in the integral form using a Green's function G defined by

$$\begin{aligned} \mathcal{L}_D\, G(t,\mathbf{z},\mathbf{z}_0) &= 0, && (5.9)\\ G(0,\mathbf{z},\mathbf{z}_0) &= (g(\mathbf{z}_0))^{-1/2}\,\delta(\mathbf{z}-\mathbf{z}_0), && (5.10) \end{aligned}$$

where $\mathbf{z}=(\vartheta,\varphi,\lambda)$. This Green's function is normalized to 1,

$$\int \mathrm{d}^3 z\,(g(\mathbf{z}))^{1/2}\,G(t,\mathbf{z},\mathbf{z}_0)=1. \tag{5.11}$$

Thus, a formal solution to Eq. (5.1) is

$$\begin{aligned} \hat{f}(t,\mathbf{z}) = \int \mathrm{d}^3 z_0\,(g(\mathbf{z}_0))^{1/2}\Bigg(& G(t-t_0,\mathbf{z},\mathbf{z}_0)\hat{f}(t_0,\mathbf{z_0}) + \\ & + \int\limits_{t_0}^{t} \mathrm{d}t' G(t-t',\mathbf{z},\mathbf{z}_0)\dot{\psi}(\mathbf{z_0})\Bigg). \end{aligned} \tag{5.12}$$

If a steady state solution is looked for,

$$\hat{f}(t,\mathbf{z})=\hat{f}(\mathbf{z})\,, \tag{5.13}$$

Eq. (5.12) becomes an integral equation for

$$F(\mathbf{z})=(g(\mathbf{z}))^{1/2}\,\hat{f}(\mathbf{z})\,, \tag{5.14}$$

which is given below also in operator form,

$$F(\mathbf{z}) = \int \mathrm{d}^3 z_0 K(\mathbf{z}, \mathbf{z}_0) F(\mathbf{z_0}) + Q(\mathbf{z}) \equiv \mathcal{K} F + Q, \tag{5.15}$$

where

$$K(\mathbf{z}, \mathbf{z}_0) = (g(\mathbf{z}))^{1/2} \, G(\Delta t, \mathbf{z}, \mathbf{z}_0) \,, \tag{5.16}$$

Δt is the integration time step and

$$\begin{aligned} Q(\mathbf{z}) &= \int \mathrm{d}^3 z_0 \, (g(\mathbf{z}) g(\mathbf{z}_0))^{1/2} \int\limits_0^{\Delta t} \mathrm{d}t' G(t', \mathbf{z}, \mathbf{z}_0) \dot{\psi}(\mathbf{z_0}) \\ &\equiv (g(\mathbf{z}))^{1/2} \, \Delta\psi(\mathbf{z}) \approx (g(\mathbf{z}))^{1/2} \, \dot{\psi}(\mathbf{z}) \Delta t. \end{aligned} \tag{5.17}$$

The Monte Carlo operator, $\mathbf{Z}(\Delta t, \mathbf{z}_0)$, is introduced as a random position of a test particle starting at $\mathbf{z}_0$ after a single time step modeled in a standard way [99]. First, the particle pitch is changed randomly in accordance with $\mathcal{L}_C$,

$$\lambda' = \lambda_0 \left(1 - \Delta_C\right) + \left(\Delta_C \left(1 - \lambda_0^2\right)\right)^{1/2} \xi \,, \tag{5.18}$$

where

$$\Delta_C = \frac{v \Delta t}{l_c} \,, \tag{5.19}$$

and ξ is a random number which takes the values ±1 with equal probabilities. Then an integration step of particle drift equations over the time interval Δt is performed. Thus, the kernel of the integral equation is given by an expectation value

$$K(\mathbf{z}, \mathbf{z}_0) = \overline{\delta \left(\mathbf{z} - \mathbf{Z}(\Delta t, \mathbf{z}_0)\right)} \,. \tag{5.20}$$

More precisely, Eq. (5.20) can be viewed as a definition of the random process $\mathbf{Z}(\Delta t, \mathbf{z}_0)$ via the transition probability density $K(\mathbf{z}, \mathbf{z}_0)$ while the algorithm described in (5.18) defines a linear approximation in Δt of this random process. At this point, in addition to $\mathbf{Z}(\Delta t, \mathbf{z}_0)$, random numbers $\mathbf{z}_{(k)} \equiv (\vartheta_{(k)}, \varphi_{(k)}, \lambda_{(k)})$ where $k = 0, 1, 2, \ldots$ are introduced via the recurrence relation (5.22) and the probability density (5.25). Various overlined quantities below are the expectation values with respect to these random numbers.

The solution of (5.15) by direct iterations is given by an expectation value of an integral along the stochastic orbit,

$$
\begin{aligned}
F &= \sum_{k=0}^{\infty} \mathcal{K}^k Q = C_0 \sum_{k=0}^{\infty} \overline{w_{(0)}\, \delta\left(\mathbf{z} - \mathbf{z}_{(k)}\right)}, && (5.21)\\
\mathbf{z}_{(k)} &= \mathbf{Z}(\Delta t, \mathbf{z}_{(k-1)}), && (5.22)\\
w_{(0)} &= \Delta\psi(\mathbf{z}_{(0)}), && (5.23)
\end{aligned}
$$

where

$$C_0 = \int \mathrm{d}^3 z \, (g(\mathbf{z}))^{1/2} \ , \tag{5.24}$$

and the random starting point $\mathbf{z}_{(0)}$ is chosen with the probability density

$$\overline{\delta\left(\mathbf{z} - \mathbf{z}_{(0)}\right)} = C_0^{-1} \, (g(\mathbf{z}))^{1/2} \ . \tag{5.25}$$

The averages (5.4) and (5.5) are given by expectation values as

$$
\begin{aligned}
D_{\text{mono}} &= -\frac{1}{\langle |\nabla\psi| \rangle^2} \sum_{k=0}^{\infty} \overline{w_{(0)} \dot{\psi}(\mathbf{z}_{(k)})}, && (5.26)\\
\lambda_{bb} &= -\frac{3}{\rho_L B_0 \langle |\nabla\psi| \rangle} \sum_{k=0}^{\infty} \overline{w_{(0)} \lambda_{(k)} B(\mathbf{z}_{(k)})}. && (5.27)
\end{aligned}
$$

When $k\Delta t$ exceeds a few collision times, the correlation between $\mathbf{z}_{(k)}$ and $w_{(0)}$ is lost and, therefore, such terms in (5.26) and (5.27) tend to zero, e.g.,

$$\overline{w_{(0)} \dot{\psi}(\mathbf{z}_{(k)})} \rightarrow \overline{w_{(0)}} \ \overline{\dot{\psi}(\mathbf{z}_{(k)})} = 0 \, , \tag{5.28}$$

because

$$
\begin{aligned}
\overline{\lambda_{(k)} B(\mathbf{z}_{(k)})} &= \frac{1}{C_0} \int \mathrm{d}^3 z \, (g(\mathbf{z}))^{1/2} \, \lambda B(\mathbf{z}) = 0, && (5.29)\\
\overline{\dot{\psi}(\mathbf{z}_{(k)})} &= \frac{1}{C_0} \int \mathrm{d}^3 z \, (g(\mathbf{z}))^{1/2} \, \dot{\psi}(\mathbf{z}) = 0 \, , && (5.30)
\end{aligned}
$$

due to Liouville's theorem. The same is true also for $\overline{w_{(0)}}$. Thus, a finite sum over k in (5.26) and (5.27) is sufficient.

The method of constant test particle weights described by (5.26) and (5.27) has rather low variance for computations of D_{mono}, however, variance of λ_{bb} has a very unfavorable scaling with collisionality. Indeed, only the orbits originating in the boundary layer located in the velocity space around the trapped-passing boundary λ_{t-p} which is determined by the absolute maximum of the magnetic field on the flux surface contribute to λ_{bb}. The boundary layer has the width

$$\Delta\lambda \sim (L_c/l_c)^{1/2} \;, \tag{5.31}$$

where $L_c = 2\pi R/\iota$ is the connection length. The test particle weight $w_{(0)}$ depends on the coordinates of the starting point of the orbit but is independent of the sign of the starting pitch parameter $\lambda_{(0)}$. Noticeable contributions to λ_{bb} are produced by test particles only when they are traveling in the passing phase space region because in the trapped region rapid oscillations of the pitch parameter λ are compensated in the time integral (5.27). Test particles starting deeply in the trapped particle region produce almost no contribution to λ_{bb} because when they reach the passing region after many oscillations in the magnetic well, probabilities to be detrapped to the co-passing region with $\lambda > 0$ and to the counter-passing region with $\lambda < 0$ become weakly dependent on the starting point (and, therefore, on $w_{(0)}$) and are almost the same. Thus, contributions from such particles compensate each other statistically. Similar compensation takes place also for particles starting deeply in the passing region because correlation between the sign of the pitch parameter and the starting position (and, therefore, the weight $w_{(0)}$) is quickly lost for them after passing the distance

$$l \sim l_c^{1/3} L_c^{2/3} \ll l_c \,, \tag{5.32}$$

while the amounts of particles starting from the same spatial point with $\pm\lambda_{(0)}$ are the same in average. Therefore, in the long mean free path regime only trapped particles starting from the boundary layer whose detrapping probabilities essentially depend on the starting position and passing particles from this layer whose trapping probabilities also depend on the starting position can produce in average essential contribution to λ_{bb} (see Fig. 5.1). Actually, this manifests the fact that asymmetry in the passing particle distribution function is driven by the asymmetry of the boundary condition for this function at the trapped-passing boundary. Note that the contribution of a particle from the boundary layer is $\Delta\lambda$ times smaller than of a normal passing particle because of a higher trapping probability. Therefore, the variance of λ_{bb} scales for this method as $(l_c/L_c)^2$ in the long mean free path regime.

For the computation of the mono-energetic parallel conductivity coefficient a formal solution to (3.133) is given by

$$\begin{aligned} \hat{f}_3^\sigma(t,\mathbf{z}) &= \int \mathrm{d}^3 z_0 \, [g(\mathbf{z}_0)]^{1/2} \Bigg(G(t-t_0,\mathbf{z},\mathbf{z}_0)\hat{f}_3^\sigma(t_0,\mathbf{z}_0) + \\ &\quad + \int\limits_{t_0}^{t} \mathrm{d}t' G(t-t',\mathbf{z},\mathbf{z}_0) Q_3^\sigma(\mathbf{z}_0) \Bigg) , \end{aligned} \tag{5.33}$$

where $\mathbf{z} = (\vartheta, \varphi, \lambda)$. If a steady state solution is looked for,

$$\hat{f}_3^\sigma(t,\mathbf{z}) = \hat{f}_3^\sigma(\mathbf{z}) , \tag{5.34}$$

equation (5.33) becomes an integral equation for

$$F_3^\sigma(\mathbf{z}) = [g(\mathbf{z})]^{1/2} \; \hat{f}_3^\sigma(\mathbf{z}) , \tag{5.35}$$

which can be written in operator form as

$$F_3^\sigma(\mathbf{z}) = \int \mathrm{d}^3 z_0 K(\mathbf{z},\mathbf{z}_0) F_3^\sigma(\mathbf{z}_0) + \hat{Q}_3^\sigma(\mathbf{z}) \equiv \mathcal{K} F_3^\sigma + \hat{Q}_3^\sigma , \tag{5.36}$$

where

$$K(\mathbf{z},\mathbf{z}_0) = [g(\mathbf{z})]^{1/2} \, G(\Delta t,\mathbf{z},\mathbf{z}_0) , \tag{5.37}$$

Δt is the integration time step and

$$\hat{Q}_3^\sigma(\mathbf{z}) = \int \mathrm{d}^3 z_0 [g(\mathbf{z})]^{1/2} [g(\mathbf{z}_0)]^{1/2} \int\limits_0^{\Delta t} \mathrm{d}t' G(t',\mathbf{z},\mathbf{z}_0) Q_3^\sigma(\mathbf{z}_0) \tag{5.38}$$

$$\approx [g(\mathbf{z})]^{1/2} \, \Delta t \, Q_3^\sigma(\mathbf{z}) . \tag{5.39}$$

The Monte Carlo procedure is the same as described after equation (5.17). The solution of (5.36) by direct iterations is given by an expectation value

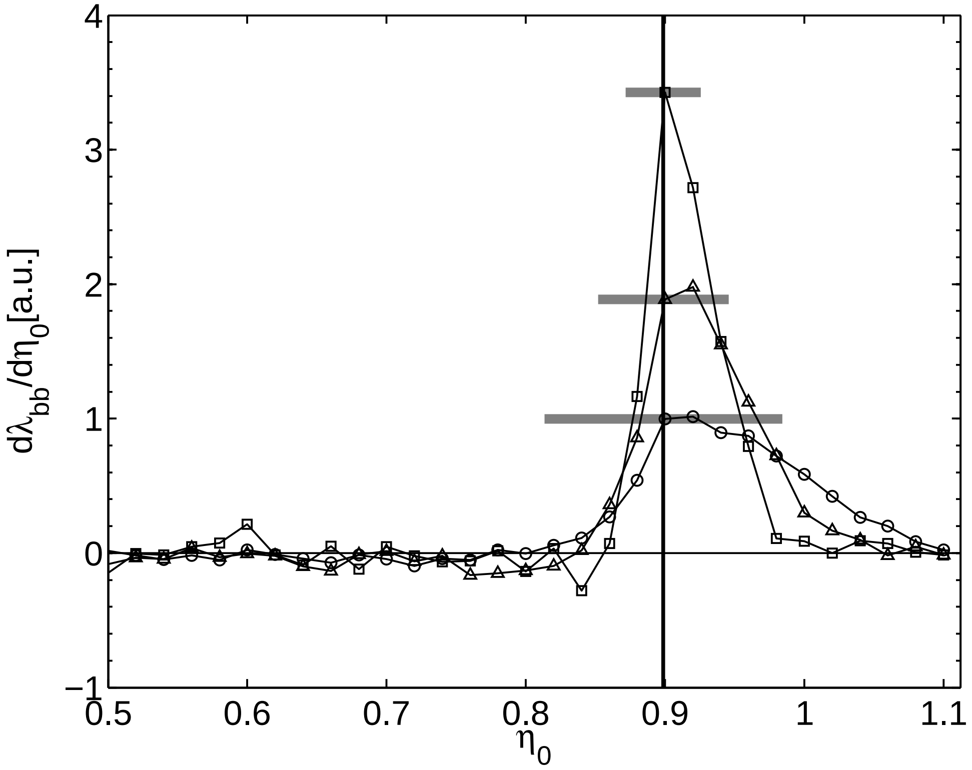

Figure 5.1: Distribution $\mathrm{d}\lambda_{bb}/\mathrm{d}\eta_0$ of test particle contributions to λ_{bb} (Eq. (5.27)) over the starting values of the normalized perpendicular invariant $\eta_0 = (1 - \lambda_0^2)B_0/B(\mathbf{z}_0)$ for a tokamak with aspect ratio $R/r = 10$, where B_0 is a reference magnetic field. Collisionality parameters L_c/l_c are $1 \cdot 10^{-2}$ (circles), $3 \cdot 10^{-3}$ (triangles) and $1 \cdot 10^{-3}$ (squares). The width of the boundary layer for each curve is indicated by a horizontal bar. The position of the trapped-passing boundary is shown by the solid vertical line.

of an integral along the stochastic orbit,

$$\begin{aligned} F_3^\sigma &= \sum_{k=0}^{\infty} \mathcal{K}^k \hat{Q}_3^\sigma & (5.40) \\ &= C_0 \sum_{k=0}^{\infty} \overline{w_{(0)}^\sigma \, \delta\left(\mathbf{z} - \mathbf{z}_{(k)}\right)} \,, & (5.41) \\ \mathbf{z}_{(k)} &= \mathbf{Z}(\Delta t, \mathbf{z}_{(k-1)}) \,, & (5.42) \\ w_{(0)}^\sigma &= \Delta t \, Q_3^\sigma(\mathbf{z}_{(0)}) & (5.43) \\ &= -\Delta t \, v_\parallel(\mathbf{z}_{(0)}) \, \hat{B}(\mathbf{z}_{(0)}) \,, & (5.44) \end{aligned}$$

where

$$C_0 = \int \mathrm{d}^3 z [g(\mathbf{z})]^{1/2} \,, \tag{5.45}$$

and the random starting point $\mathbf{z}_{(0)}$ is chosen with the probability density

$$\overline{\delta\left(\mathbf{z} - \mathbf{z}_{(0)}\right)} = C_0^{-1} [g(\mathbf{z})]^{1/2} \,. \tag{5.46}$$

Substituting the definition of the flux surface average (3.33) into equation (3.135) the mono-energetic parallel conductivity coefficient can be written as

$$\begin{aligned} D_{33} &= -\frac{1}{C_0} \int \mathrm{d}^3 z \, F_3^\sigma \, v_\parallel \hat{B} & (5.47) \\ &= -\frac{1}{B_0} \sum_{k=0}^{\infty} \overline{w_{(0)}^\sigma \, v_\parallel(\mathbf{z}_{(k)}) \, B(\mathbf{z}_{(k)})} \,, & (5.48) \end{aligned}$$

where F_3^σ has been substituted from (5.41) and integration over $\mathbf{z}$ has been performed in the second equality.

5.3 Standard δf method

The distribution of the test particles at each step remains to be the equilibrium distribution,

$$\overline{\delta\left(\mathbf{z} - \mathbf{z}_{(k)}\right)} = C_0^{-1} \left(g(\mathbf{z})\right)^{1/2} \,, \tag{5.49}$$

which is independent of the pitch parameter λ (dependence of the metric determinant g on the full set of phase space variables $\mathbf{z}$ is only formal here). Therefore, the correlation between any function of $\mathbf{z}_{(k)}$ and any other function of $\mathbf{z}_{(j)}$ depends only on the time interval needed for test particle to travel from the point $\mathbf{z}_{(k)}$ to $\mathbf{z}_{(j)}$, i.e. on the difference $k-j$,

$$\overline{w_{(0)}\lambda_{(k-j)}B(\mathbf{z}_{(k-j)})} = \overline{w_{(j)}\lambda_{(k)}B(\mathbf{z}_{(k)})}\,, \tag{5.50}$$

where

$$w_{(j)} = \Delta\psi(\mathbf{z}_{(j)}) \approx \dot{\psi}(\mathbf{z}_{(j)})\Delta t\,. \tag{5.51}$$

Thus the averages (5.26) and (5.27) can be presented as

$$\begin{aligned}
D_{\mathrm{mono}} &= -\frac{1}{\langle|\nabla\psi|\rangle^2}\lim_{k\to\infty}\overline{W_{(k)}\dot{\psi}(\mathbf{z}_{(k)})} && (5.52)\\
&= -\frac{1}{\langle|\nabla\psi|\rangle^2}\lim_{K\to\infty}\frac{1}{K}\sum_{k=0}^{K}\overline{W_{(k)}\dot{\psi}(\mathbf{z}_{(k)})}, && (5.53)\\
\lambda_{bb} &= -\frac{3}{\rho_L B_0\,\langle|\nabla\psi|\rangle}\lim_{k\to\infty}\overline{W_{(k)}\lambda_{(k)}B(\mathbf{z}_{(k)})} && (5.54)\\
&= -\frac{3}{\rho_L B_0\,\langle|\nabla\psi|\rangle}\lim_{K\to\infty}\frac{1}{K}\sum_{k=0}^{K}\overline{W_{(k)}\lambda_{(k)}B(\mathbf{z}_{(k)})}, && (5.55)
\end{aligned}$$

where

$$W_{(k)} = \sum_{j=0}^{k} w_{(j)} = \psi(\mathbf{z}_{(k)}) - \psi(\mathbf{z}_{(0)}) \tag{5.56}$$

is an integral of $\dot{\psi}$ along a stochastic orbit (total test particle displacement over ψ). The sum in (5.56) actually represents the integration formula which is linear in Δt for the linearized radial equation of motion (see the algorithm below (5.19) and the recurrence relation (5.22)). For simplicity, the proof that $W_{(k)}$ corresponds to the radial displacement modeled exactly is omitted here in favor of the above argument. Nevertheless, in the computations $W_{(k)}$ is calculated integrating the radial equation of motion in the same manner as the rest of drift equations, i.e. using a high order Runge–Kutta algorithm (see Section 5.1). Such a procedure of evaluating averages corresponds to a standard δf method [3, 6, 7]. For a tokamak, the variance of λ_{bb} for this method does not scale with the collisionality, and the required CPU time scales linearly with l_c/L_c. However, for stellarators the variance of λ_{bb} again recovers the scaling $(l_c/L_c)^2$ because due to the non-zero bounce-averaged drift of trapped particles large contributions to $W_{(k)}$ are acquired, which scale as $\dot{\psi} l_c/v$. These contributions are weakly correlated with the values of $\lambda_{(k)}$ which test particles have after detrapping. This is due to the fact that detrapping probabilities to the co-passing and to the counter-passing phase space regions weakly depend on test particle position in the magnetic well and are almost equal as long as this particle is deeply trapped. Therefore, weight generated in the phase space regions of deeply trapped particles reaches co-passing or counter-passing phase space regions with almost equal probabilities and therefore in average is compensated statistically in λ_{bb}. Numerically this results in statistical compensation of large random numbers which introduces large variance in the computation. To overcome this problem in a standard δf method, the test particle motion is limited to an annulus, $\psi_0 - \delta\psi < \psi < \psi_0 + \delta\psi$, so that test particles which leave the annulus (particles with large $W_{(k)}$) are replaced with particles from the equilibrium distribution (5.49) with $W_{(k)} = 0$ (new particles are placed at the middle of the annulus). This means that large weights are filtered out. In order to reduce the noise effectively, the size of this annulus, $\delta\psi$, should be small enough to avoid systematic errors (bias) in the result, and the annulus width should be larger than the particle displacement during a collision time. If the second condition is properly satisfied, practically no noise reduction for the bootstrap coefficient λ_{bb} will be achieved. If it is not satisfied, the simultaneously computed transport coefficient D_{mono} becomes biased, although for the computation of D_{mono} filtering would not be necessary at all. In Ref. 7 this condition has been violated for sake of good convergence of the bootstrap coefficient where the bias still remained small. A procedure which is formally free of such bias and which does not need additional calculations for the control of the bias is therefore of interest.

Chapter 6

Variance reduction

6.1 Splitting of the source

For a formally "unbiased" method it is convenient to split the source in (5.15) into "passing" and "trapped" sources $Q_p = \chi Q$ and $Q_t = Q - Q_p$ using

$$\chi = \frac{1}{2}\left[1 + \tanh\left(\frac{|\lambda| - \lambda_{t-p}}{\Delta\lambda}\right)\right], \tag{6.1}$$

where λ_{t-p} is the pertinent trapped-passing boundary (see Fig. 6.1), and solve the problem with each source independently. Results for transport coefficients for these two sources are added up at the end. The problem with Q_p is solved with the standard method without using an annulus limiting the test particle motion. Since accumulation of large weights is avoided for this source, the convergence of the bootstrap coefficient is similar to that in a tokamak.

6.2 Algorithm for the "trapped" problem

For the treatment of the problem with Q_t one should notice the following. In both formulas for the bootstrap coefficient, Eq. (5.27) and Eq. (5.55), this coefficient is defined by a time average of a test particle weight multiplied with λ. As long as a test particle is trapped it produces practically no contribution to λ_{bb} due to this averaging and the change of sign of λ at the reflection points. Therefore, trapped particles with large weights

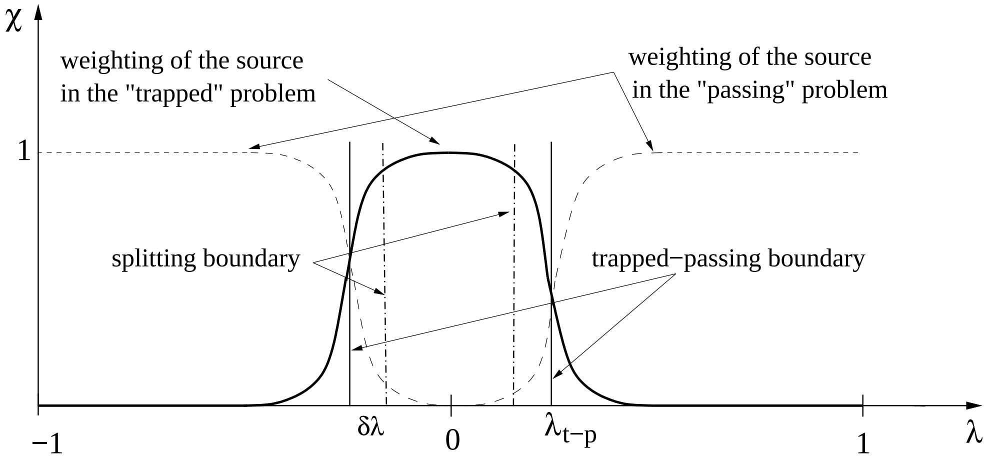

Figure 6.1: Separation of the source in "trapped" and "passing" problems. The "splitting boundary" is located at a distance $\delta\lambda = 2\Delta\lambda$ away from the trapped-passing boundary, where $\Delta\lambda$ is the width of the boundary layer.

start to produce the noise in λ_{bb} only after detrapping. On the other hand, the total weight generated by Q_t in the phase space is zero. This is obvious in the case of stellarator symmetry because of $Q(-\mathbf{z}) = -Q(\mathbf{z})$, but this is also true in a general case for the total source Q. In the general case the average of Q_t can be made zero also by re-defining the function χ in terms of invariants of motion instead of λ. Particles with different signs of the weight detrapped from different magnetic wells quickly mix up in the close vicinity of the boundary layer so that each phase space volume element in this region contains both, particles with positive and negative weights if the number of test particles is large enough. The total weight in such a volume element which actually determines the distribution function being of relevance for the averages is smaller than the sum of the modulus of test particle weights contained in this element. Therefore a periodic re-discretization procedure which replaces all particles in the phase space volume element ("cell") with fewer particles with equal weights which carry the total weight in this element would lead to a significant reduction in the test particle number. It should be noted however, that the number of cells needed for re-discretization in the 3D phase space without significant bias from the finite size of the cells must be large and usually exceeds the number of test particles. Therefore, certain time averaging is needed for an effective re-discretization procedure. In order to introduce such a procedure, the formal solution to (5.15) can be presented as

$$F = F_M + \Delta F_M \,, \tag{6.2}$$

where F_M satisfies an equation which differs from (5.15) only by a source term

$$F_M = \mathcal{K} F_M + Q_M \,, \tag{6.3}$$

where

$$\begin{aligned} Q_M &= \frac{1}{M} \sum_{k=0}^{M-1} \mathcal{K}^k Q = Q_M(Q) \,, & (6.4) \\ \Delta F_M &= \sum_{k=0}^{M-1} \left(1 - \frac{k+1}{M}\right) \mathcal{K}^k Q = \Delta F_M(Q) \,. & (6.5) \end{aligned}$$

In order to derive this form of integral equation the original equation is re-written according to

$$\begin{aligned} F &= Q + \mathcal{K} F & (6.6) \\ &= Q + \mathcal{K} Q + \mathcal{K}^2 F & (6.7) \\ &= \ldots & (6.8) \\ &= \sum_{k=0}^{m-1} \mathcal{K}^k Q + \mathcal{K}^m F \,, & (6.9) \end{aligned}$$

where m is an arbitrary natural number. Averaging the right hand side over $1 \leq m \leq M$ yields

$$\begin{aligned} F &= \frac{1}{M} \sum_{m=1}^{M} \sum_{k=0}^{m-1} \mathcal{K}^k Q + \frac{1}{M} \sum_{m=1}^{M} \mathcal{K}^m F & (6.10) \\ &= \Delta F_M + \frac{1}{M} \sum_{m=0}^{M-1} \mathcal{K}^m Q + \frac{1}{M} \sum_{m=1}^{M} \mathcal{K}^m F \,. & (6.11) \end{aligned}$$

Denoting the last two terms in (6.11) with F_M and substituting there F

in the form of the series (5.21) one obtains

$$\begin{aligned}
F_M &\equiv \frac{1}{M}\left(\sum_{m=0}^{M-1}\mathcal{K}^m Q + \sum_{m=1}^{M}\mathcal{K}^m F\right) && (6.12)\\
&= \frac{1}{M}\left(\sum_{m=0}^{M-1}\mathcal{K}^m Q + \sum_{m=1}^{M}\mathcal{K}^m \sum_{k=0}^{\infty}\mathcal{K}^k Q\right) && (6.13)\\
&= \frac{1}{M}\left(\sum_{m=0}^{M-1}\mathcal{K}^m Q + \mathcal{K}\sum_{k=0}^{\infty}\mathcal{K}^k \sum_{m=0}^{M-1}\mathcal{K}^m Q\right) && (6.14)\\
&= \sum_{k=0}^{\infty}\mathcal{K}^k \frac{1}{M}\sum_{m=0}^{M-1}\mathcal{K}^m Q && (6.15)\\
&= \sum_{k=0}^{\infty}\mathcal{K}^k Q_M\,. && (6.16)
\end{aligned}$$

The last expression is a series solution to equation (6.3). Equation (6.3) describes one iteration of the solution procedure which results in

$$F = \sum_{i=1}^{\infty}\Delta F_M^{(i)}\,, \tag{6.17}$$

with

$$\Delta F_M^{(i)} = \Delta F_M\left(Q^{(i)}\right), \tag{6.18}$$

and

$$Q^{(i)} = Q_M\left(Q^{(i-1)}\right)\,, \tag{6.19}$$

where

$$Q^{(1)} = Q_t\,. \tag{6.20}$$

In accordance to (6.17), the averages are given by

$$\begin{aligned}
D_{\mathrm{mono}} &= \lim_{N_{\mathrm{it}}\to\infty}\sum_{i=1}^{N_{\mathrm{it}}} D_{\mathrm{mono}}^{(i)}\,, && (6.21)\\
\lambda_{bb} &= \lim_{N_{\mathrm{it}}\to\infty}\sum_{i=1}^{N_{\mathrm{it}}} \lambda_{bb}^{(i)}\,, && (6.22)
\end{aligned}$$

where $D^{(i)}_{\mathrm{mono}}$ and $\lambda^{(i)}_{bb}$ are given by Eqs. (5.4) and (5.5), respectively, with the substitution

$$\hat{f} = g^{-1/2} F^{(i)}_M \, , \tag{6.23}$$

and N_{it} is the number of iterations. The first iteration is performed using a standard δf method advancing N test particles initially distributed according to (5.25) by $M-1$ steps so that each of them gains the (random) weight

$$W_{(M-1)} = \sum_{j=0}^{M-1} \left(1 - \chi(\mathbf{z}_{(j)})\right) \dot{\psi}(\mathbf{z}_{(j)}) \Delta t \tag{6.24}$$

and the averages are estimated as an ensemble average

$$\begin{aligned} D^{(1)}_{\mathrm{mono}} &\approx -\frac{1}{\langle|\nabla\psi|\rangle^2} \frac{1}{N} \sum_{\mathit{particles}} W_{(M-1)} \dot{\psi}(\mathbf{z}_{(M-1)}), &(6.25)\\ \lambda^{(1)}_{bb} &\approx -\frac{3}{\rho_L B_0 \langle|\nabla\psi|\rangle} \frac{1}{N} \sum_{\mathit{particles}} W_{(M-1)} \lambda_{(M-1)} B(\mathbf{z}_{(M-1)}). &(6.26) \end{aligned}$$

Starting from the second iteration the algorithm with constant weights is used. For this purpose, in accordance with (6.4), the weight of each test particle is changed to

$$w = W_{(M-1)}/M \, , \tag{6.27}$$

where $W_{(M-1)}$ is its weight after the first iteration, and these particles are again advanced by $M-1$ steps with these fixed weights. During each such step their weights are counted on the 3D grid in phase space producing in this way a source term $Q^{(3)}$ for the next iteration while the contribution to the averages is computed directly as

$$\begin{aligned} D^{(i)}_{\mathrm{mono}} &\approx -\frac{1}{\langle|\nabla\psi|\rangle^2} \frac{1}{N} \sum_{\mathit{particles}} w \sum_{k=0}^{M-1} \dot{\psi}(\mathbf{z}_{(k)}), &(6.28)\\ \lambda^{(i)}_{bb} &\approx -\frac{3}{\rho_L B_0 \langle|\nabla\psi|\rangle} \frac{1}{N} \sum_{\mathit{particles}} w \sum_{k=0}^{M-1} \lambda_{(k)} B(\mathbf{z}_{(k)}), &(6.29) \end{aligned}$$

where $i = 2$ and starting positions $\mathbf{z}_{(0)}$ are the final positions $\mathbf{z}_{(M-1)}$ of the first iteration. Finally, for the third and all further iterations test particles are generated from the source determined on the grid. Namely, in accordance with (6.4), the weight scored in each grid cell during a previous iteration is divided by M thus giving w_{cell}. Then test particles with a prescribed weight modulus $w_{(0)}$ are generated in grid cell centers with a probability proportional to $|w_{cell}|/w_{(0)}$ and signs of their weights w given by the sign of the pertinent w_{cell}.

Note that in computations of the parallel conductivity coefficient the variance does not show up a strong dependence on the collisionality parameter, therefore variance reduction techniques are not applied in computations of this coefficient and the procedure described in chapter 5 can be directly used for the calculations.

6.3 Splitting of particles in the passing region

The prescribed weight $w_{(0)}$ is different in the "trapped" and "passing" regions of the phase space separated by a splitting boundary as shown in Fig. 6.1. These weights are prescribed after the second iteration as

$$w^t_{(0)} = \frac{1}{N}\sum_{cells} |w_{cell}| \,, \tag{6.30}$$

$$w^p_{(0)} = w^t_{(0)}/n_{split} \,, \tag{6.31}$$

where t denotes trapped, p denotes passing and n_{split} is chosen in order to make the number of test particles in both phase space regions roughly the same. In the long mean free path regime, the weight contained in the "trapped" region is large compared to the weight in the "passing" region. In addition, test particles with $w^t_{(0)}$ which cross the splitting boundary and enter the passing region during the iteration are also split into n_{split} particles. Since prescribed weights stay further unchanged, the total number of test particles is decreasing with iterations due to annihilation of their weights on the grid (see Fig. 6.2). Despite the decreasing number of test particles, contributions to the averages from iterations $i \geq 3$ are also determined by (6.28) and (6.29) with the same value of N as for the first iteration.

The number of steps M for a single iteration is chosen to be much smaller than collision time and large enough in order to fill the grid using a limited

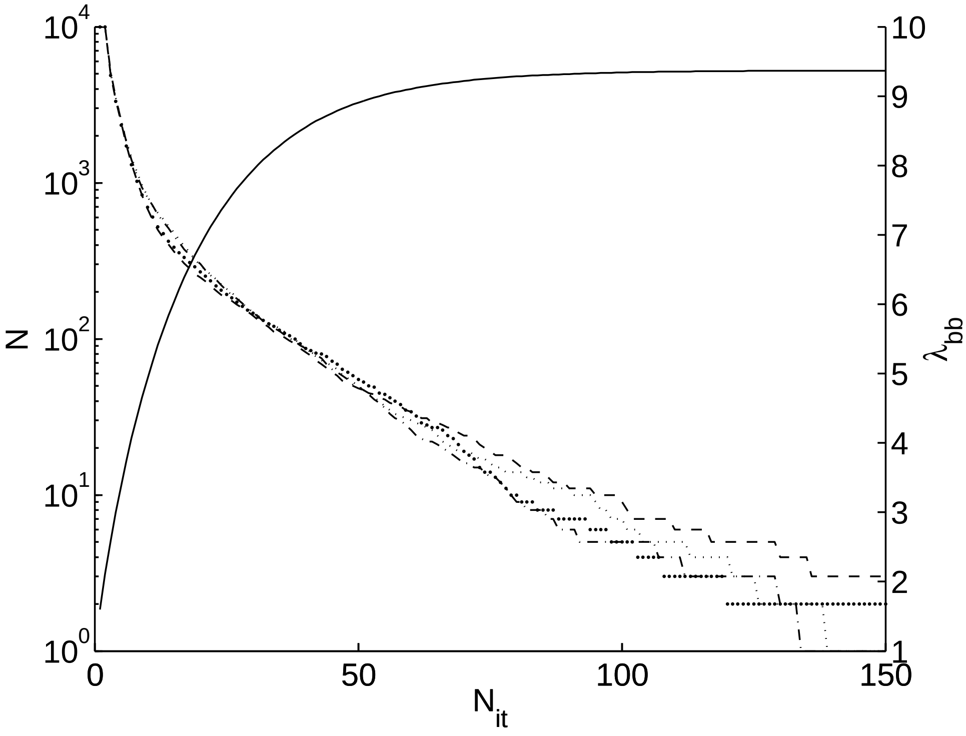

Figure 6.2: Number of simulation particles N for four sub-runs (left axis, dashed lines) and final value of the bootstrap coefficient λ_{bb} computed from 40 sub-runs (right axis, solid line) versus number of iterations N_{it}. Here, 150 iterations approximately correspond to five collision times.

number of test particles. Since the filtering (limitation of test particle motion by the annulus) is not used in the procedure described above, the main source of the bias besides the negligible small error in the Monte Carlo operator may come from the re-discretization procedure. In order to keep this error within predefined limits, a rather large size of the grid over ϑ and φ was chosen, 100x100, while the size of the grid over the pitch parameter λ is chosen so that the grid cell width over λ is smaller with a certain tolerance than the diffusive change in pitch after a re-discretization time $iM\Delta t$. Iterations are continued until no particles are left for the next iteration. Typically, this corresponds to $iM\Delta t$ equal to a few collision times (see Fig. 6.2). At this point the result is fully converged, the convergence with iteration number is exponential.

6.4 Physical parameters

6.4.1 Width of the boundary layer

The width of the boundary layer $\Delta\lambda_{bl}$ is determined by the diffusive change of the particle pitch parameter λ due to collisions during a bounce time t_b according to

$$\nu_c = \frac{(\Delta\lambda_{bl})^2}{2t_b} \,, \tag{6.32}$$

where ν_c is the collision frequency. In terms of the mean free path $l_c = v/\nu_c$ and the connection length $L_c \approx v\, t_b$ this quantity can be written as

$$\Delta\lambda_{bl} \sim \sqrt{\frac{L_c}{l_c}} = \sqrt{\bar{\nu}} \,, \tag{6.33}$$

where v is the particle velocity and $\bar{\nu} = L_c/l_c$ is the collisionality parameter.

6.4.2 Re-discretization length

The re-discretization length in the trapped region τ_{rd}^{tr} is given by

$$\tau_{rd}^{tr} = \sqrt{L_c l_c} = L_c \frac{1}{\sqrt{\bar{\nu}}} \,, \tag{6.34}$$

and the re-discretization length in the passing region τ_{rd}^{pa} is given by

$$\tau_{rd}^{pa} = l_c = L_c \frac{1}{\bar{\nu}} \,. \tag{6.35}$$

6.4.3 Change in pitch parameter during a re-discretization step

The change of the pitch parameter $\Delta\lambda$ during a re-discretization time t_{rd} is related to the collision frequency according to

$$\nu_c = \frac{(\Delta\lambda)^2}{2t_{rd}} \,, \tag{6.36}$$

and can be expressed as

$$\Delta\lambda \sim \sqrt{\frac{t_{rd}}{t_c}} = \sqrt{\frac{\tau_{rd}}{l_c}} \,, \tag{6.37}$$

where t_c is the collision time and τ_{rd} is the distance associated to t_{rd}. In the trapped region this quantity becomes with equation (6.34)

$$\Delta\lambda \sim \sqrt{\frac{L_c}{\sqrt{\bar{\nu}}} \frac{1}{l_c}} = \bar{\nu}^{1/4} \,. \tag{6.38}$$

6.4.4 De-correlation length – passing region

A passing particle with a velocity $v_\parallel$ travels a distance $l = v_\parallel t$ during a time t. The change of distance Δl due to the change in parallel velocity $v_\parallel$ is then given by

$$\Delta l = \Delta v_\parallel t \,, \tag{6.39}$$

where

$$\Delta v_\parallel = \sqrt{\nu_c \, t} \, v_T \,. \tag{6.40}$$

The correlation to the starting point is assumed to be lost if Δl is of the order of the connection length L_c

$$\Delta l \geq L_c \,. \tag{6.41}$$

From the criterion (6.41) one gets with equations (6.39) and (6.40)

$$\sqrt{\nu_c}\, v_T\, t^{3/2} \geq L_c\,. \tag{6.42}$$

Substituting the mean free path $l_c = v_T/\nu_c$, the de-correlation length $L_D = v_T t$ can be expressed as

$$L_D \geq l_c^{1/3} L_c^{2/3} = L_c \bar{\nu}^{-1/3}\,. \tag{6.43}$$

6.4.5 Re-discretization length adjusted to grid mesh size

Particles trapped in one and the same ripple of the magnetic field carry either positive or negative weights (determined by the sign of their radial velocities). Therefore the particle distribution has to evolve for a defined time in order to ensure that positive and negative weights mix up on the grid and allow for an efficient re-discretization procedure. This minimum re-discretization length τ_{rd}^{min} is given by

$$\tau_{rd}^{min} = L_c \left(\frac{L_c}{l_c}\right)^{-1/3}\,. \tag{6.44}$$

The change in pitch parameter of particles which have passed this distance is

$$\Delta\lambda = \varepsilon \sqrt{\frac{\tau_{rd}}{l_c}}\,, \tag{6.45}$$

and the associated number of grid cells N_λ is given by

$$N_\lambda = \frac{1}{\varepsilon}\sqrt{\frac{l_c}{\tau_{rd}}}\,, \tag{6.46}$$

where ε is an accuracy parameter and τ_{rd} is the re-discretization length. In order to ensure that on average each cell of the grid contains at least one count the following condition has to hold

$$N_{part}\frac{\tau_{rd}}{h_s} > N_\varphi\, N_\vartheta\, N_\lambda\,, \tag{6.47}$$

where N_φ, N_ϑ and N_λ are the number of grid cells in φ, ϑ and λ, respectively. Here, h_s is the step size of numerical integration and N_{part} is the number of particles. Substituting equation (6.46) into equation (6.47) yields

$$\tau_{rd} > h_s^{2/3} \left(\frac{N_\varphi N_\vartheta}{\varepsilon}\right)^{2/3} \left(\frac{1}{N_{part}}\right)^{2/3} l_c^{1/3} \,. \tag{6.48}$$

Substituting equation (6.44) into equation (6.48) the re-discretization length can be written as

$$\tau_{rd} > h_s^{2/3} \left(\frac{N_\varphi N_\vartheta}{\varepsilon}\right)^{2/3} \left(\frac{1}{N_{part}}\right)^{2/3} \tau_{rd}^{min} L_c^{-2/3} \,. \tag{6.49}$$

6.4.6 Relaxation due to parallel diffusion

The diffusion coefficient $D_\parallel$ for a diffusion process characterized by the mean free path $l_c = v_T t_c$ can be written as

$$D_\parallel \sim \frac{l_c^2}{2t_c} \sim \frac{v_T^2}{\nu_c} \,. \tag{6.50}$$

The relaxation time t_{rcon} associated to relaxation processes characterized by a multiple number n_{rcon} of connection lengths L_c is given by

$$t_{rcon} \sim \frac{(n_{rcon} L_c)^2}{4D_\parallel} \sim \frac{n_{rcon}^2 L_c^2 \nu_c}{v_T^2} \,. \tag{6.51}$$

The associated distance τ_{rcon} becomes

$$\tau_{rcon} = v_T t_{rcon} \sim n_{rcon}^2 L_c \frac{\nu_c}{\nu_b} \sim n_{rcon}^2 L_c \bar{\nu} \,, \tag{6.52}$$

where $L_c = v_T/\nu_b$ has been substituted and ν_b is the bounce frequency.

6.4.7 Relaxation during multiple collision times

The relaxation time t_{rcol} associated to a multiple number n_{rcol} of collision times t_c is given by

$$t_{rcol} = n_{rcol} t_c = n_{rcol} \frac{1}{\nu_c} \,. \tag{6.53}$$

The corresponding length scale τ_{rcol} can be represented as

$$\tau_{rcol} = v_T t_{rcol} \sim n_{rcol} L_c \frac{\nu_b}{\nu_c} \sim n_{rcol} L_c \frac{1}{\bar{\nu}} \,, \tag{6.54}$$

where t_b is the bounce time and ν_b is the bounce frequency.

Chapter 7

Computations

Transport coefficients are computed by summing the results of two separate computations, one where the source is placed in the "trapped" region and one where the source is placed in the "passing" region (see equation (6.1) and Fig. 6.1). "Trapped" and "passing" regions in phase space are defined by the trapped-passing boundary $\lambda_{t-p} = \sqrt{1 - B/B_{max}}$ which is determined by the module of the local magnetic field B and by the absolute maximum of the magnetic field on the flux surface B_{max}. The splitting boundary is located in a distance two times the width of the boundary layer away from the trapped-passing boundary. In the problem with the source in the "trapped" region cells are assigned to the "trapped" region if the absolute value of their pitch parameter λ is bigger than the absolute value of the pitch parameter λ associated to the splitting boundary. In the problem with the source in the "trapped" region cells are assigned to the "passing" region if the absolute value of their pitch parameter λ is smaller than the absolute value of the pitch parameter λ associated to the splitting boundary. In the problem with the source in the "passing" region cells are assigned to the "trapped" region if the absolute value of their pitch parameter λ is bigger than the absolute value of the pitch parameter λ associated to the trapped-passing boundary. In the problem with the source in the "passing" region cells are assigned to the "passing" region if the absolute value of their pitch parameter λ is smaller than the absolute value of the pitch parameter λ associated to the trapped-passing boundary.

The density distribution on the flux surface is initialized with the normalized value of $\sqrt{g}$ at the center of each cell according to equation (5.25). At the beginning of the simulation as well as after each re-discretization step cells are assigned to categories (see Fig. 7.1) and probability densities d are introduced

$$ {}^{\textit{sign of density}}_{\textit{trapped/passing}}\mathsf{d}^{\textit{sign of pitch variable}}_{\textit{cell index }(3-\textit{dim})} \ . \tag{7.1}$$

These categories take into account the sign of the density in each cell and whether the cell is assigned to the "trapped" or to the "passing" region in phase space. Also, the sign of the pitch variable and the 3-dim index of the cell are taken into account. The weight of a cell which will be simulated with single test particles is evaluated as well as the weight which will be simulated with with pairs of test particles. For this purpose the density in cells with a positive value of the pitch variable and the density in cells with a negative value of the pitch variable is evaluated at each location (cell position) on the flux surface and quantities p are introduced

$$ {}^{\textit{sign of density}}_{\textit{trapped/passing}}\mathsf{p}^{\textit{single/pair}}_{\textit{cell index }(1-\textit{dim})} \ . \tag{7.2}$$

The density which is the same in both cells is simulated with pairs of test particles, which means that two particles are started with different signs of the pitch variable and the same sequence of random numbers is used for the computation of their orbits. These densities are given by

$$\begin{aligned}
{}^{+}_{tr}\mathsf{p}^{p}_{l} &= 2\cdot\mathrm{MIN}\left({}^{+}_{tr}\mathsf{d}^{\lambda+}_{ijk}\ ,\ {}^{+}_{tr}\mathsf{d}^{\lambda-}_{ijk}\right) && (7.3)\\
{}^{+}_{pa}\mathsf{p}^{p}_{l} &= 2\cdot\mathrm{MIN}\left({}^{+}_{pa}\mathsf{d}^{\lambda+}_{ijk}\ ,\ {}^{+}_{pa}\mathsf{d}^{\lambda-}_{ijk}\right) && (7.4)\\
{}^{-}_{tr}\mathsf{p}^{p}_{l} &= 2\cdot\mathrm{MIN}\left({}^{-}_{tr}\mathsf{d}^{\lambda+}_{ijk}\ ,\ {}^{-}_{tr}\mathsf{d}^{\lambda-}_{ijk}\right) && (7.5)\\
{}^{-}_{pa}\mathsf{p}^{p}_{l} &= 2\cdot\mathrm{MIN}\left({}^{-}_{pa}\mathsf{d}^{\lambda+}_{ijk}\ ,\ {}^{-}_{pa}\mathsf{d}^{\lambda-}_{ijk}\right)\ . && (7.6)
\end{aligned}$$

The residual density is simulated with particles with a pitch parameter carrying the sign of the pertinent cell. These densities are given by

$$\begin{aligned}
{}^{+}_{tr}\mathsf{p}^{s}_{l} &= {}^{+}_{tr}\mathsf{d}^{\lambda+}_{ijk} - {}^{+}_{tr}\mathsf{d}^{\lambda-}_{ijk} && (7.7)\\
{}^{+}_{pa}\mathsf{p}^{s}_{l} &= {}^{+}_{pa}\mathsf{d}^{\lambda+}_{ijk} - {}^{+}_{pa}\mathsf{d}^{\lambda-}_{ijk} && (7.8)\\
{}^{-}_{tr}\mathsf{p}^{s}_{l} &= {}^{-}_{tr}\mathsf{d}^{\lambda+}_{ijk} - {}^{-}_{tr}\mathsf{d}^{\lambda-}_{ijk} && (7.9)\\
{}^{-}_{pa}\mathsf{p}^{s}_{l} &= {}^{-}_{pa}\mathsf{d}^{\lambda+}_{ijk} - {}^{-}_{pa}\mathsf{d}^{\lambda-}_{ijk}\ , && (7.10)
\end{aligned}$$

where $l = i \cdot j \cdot k$. Finally there exist eight categories which are assigned to the individual cells on the grid: "trapped" region - positive density

- single ${}^{+}_{tr}\mathsf{p}_l^s$, “trapped” region - positive density - pair ${}^{+}_{tr}\mathsf{p}_l^p$, “trapped” region - negative density - single ${}^{-}_{tr}\mathsf{p}_l^s$, “trapped” region - negative density - pair ${}^{-}_{tr}\mathsf{p}_l^p$, “passing” region - positive density - single ${}^{+}_{pa}\mathsf{p}_l^s$, “passing” region - positive density - pair ${}^{+}_{pa}\mathsf{p}_l^p$, “passing” region - negative density - single ${}^{-}_{pa}\mathsf{p}_l^s$, “passing” region - negative density - pair ${}^{-}_{pa}\mathsf{p}_l^p$.

The probability densities p are stored as cumulative probability densities which means that the above categorizations are done subsequently for all cells and the probability density associated to a certain cell and category is stored as the sum of the contribution from the respective cell plus the contributions from the preceding cells. This is done for all categories of cells and the location of each contribution is recorded.

The total probability density is given by the sum of the probability densities of all cells. With this total probability density and the total number of simulation particles which has been chosen at beginning of the computation the total weight in the simulation can be fixed. The number of particles which has to be simulated for each category is related to the ratio of the pertinent probability density to the total weight. Weights of particles of each category are computed by dividing the respective probability density by the number of particles associated to this category.

Test particles are started to simulate the weight carried by the cells subsequently for the individual categories. For each test particle started, a random number is created and multiplied with the total probability density of the category under investigation. This random probability density corresponds to a certain cell on the grid which can be localized by scanning the cumulative probability densities with the help of a binary search algorithm. This procedure transforms the (uniformly distributed) pseudo random numbers to (non-uniformly distributed) probability densities where cells which have delivered bigger contributions to the cumulative probability densities will be selected more frequently than those with smaller contributions.

The locations of cells selected that way serve as the starting points of test particle orbits which are modeled stepwise in time. One time step consists of advancing a particle along its drift orbit in phase space using an adaptive Runge-Kutta integration followed by a random displacement of the particle pitch parameter modeling the collisions. The number of steps between re-discretizations is chosen in accordance with the re-discretization length (see section 6.4.5). For the first set of steps the standard δf method is applied where particle weights are increasing and defined by the normalized value of the distance between the particles ψ value and the starting flux surface. For the next set of steps particle weights are fixed and the same number of steps is performed once more with constant weights. At this point the total weight of the computation is fixed and the number of particles which has to be run for each category is evaluated. Contributions to the densities as well as to the transport coefficients are computed as described in section 6.2 while running the particles. In the following the re-discretizations of the probability density distributions are continued until no more particles are left which can be run in the simulation.

7.1 NEO-MC

For numerical computations the Fortran 90/95 code NEO-MC has been developed. In order to speed up the computations the batch systems Condor and HTCondor [100], respectively, have been used which allow to run subsets of particles on different CPUs at the same time. Each random number generator on each CPU has to be initialized with a different seed number. In a single subset $N = 10^4$ particles are started for computations with the source in the "trapped" region and $N = 10^3$ particles are started for computations with the source in the "passing" region. Typically, $K = 80$ to $K = 160$ subsets have been computed depending on the desired accuracy. Each of these sub-runs delivers results for the transport coefficients which have to be joined appropriately to get the final value (see Fig. 7.2). The results of the sub-runs are used to estimate the variance of these final values according to

$$\sigma_K^2 \approx \frac{1}{K-1} \sum_{k=1}^{K} \left(A_k - \langle A \rangle_K\right)^2 \ , \tag{7.11}$$

where A_k are the results computed by the individual sub-runs and σ_K is the standard error of the average over sub-runs

$$\langle A \rangle_K = \frac{1}{K} \sum_{k=1}^{K} A_k \, . \tag{7.12}$$

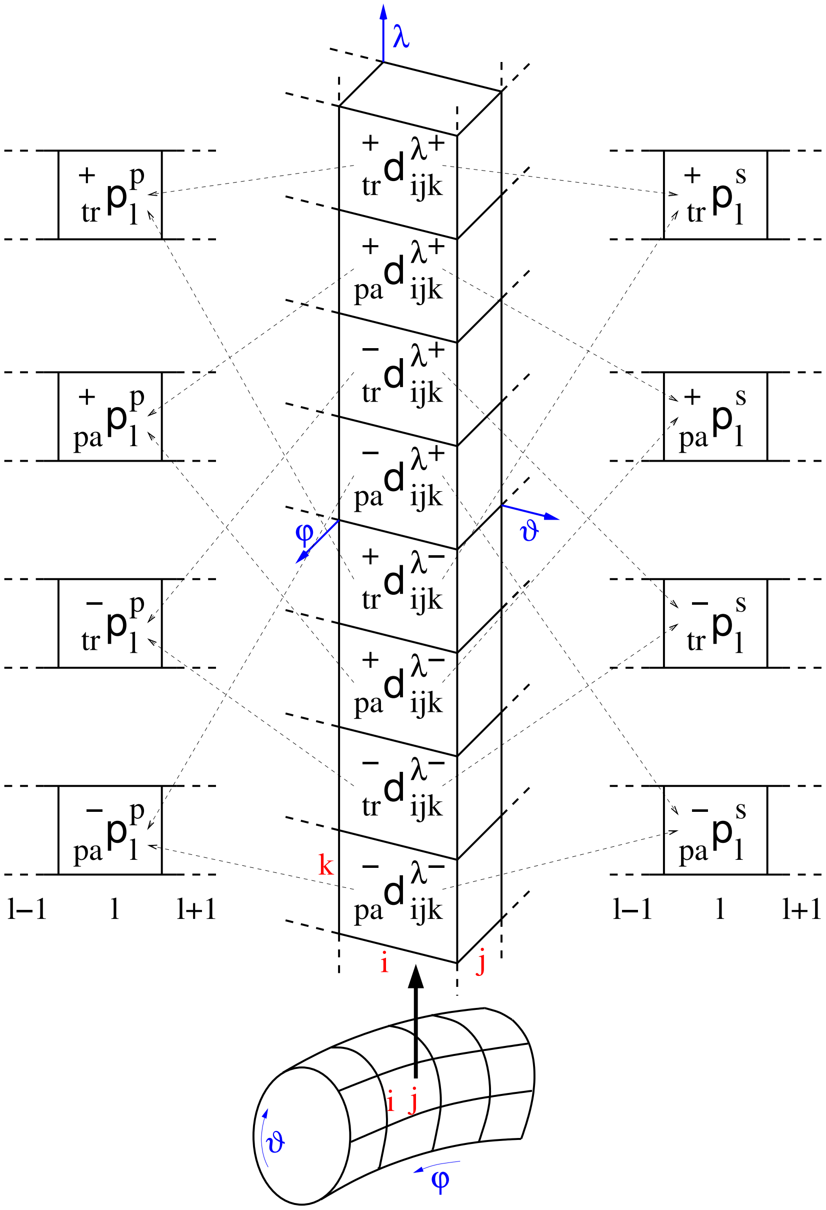

Figure 7.1: Sketch of the grid for the discretization of the probability densities d and p. Explanations are given in the text.

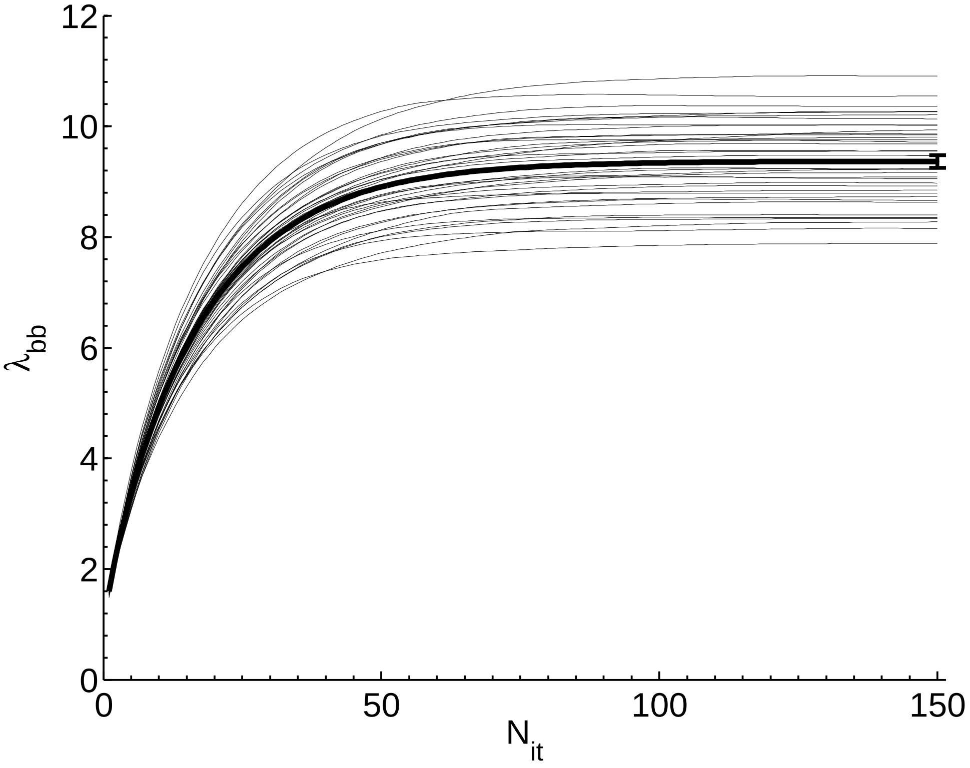

Figure 7.2: Bootstrap coefficient λ_{bb} for each of $K = 40$ sub-runs (thin lines) and the average value (thick line) plotted over the number of iterations N_{it}. The estimated standard deviation σ_K of the final value is shown with an error bar.

In Fig. 6.2 together with the number of test particles the sum entering the limit for λ_{bb} in Eq. (6.22) is plotted over the number of iterations N_{it} for a couple of sub-runs. The change of each λ_{bb} value towards the end of the computation is small due to the fact that at the end of the integration path there are only few test particles remaining which deliver contributions to λ_{bb}. In NEO-MC collisionless drift motion is computed using an adaptive integrator (see Section 5.3). Splitting of the orbits into time steps is necessary for modeling the collisions. For most of the computations, it was sufficient to use step size corresponding to less than 30 steps per magnetic field period by a strictly passing particle. Nevertheless, for high values of the electric field parameter this number of integration steps n_s had to be increased in computations of the mono-energetic diffusion coefficient up to several hundreds in the optimized configurations (Fig. 7.3). In the high collisionality regime even higher values of n_s had to be used in computations of the conductivity coefficient (Fig. 7.4).

7.2 Scaling of variance and computation time

As a result of the described improvements of the δf method, the variance of this method is reduced to the scaling l_c/L_c as compared to the scaling $(l_c/L_c)^2$ of the standard δf method without filtering for the same number of test particles N at the start of the computation. In addition, due to the decay of test particle numbers with iterations, the CPU time needed for the same number of starting particles is also reduced from the usual linear scaling, l_c/L_c, to the scaling $(l_c/L_c)^{1/2}$. As a result, the CPU time needed to achieve a given accuracy by the improved method scales as $(l_c/L_c)^{3/2}$. This can be seen from Fig. 7.5 where normalized run times are shown as functions of collisionality L_c/l_c. The deviations at the higher collisionalities from the expected scaling are caused by the time needed for the precomputation of the magnetic field data which makes up the major part of the total computation time there. For low collisionalities this precomputation time is negligible compared to the time needed for running the particles. Such a scaling is much better than the scaling $(l_c/L_c)^3$ of the standard δf method without a filter.

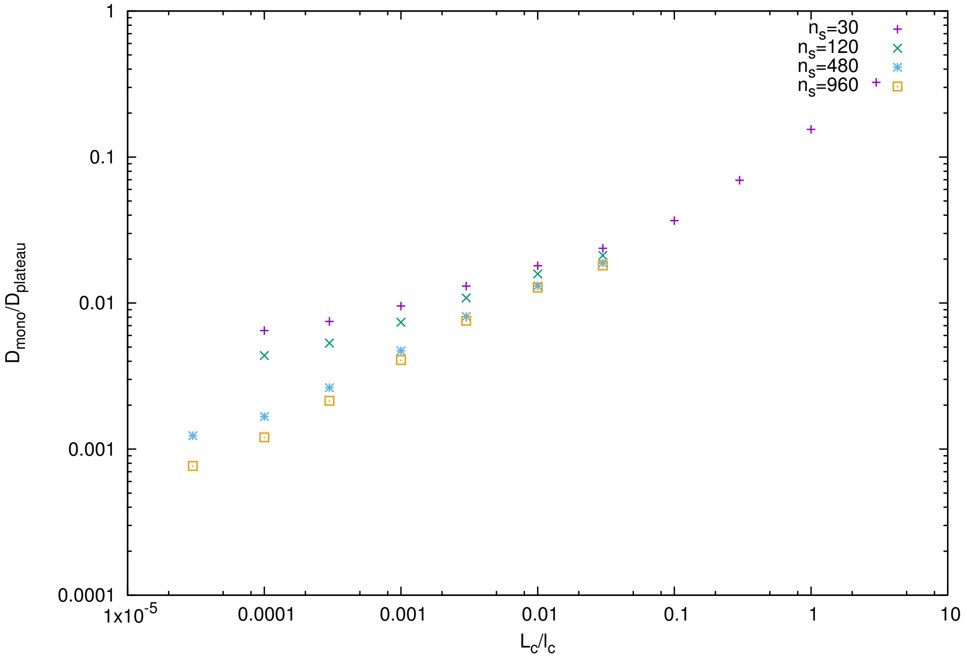

Figure 7.3: Normalized mono-energetic diffusion coefficient $D_{\text{mono}}/D_{\text{plateau}}$ for QIPC vs. collisionality parameter L_c/l_c at half plasma radius computed with different values of the integration step parameter n_s for $E_r/(vB) = 3 \cdot 10^{-3}$.

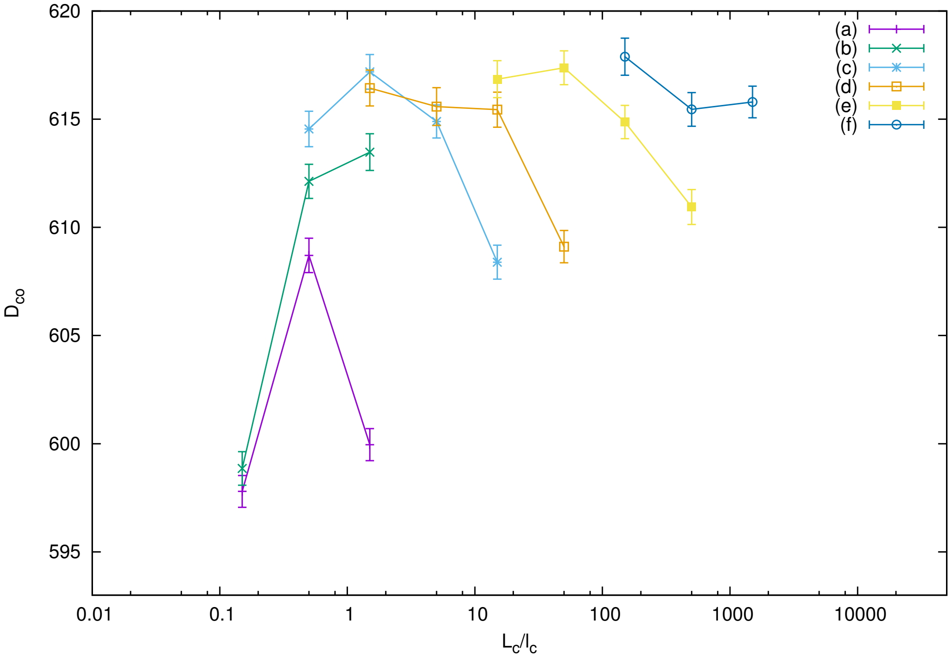

Figure 7.4: Normalized conductivity coefficient D_{co} for NCSX vs. collisionality parameter L_c/l_c at half plasma radius for zero radial electric field parameter computed with $n_s = 120$ (a), 480 (b), 1920 (c), $8 \cdot 10^3$ (d), $8 \cdot 10^4$ (e), $8 \cdot 10^5$ (f).

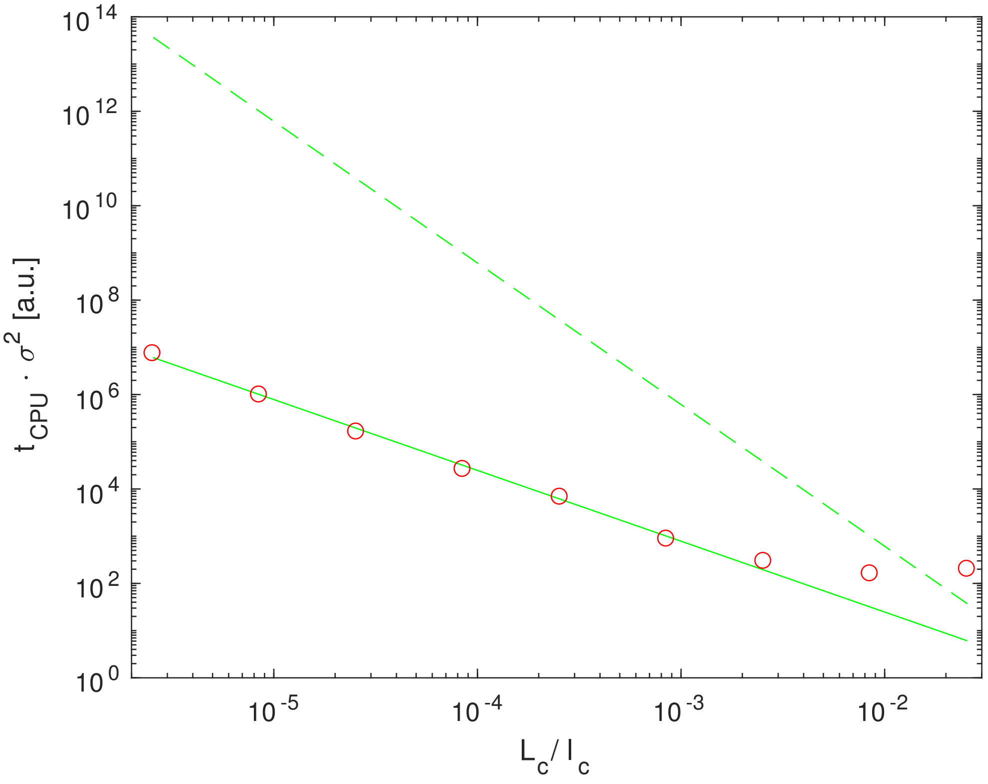

Figure 7.5: CPU-time multiplied with the variance of the bootstrap coefficient σ^2 plotted over the collisionality parameter (circles). The solid line shows the scaling $(l_c/L_c)^{3/2}$, the dashed line shows the scaling $(l_c/L_c)^3$.

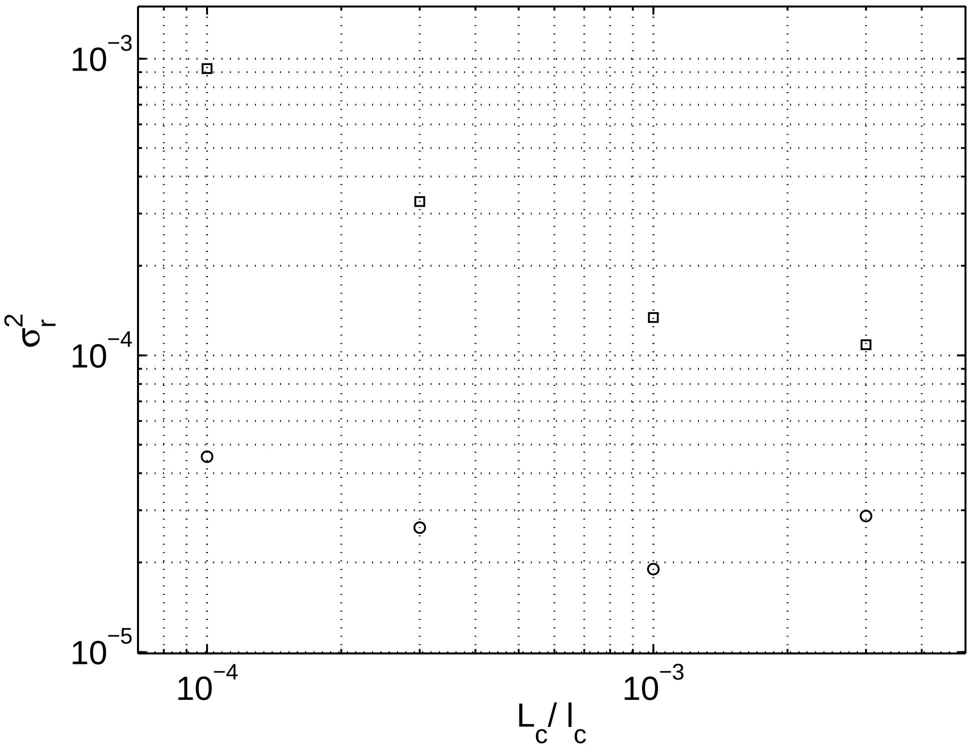

Figure 7.6: Squares of relative statistical errors σ_r^2 of $D_{\mathrm{mono}}/D_{\mathrm{plateau}}$ (circles) and λ_{bb} (squares) for LHD with R=375cm vs. collisionality parameter L_c/l_c at half plasma radius.

In Fig. 7.6 and Fig. 7.7 squares of relative statistical errors σ_r^2, i.e. variances of $D_{\mathrm{mono}}/D_{\mathrm{plateau}}$ (circles) and λ_{bb} (squares) normalized by the squares of the respective average values are shown for LHD with R=375cm and W7-X standard configuration. These quantities scale inversely with the number of test particles and, respectively, with CPU time. Normalized variances of $D_{\mathrm{mono}}/D_{\mathrm{plateau}}$ have weak dependence on collisionality while normalized variances of λ_{bb} scale approximately linearly with the mean free path. This scaling leads to a much larger amount of CPU time needed in the long mean free path regime for computations of λ_{bb} with given accuracy as compared to $D_{\mathrm{mono}}/D_{\mathrm{plateau}}$ computations. Nevertheless, this scaling is much better than quadratic scaling with the mean free path of the variance of the standard delta-f method.

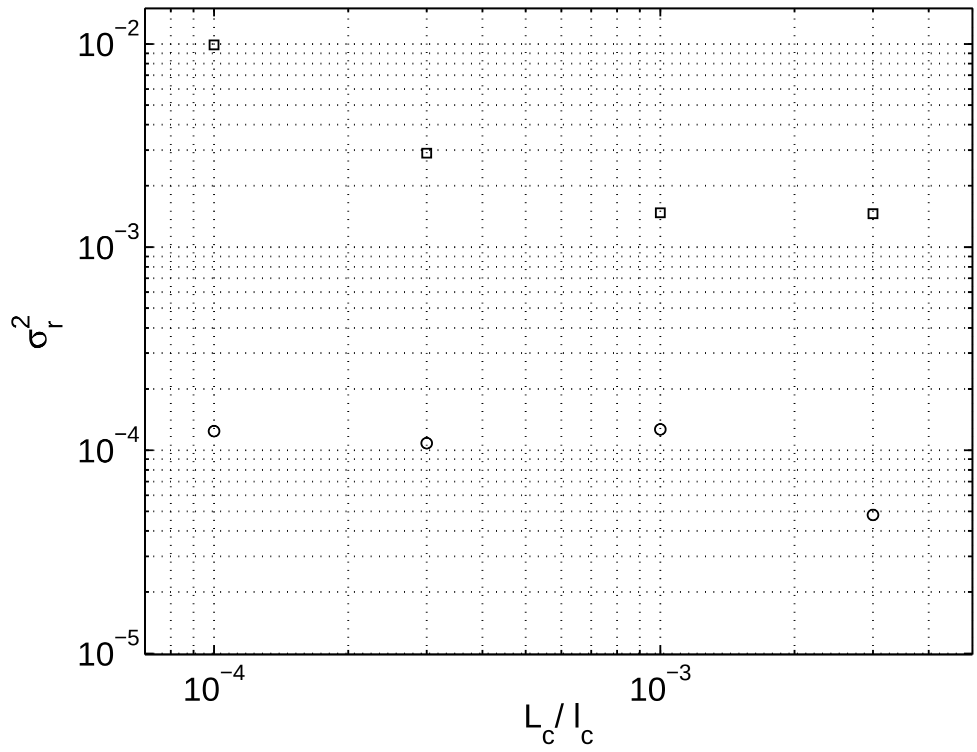

Figure 7.7: Squares of relative statistical errors σ_r^2 of $D_{\mathrm{mono}}/D_{\mathrm{plateau}}$ (circles) and λ_{bb} (squares) for W7-X standard configuration vs. collisionality parameter L_c/l_c at half plasma radius.

It should be noted, that from the viewpoint of re-discretization it would be most effective to start all particles in a single run instead of distributing them to subsets, but from a practical point of view the usage of a computer cluster as for the computations in this work is advantageous for the total computing times as well as for the estimation of variances.

7.3 Magnetic configurations

The magnetic configurations for which the computations have been performed are the Large Helical Device (LHD) [101, 102], a heliotron located at Toki, Japan, (beside the standard configuration also two inward shifted configurations of this device have been investigated); the advanced stellarator Wendelstein 7-X (W7-X) [24, 59, 103, 104], a helias which is in the start-up phase at Greifswald, Germany; the quasi-axisymmetric National Compact Stellarator Experiment (NCSX) [105], designed at Princeton, New Jersey, USA; the Helically Symmetric Experiment (HSX) [106], operating at Madison, Wisconsin, USA; a quasi-isodynamic stellarator [107] with poloidally closed contours of the magnetic field strength (QIPC) [108], taken from the literature; and the heliac TJ-II [25], operating at Madrid, Spain.

7.4 Computational results

Results of computations of the mono-energetic transport coefficients for the magnetic configurations listed in section 7.3 for various values of the collisionality parameter and the electric field parameter can be found in Figs. 7.8 – 7.26. Some of the curves in these figures have been published in [11–23]. The results for regimes with negligible electric fields have been benchmarked with computations by NEO-2 [12, 18, 109] which are also shown in these figures. NEO-2 solves the linearized drift kinetic equation for three-dimensional toroidal magnetic fields and is able to compute, besides various other plasma quantities of interest, mono-energetic neoclassical transport coefficients for regimes with weak plasma rotation. It does not introduce any simplifications on the device geometry or on the Coulomb collision model and is especially efficient in the long mean free path regime. It uses the field line integration technique together with a multiple domain decomposition approach and introduces an adaptive phase space discretization. This allows for an effective resolution of the boundary layers between various classes of trapped and passing particles. Results of benchmarking of computations with finite values of the radial electric field parameter with other methods can be found in Ref. 21. There it is shown that the results of NEO-MC stay in good agreement with computations by other methods such as different δf schemes [7], full-f Monte Carlo simulations [110, 111], the variational approach of the Drift Kinetic Equation Solver (DKES) [66, 112] and a numerical solution of the ripple-averaged kinetic equation (GSRAKE) [113]. Also, an extensive discussion of the results of this benchmarking can be found in this reference.

7.4.1 Diffusion coefficient

The following figures show results of computations of normalized mono-energetic radial diffusion coefficients at half plasma radius for the configurations listed in section 7.3 for confinement regimes with various values of the collisionality parameter and the electric field parameter.

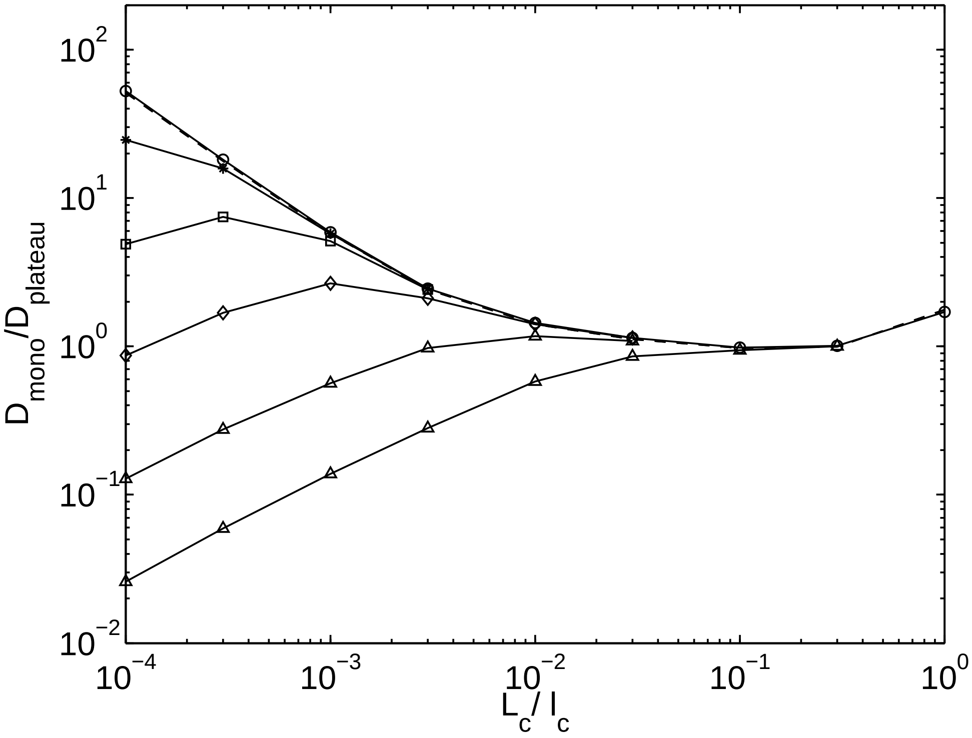

Figure 7.8: Normalized mono-energetic diffusion coefficient $D_{\text{mono}}/D_{\text{plateau}}$ for LHD with R=375cm vs. collisionality parameter L_c/l_c at half plasma radius computed by NEO-MC (solid lines) and NEO-2 (dashed line) for $E_r/(vB) = 0$ (circles), $3 \cdot 10^{-5}$ (stars), $1 \cdot 10^{-4}$ (squares), $3 \cdot 10^{-4}$ (diamonds), $1 \cdot 10^{-3}$ (upper curve with triangles), $3 \cdot 10^{-3}$ (lower curve with triangles).

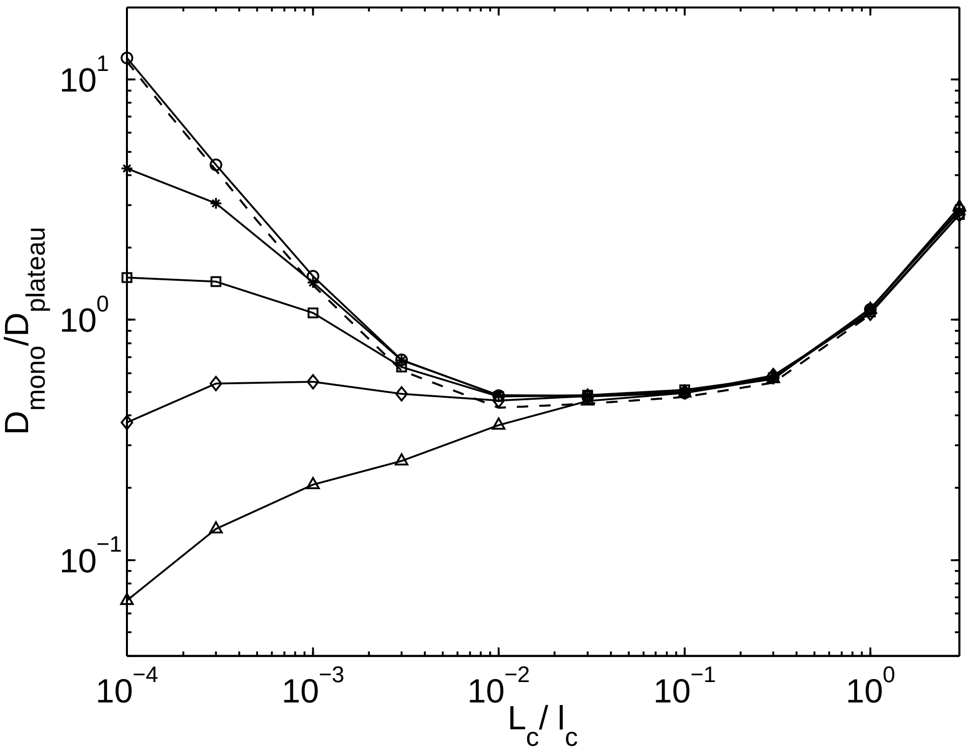

Figure 7.9: Normalized mono-energetic diffusion coefficient $D_{\mathrm{mono}}/D_{\mathrm{plateau}}$ for LHD with R=360cm vs. collisionality parameter L_c/l_c at half plasma radius computed by NEO-MC (solid lines) and NEO-2 (dashed line) for $E_r/(vB) = 0$ (circles), $3 \cdot 10^{-5}$ (stars), $1 \cdot 10^{-4}$ (squares), $3 \cdot 10^{-4}$ (diamonds), $1 \cdot 10^{-3}$ (triangles).

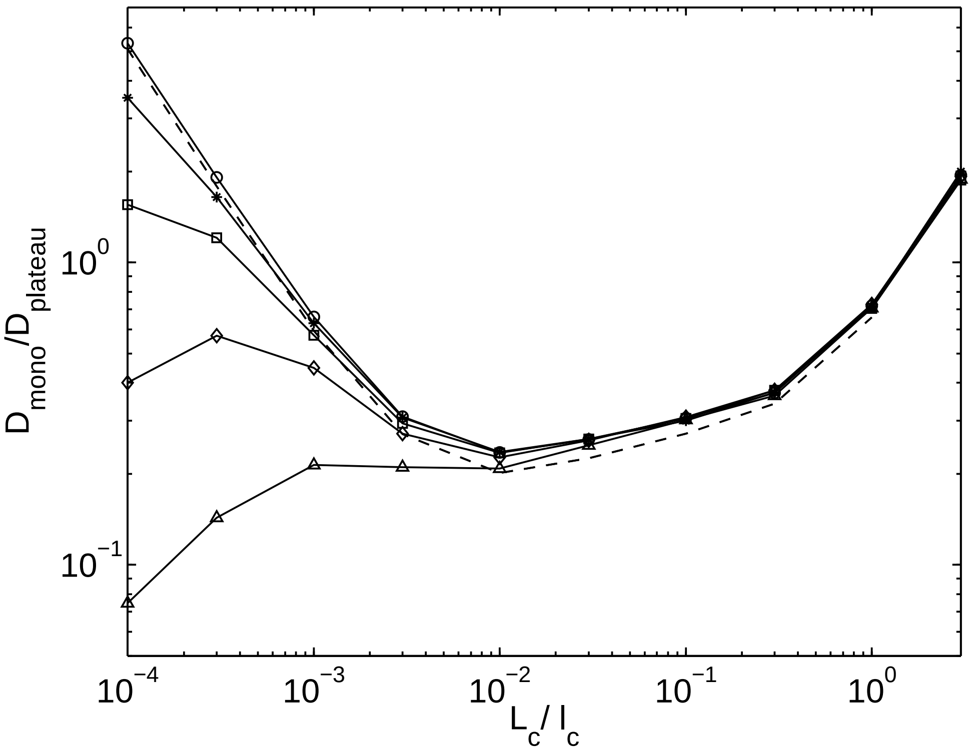

Figure 7.10: Normalized mono-energetic diffusion coefficient $D_{\mathrm{mono}}/D_{\mathrm{plateau}}$ for LHD with R=353cm vs. collisionality parameter L_c/l_c at half plasma radius computed by NEO-MC (solid lines) and NEO-2 (dashed line) for $E_r/(vB) = 0$ (circles), $3 \cdot 10^{-5}$ (stars), $1 \cdot 10^{-4}$ (squares), $3 \cdot 10^{-4}$ (diamonds), $1 \cdot 10^{-3}$ (triangles).

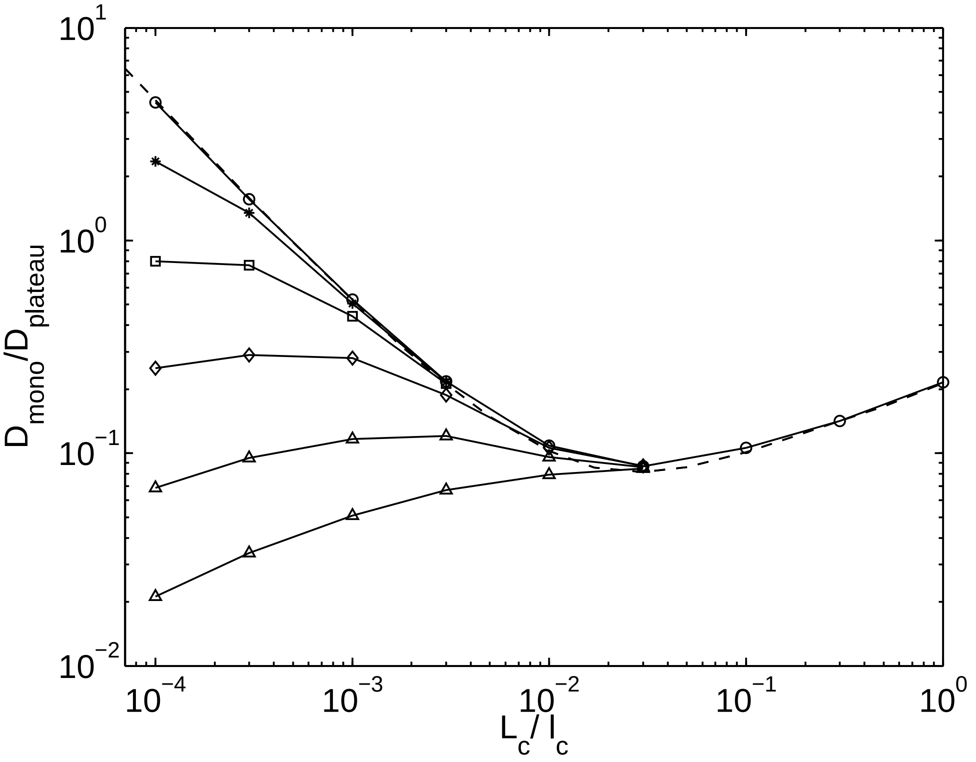

Figure 7.11: Normalized mono-energetic diffusion coefficient $D_{\mathrm{mono}}/D_{\mathrm{plateau}}$ for W7-X standard configuration vs. collisionality parameter L_c/l_c at half plasma radius computed by NEO-MC (solid lines) and NEO-2 (dashed line) for $E_r/(vB) = 0$ (circles), $3 \cdot 10^{-5}$ (stars), $1 \cdot 10^{-4}$ (squares), $3 \cdot 10^{-4}$ (diamonds), $1 \cdot 10^{-3}$ (upper curve with triangles), $3 \cdot 10^{-3}$ (lower curve with triangles).

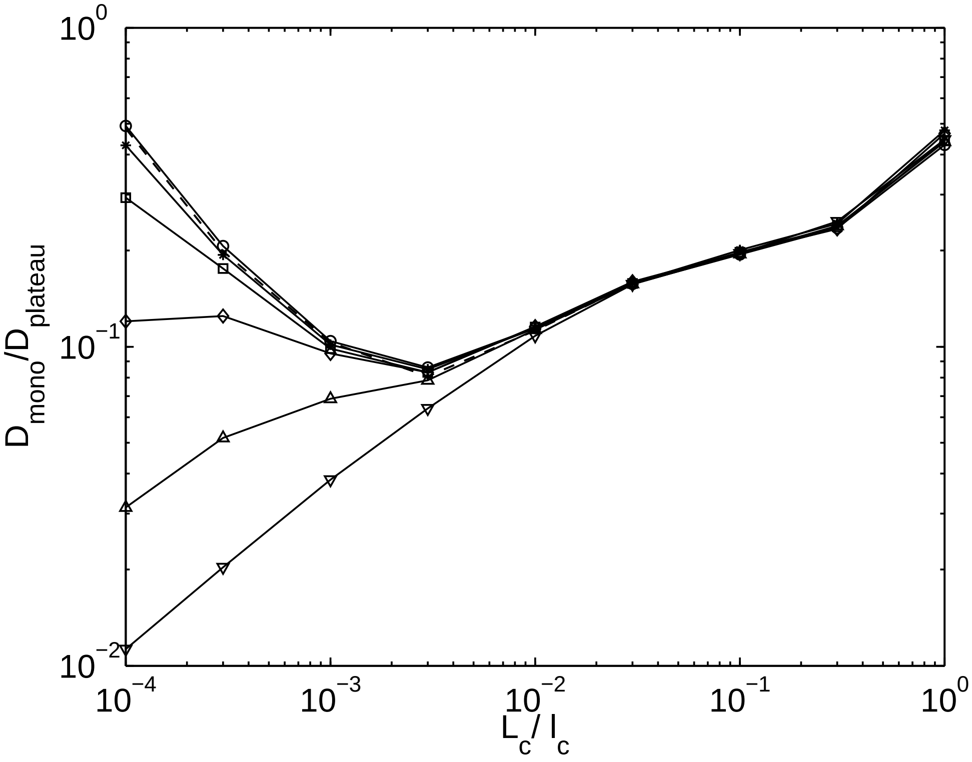

Figure 7.12: Normalized mono-energetic diffusion coefficient $D_{\mathrm{mono}}/D_{\mathrm{plateau}}$ for NCSX vs. collisionality parameter L_c/l_c at half plasma radius computed by NEO-MC (solid lines) and NEO-2 (dashed line) for $E_r/(vB) = 0$ (circles), $3 \cdot 10^{-5}$ (stars), $1 \cdot 10^{-4}$ (squares), $3 \cdot 10^{-4}$ (diamonds), $1 \cdot 10^{-3}$ (upwards triangles), $3 \cdot 10^{-3}$ (downwards triangles).

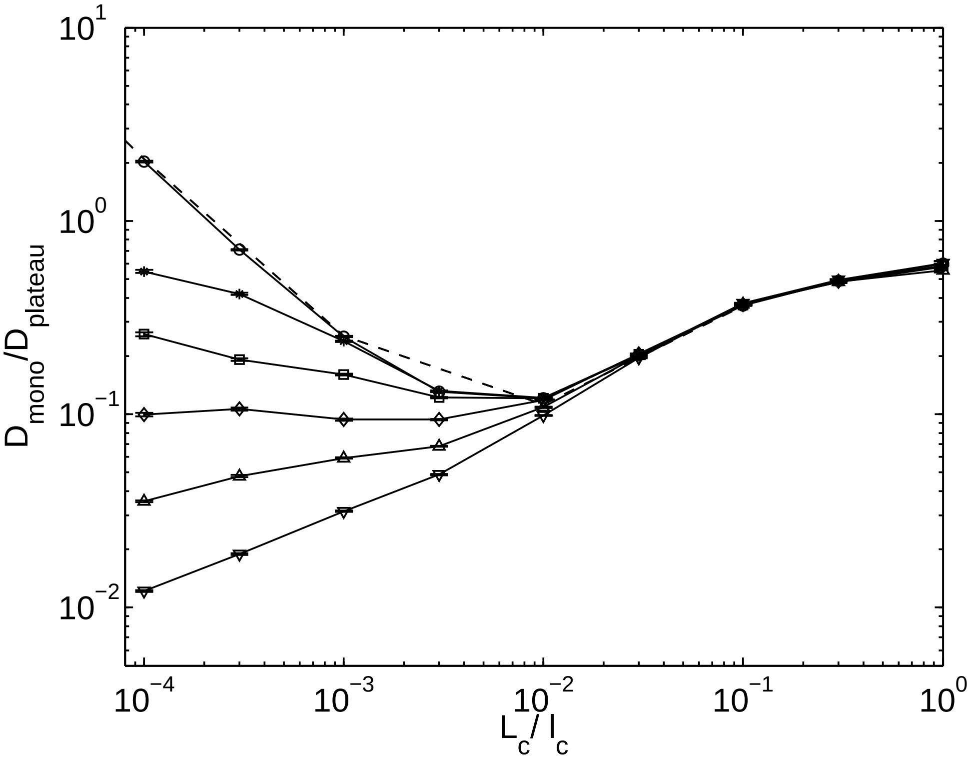

Figure 7.13: Normalized mono-energetic diffusion coefficient $D_{\mathrm{mono}}/D_{\mathrm{plateau}}$ for HSX vs. collisionality parameter L_c/l_c at half plasma radius computed by NEO-MC (solid lines) and NEO-2 (dashed line) for $E_r/(vB) = 0$ (circles), $3 \cdot 10^{-5}$ (stars), $1 \cdot 10^{-4}$ (squares), $3 \cdot 10^{-4}$ (diamonds), $1 \cdot 10^{-3}$ (upwards triangles), $3 \cdot 10^{-3}$ (downwards triangles).

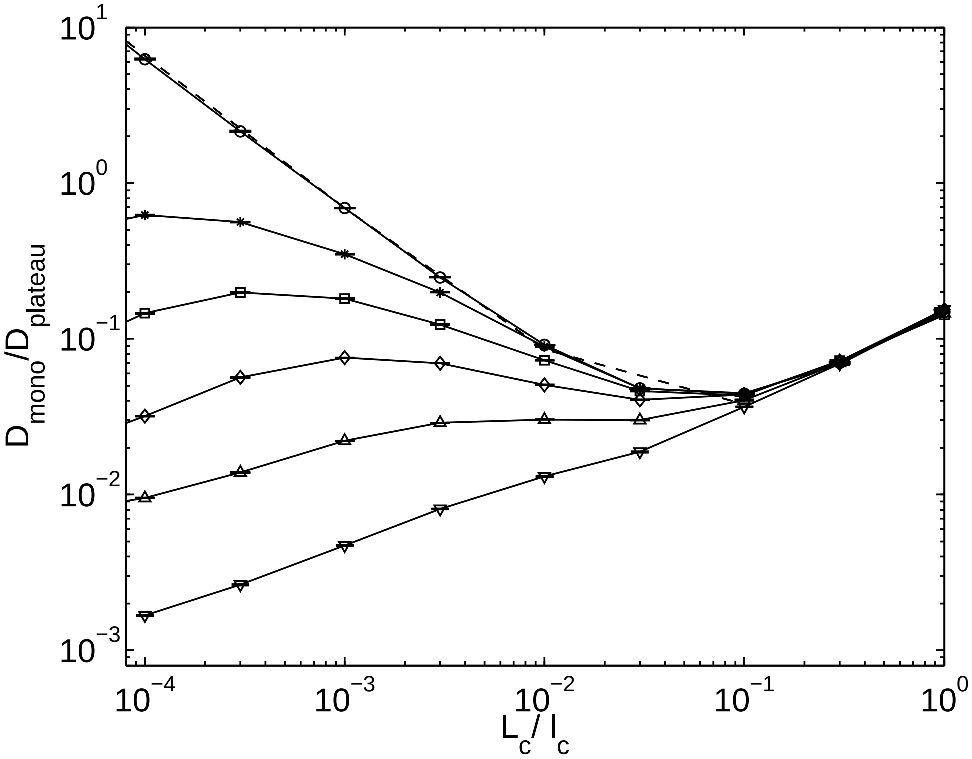

Figure 7.14: Normalized mono-energetic diffusion coefficient $D_{\mathrm{mono}}/D_{\mathrm{plateau}}$ for QIPC vs. collisionality parameter L_c/l_c at half plasma radius computed by NEO-MC (solid lines) and NEO-2 (dashed line) for $E_r/(vB) = 0$ (circles), $3 \cdot 10^{-5}$ (stars), $1 \cdot 10^{-4}$ (squares), $3 \cdot 10^{-4}$ (diamonds), $1 \cdot 10^{-3}$ (upwards triangles), $3 \cdot 10^{-3}$ (downwards triangles).

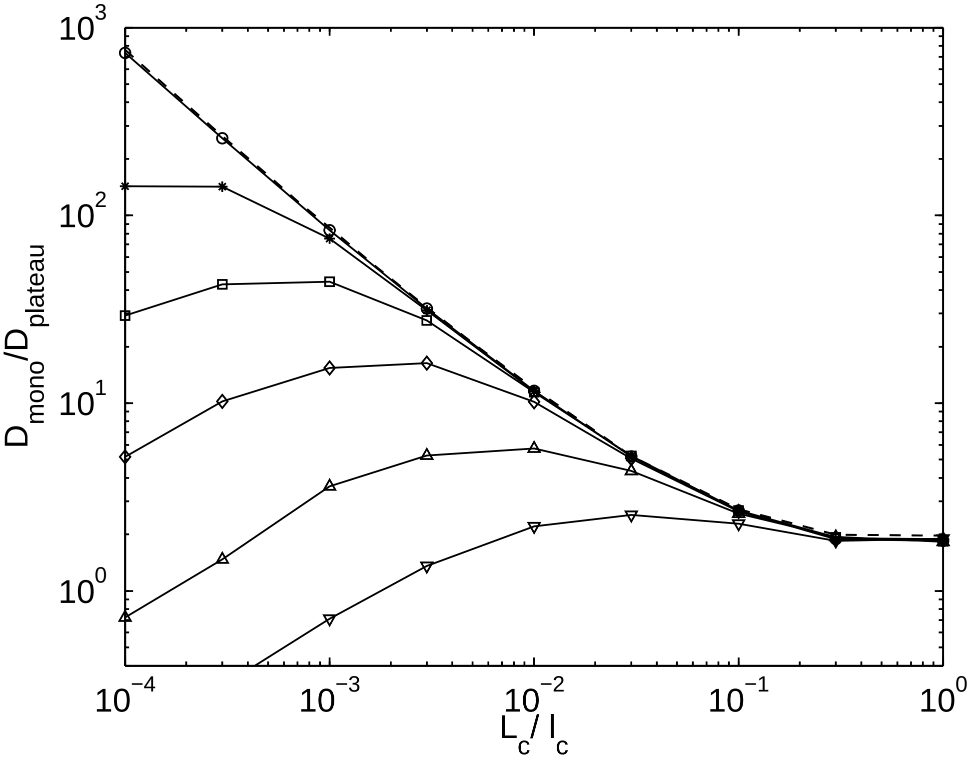

Figure 7.15: Normalized mono-energetic diffusion coefficient $D_{\mathrm{mono}}/D_{\mathrm{plateau}}$ for TJ-II vs. collisionality parameter L_c/l_c at half plasma radius computed by NEO-MC (solid lines) and NEO-2 (dashed line) for $E_r/(vB) = 0$ (circles), $3 \cdot 10^{-5}$ (stars), $1 \cdot 10^{-4}$ (squares), $3 \cdot 10^{-4}$ (diamonds), $1 \cdot 10^{-3}$ (upwards triangles), $3 \cdot 10^{-3}$ (downwards triangles).

7.4.2 Bootstrap coefficient

The following figures show results of computations of normalized mono-energetic bootstrap current coefficients at half plasma radius for the configurations listed in section 7.3 for confinement regimes with various values of the collisionality parameter and the electric field parameter.

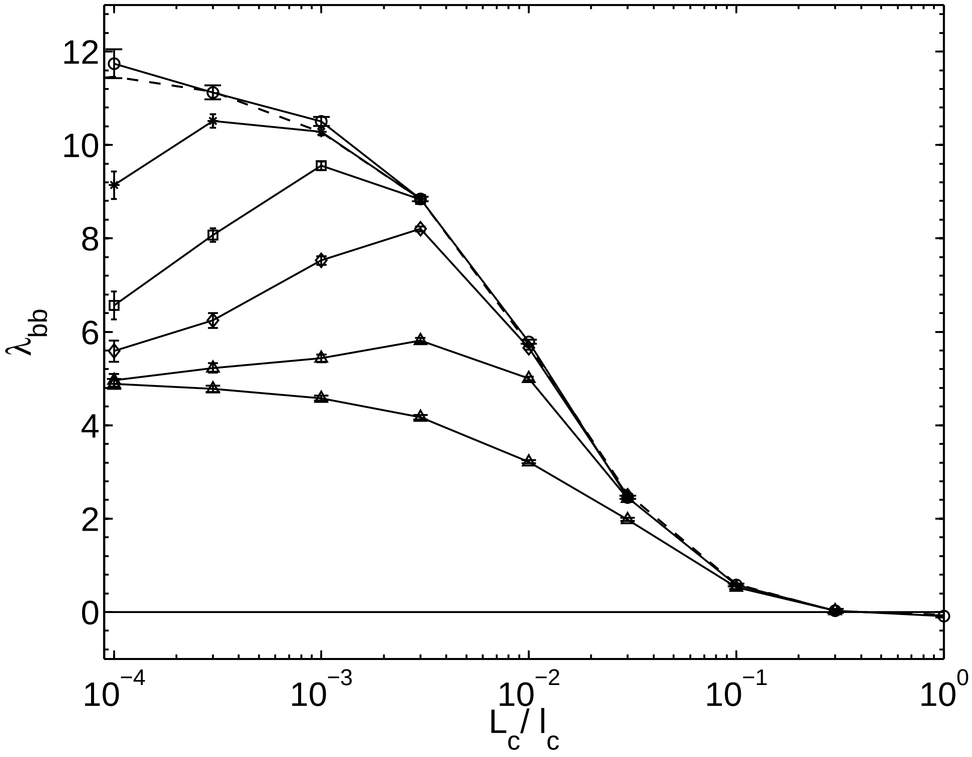

Figure 7.16: Normalized mono-energetic bootstrap coefficient λ_{bb} for LHD with R=375cm vs. collisionality parameter L_c/l_c at half plasma radius computed by NEO-MC (solid lines) and NEO-2 (dashed line) for $E_r/(vB) = 0$ (circles), $3 \cdot 10^{-5}$ (stars), $1 \cdot 10^{-4}$ (squares), $3 \cdot 10^{-4}$ (diamonds), $1 \cdot 10^{-3}$ (upper curve with triangles), $3 \cdot 10^{-3}$ (lower curve with triangles).

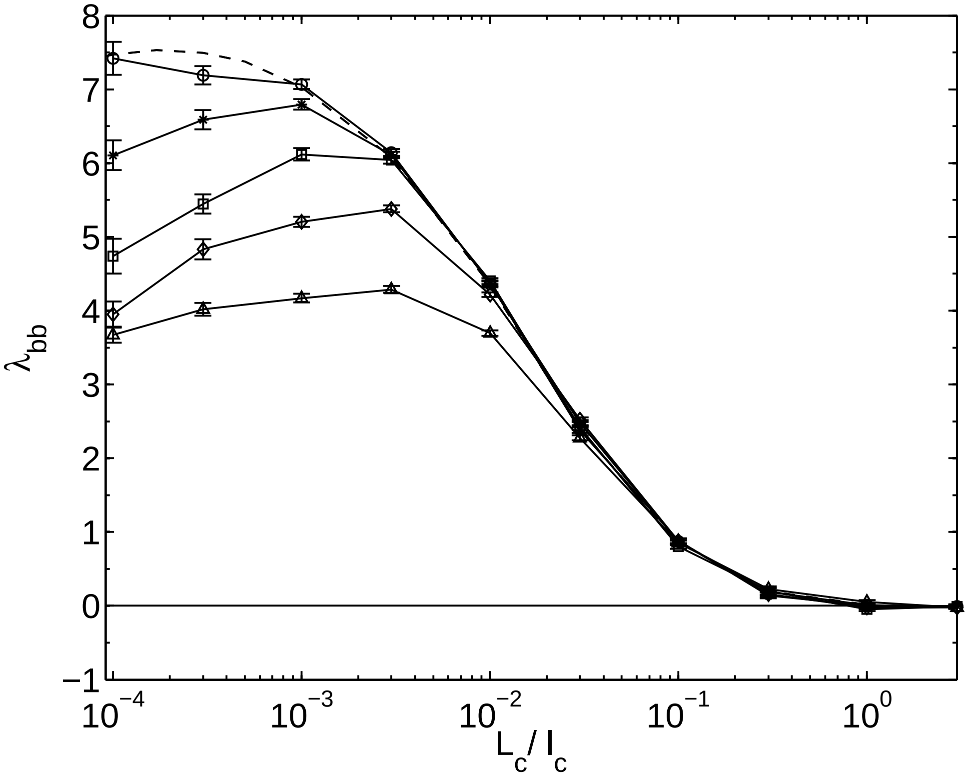

Figure 7.17: Normalized mono-energetic bootstrap coefficient λ_{bb} for LHD with R=360cm vs. collisionality parameter L_c/l_c at half plasma radius computed by NEO-MC (solid lines) and NEO-2 (dashed line) for $E_r/(vB) = 0$ (circles), $3 \cdot 10^{-5}$ (stars), $1 \cdot 10^{-4}$ (squares), $3 \cdot 10^{-4}$ (diamonds), $1 \cdot 10^{-3}$ (triangles).

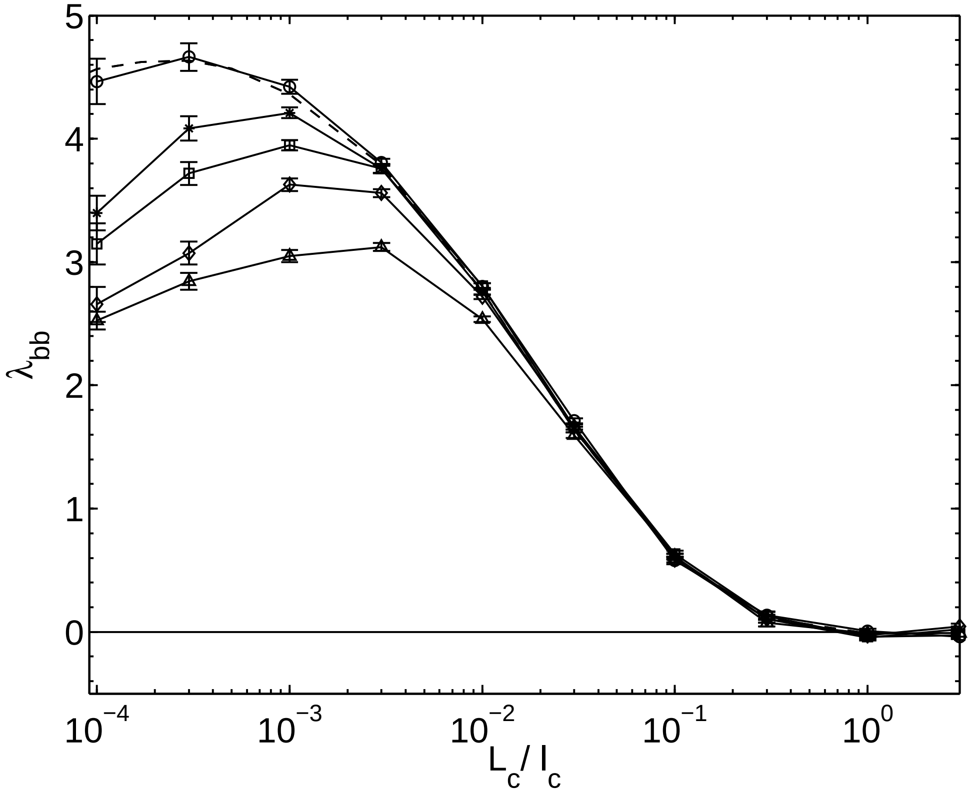

Figure 7.18: Normalized mono-energetic bootstrap coefficient λ_{bb} for LHD with R=353cm vs. collisionality parameter L_c/l_c at half plasma radius computed by NEO-MC (solid lines) and NEO-2 (dashed line) for $E_r/(vB) = 0$ (circles), $3 \cdot 10^{-5}$ (stars), $1 \cdot 10^{-4}$ (squares), $3 \cdot 10^{-4}$ (diamonds), $1 \cdot 10^{-3}$ (triangles).

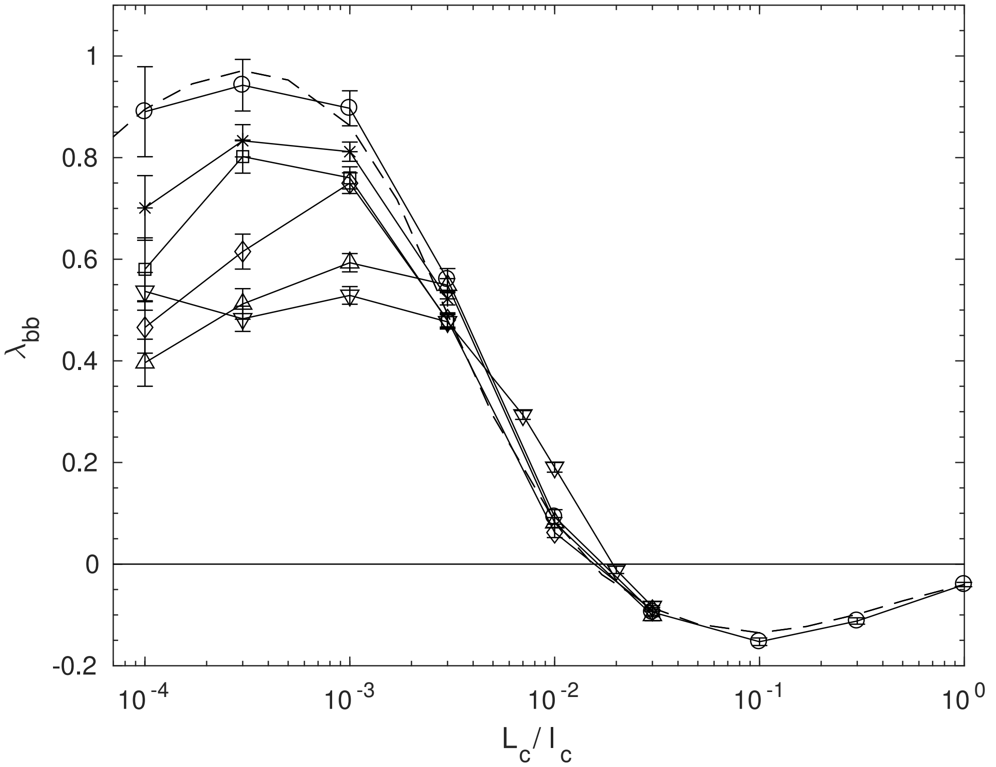

Figure 7.19: Normalized mono-energetic bootstrap coefficient λ_{bb} for W7-X standard configuration vs. collisionality parameter L_c/l_c at half plasma radius computed by NEO-MC (solid lines) and NEO-2 (dashed line) for $E_r/(vB) = 0$ (circles), $3 \cdot 10^{-5}$ (stars), $1 \cdot 10^{-4}$ (squares), $3 \cdot 10^{-4}$ (diamonds), $1 \cdot 10^{-3}$ (upwards triangles), $3 \cdot 10^{-3}$ (downwards triangles).

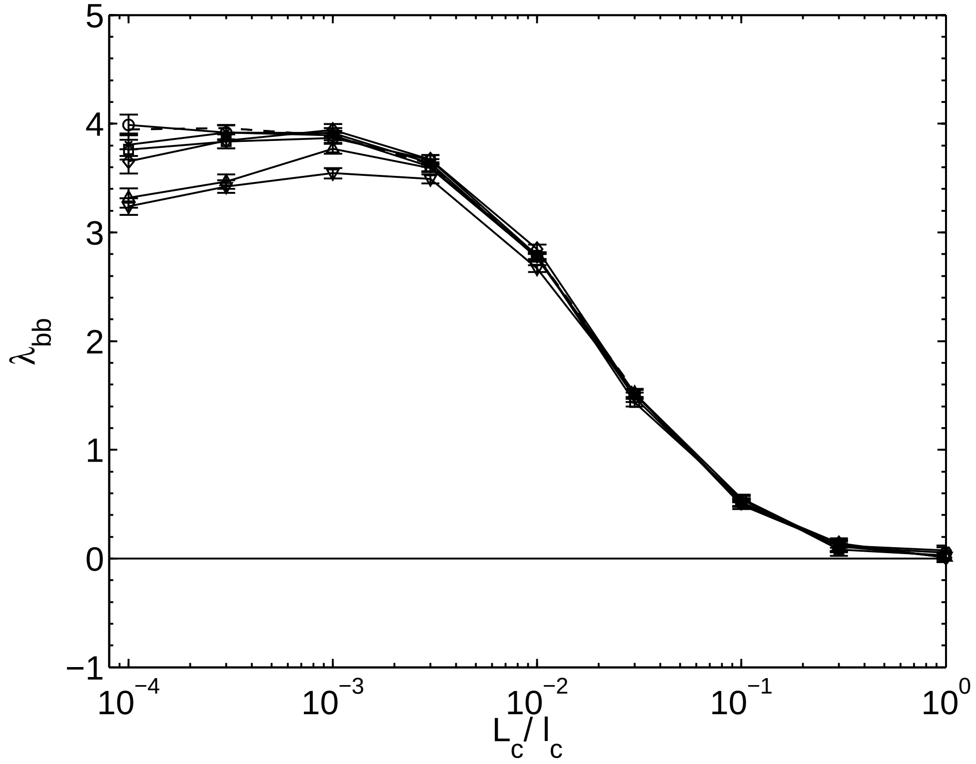

Figure 7.20: Normalized mono-energetic bootstrap coefficient λ_{bb} for NCSX vs. collisionality parameter L_c/l_c at half plasma radius computed by NEO-MC (solid lines) and NEO-2 (dashed line) for $E_r/(vB) = 0$ (circles), $3 \cdot 10^{-5}$ (stars), $1 \cdot 10^{-4}$ (squares), $3 \cdot 10^{-4}$ (diamonds), $1 \cdot 10^{-3}$ (upwards triangles), $3 \cdot 10^{-3}$ (downwards triangles).

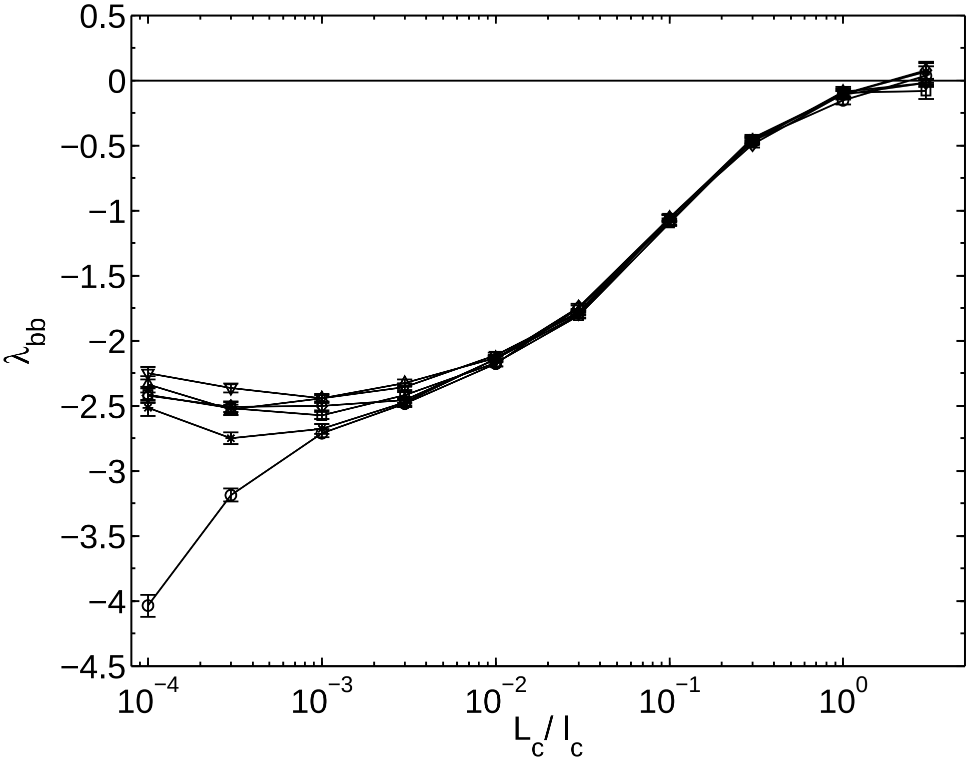

Figure 7.21: Normalized mono-energetic bootstrap coefficient λ_{bb} for HSX vs. collisionality parameter L_c/l_c at half plasma radius computed by NEO-MC (solid lines) and NEO-2 (dashed line) for $E_r/(vB) = 0$ (circles), $3 \cdot 10^{-5}$ (stars), $1 \cdot 10^{-4}$ (squares), $3 \cdot 10^{-4}$ (diamonds), $1 \cdot 10^{-3}$ (upwards triangles), $3 \cdot 10^{-3}$ (downwards triangles).

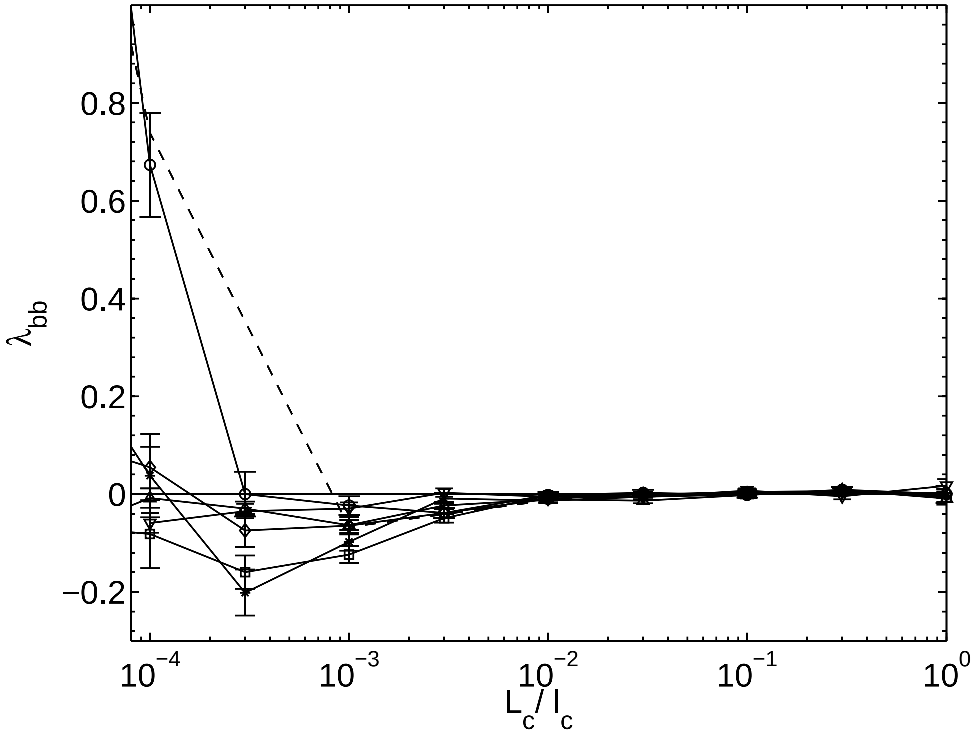

Figure 7.22: Normalized mono-energetic bootstrap coefficient λ_{bb} for QIPC vs. collisionality parameter L_c/l_c at half plasma radius computed by NEO-MC (solid lines) and NEO-2 (dashed line) for $E_r/(vB) = 0$ (circles), $3 \cdot 10^{-5}$ (stars), $1 \cdot 10^{-4}$ (squares), $3 \cdot 10^{-4}$ (diamonds), $1 \cdot 10^{-3}$ (upwards triangles), $3 \cdot 10^{-3}$ (downwards triangles).

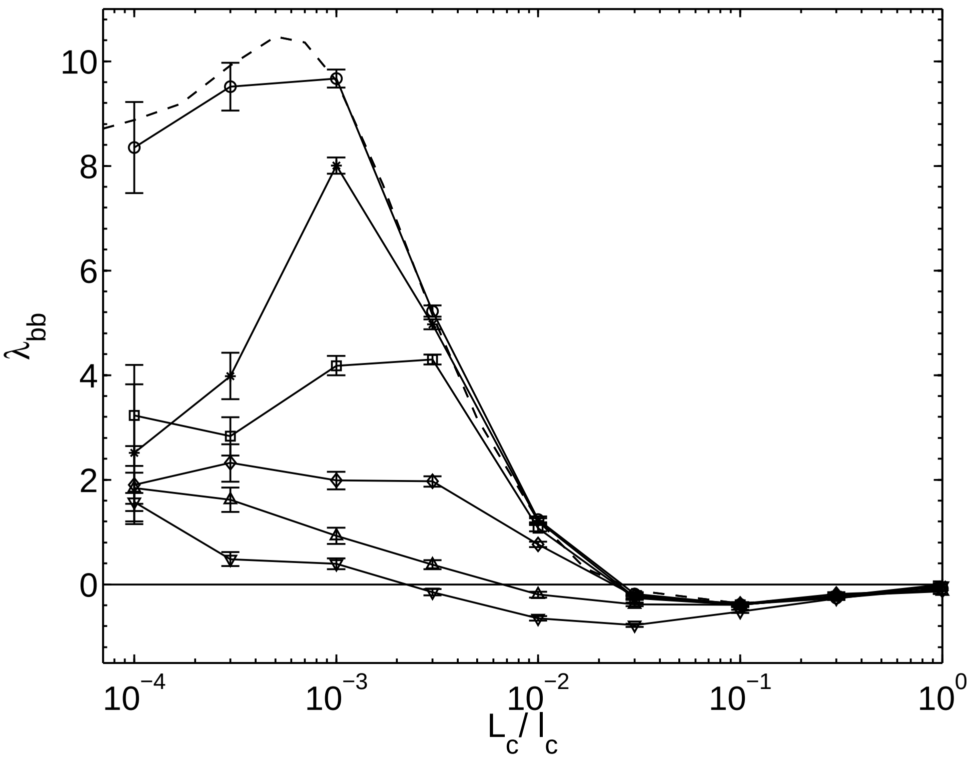

Figure 7.23: Normalized mono-energetic bootstrap coefficient λ_{bb} for TJ-II vs. collisionality parameter L_c/l_c at half plasma radius computed by NEO-MC (solid lines) and NEO-2 (dashed line) for $E_r/(vB) = 0$ (circles), $3 \cdot 10^{-5}$ (stars), $1 \cdot 10^{-4}$ (squares), $3 \cdot 10^{-4}$ (diamonds), $1 \cdot 10^{-3}$ (upwards triangles), $3 \cdot 10^{-3}$ (downwards triangles).

7.4.3 Conductivity coefficient

The following figures show results of computations of normalized mono-energetic parallel conductivity coefficients at half plasma radius for the configurations listed in section 7.3 for confinement regimes with various values of the collisionality parameter and the electric field parameter.

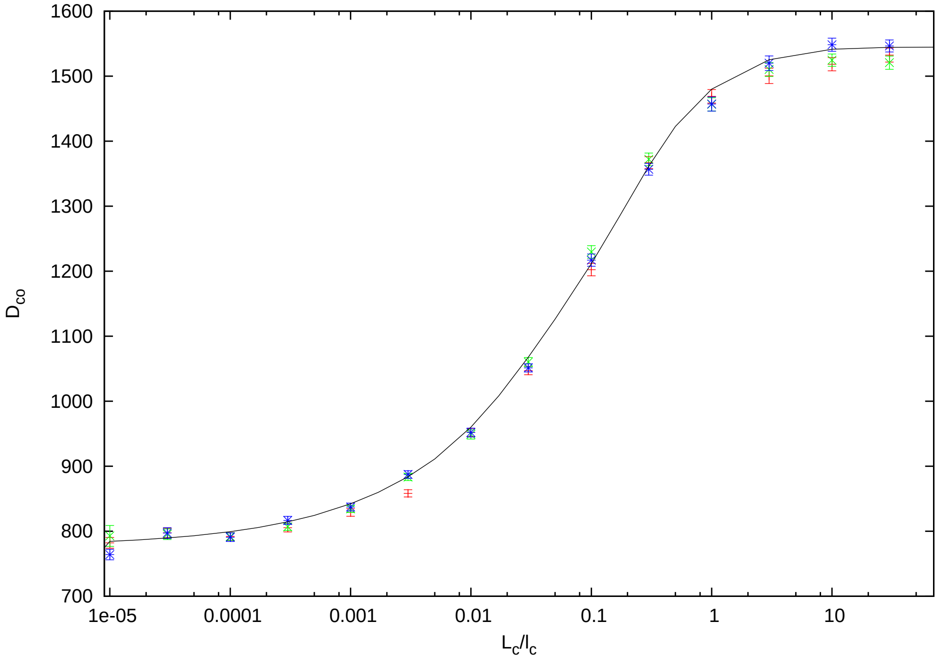

Figure 7.24: Normalized mono-energetic parallel conductivity coefficient D_{co} for LHD with R=375cm vs. collisionality parameter L_c/l_c at half plasma radius computed by NEO-2 (line) and NEO-MC (points) for $E_r/(vB) = 0$ (red), $1 \cdot 10^{-4}$ (green), $1 \cdot 10^{-3}$ (blue).

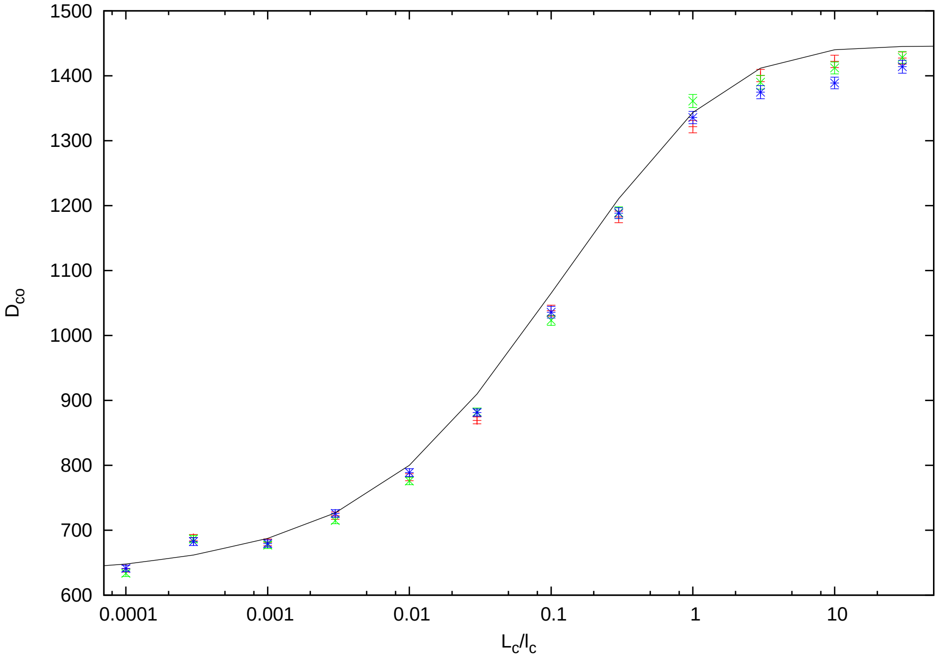

Figure 7.25: Normalized mono-energetic parallel conductivity coefficient D_{co} for LHD with R=360cm vs. collisionality parameter L_c/l_c at half plasma radius computed by NEO-MC (points) for $E_r/(vB) = 0$ (red), $1 \cdot 10^{-4}$ (green), $1 \cdot 10^{-3}$ (blue).

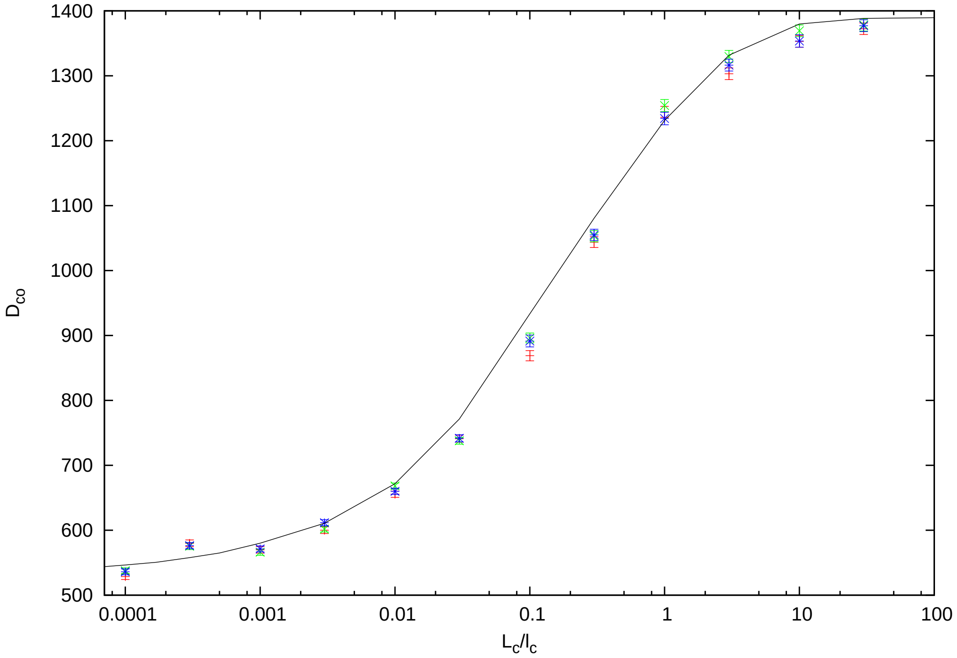

Figure 7.26: Normalized mono-energetic parallel conductivity coefficient D_{co} for LHD with R=353cm vs. collisionality parameter L_c/l_c at half plasma radius computed by NEO-MC (points) for $E_r/(vB) = 0$ (red), $1 \cdot 10^{-4}$ (green), $1 \cdot 10^{-3}$ (blue).

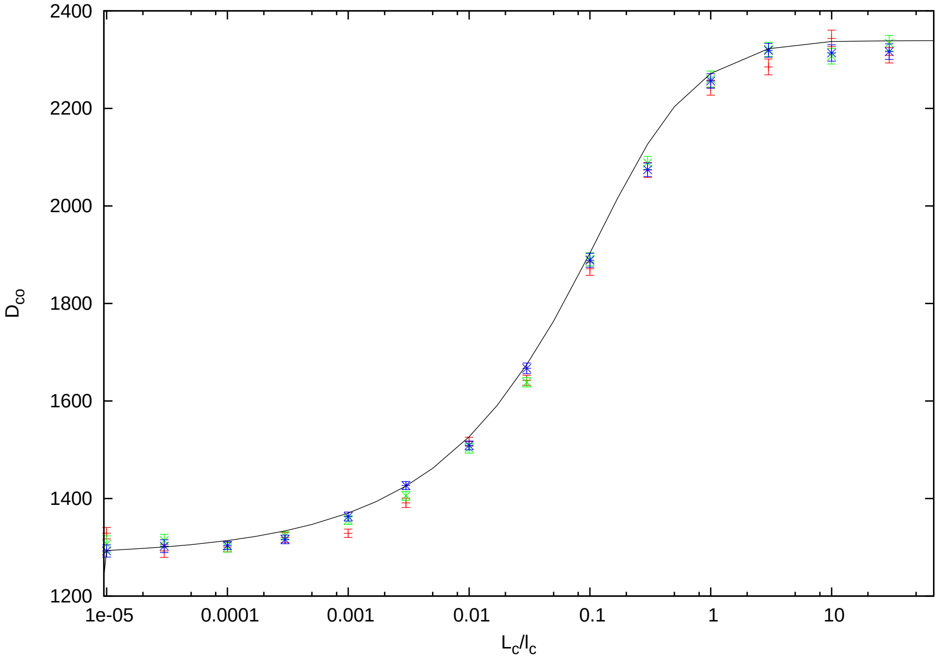

Figure 7.27: Normalized mono-energetic parallel conductivity coefficient D_{co} for W7-X standard configuration vs. collisionality parameter L_c/l_c at half plasma radius computed by NEO-MC (solid lines) and NEO-2 (dashed line) for $E_r/(vB) = 0$ (red), $1 \cdot 10^{-4}$ (green), $1 \cdot 10^{-3}$ (blue).

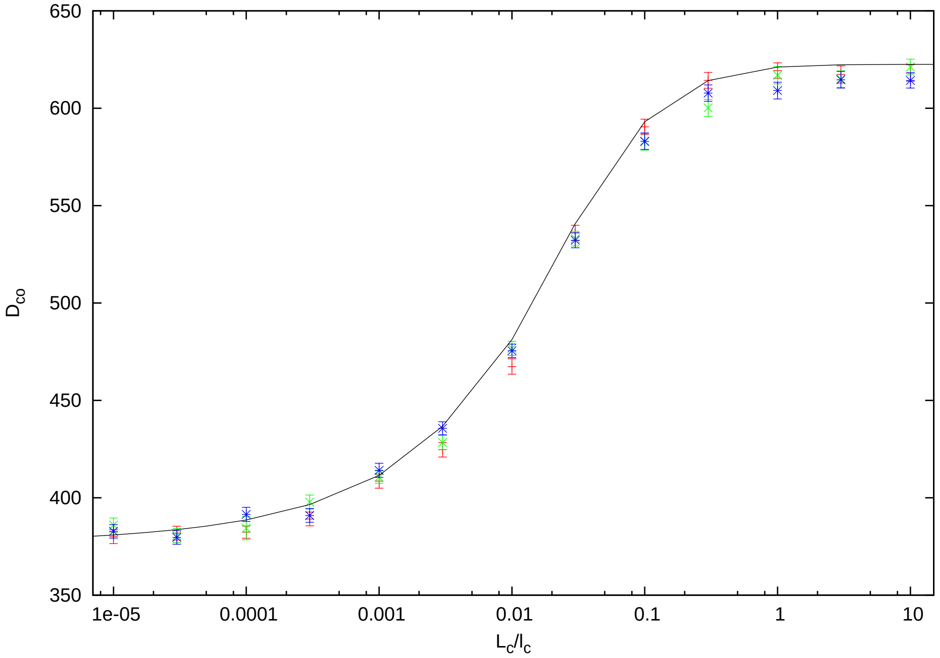

Figure 7.28: Normalized mono-energetic parallel conductivity coefficient D_{co} for NCSX vs. collisionality parameter L_c/l_c at half plasma radius computed by NEO-2 (line) and NEO-MC (points) for $E_r/(vB) = 0$ (red), $1 \cdot 10^{-4}$ (green), $1 \cdot 10^{-3}$ (blue).

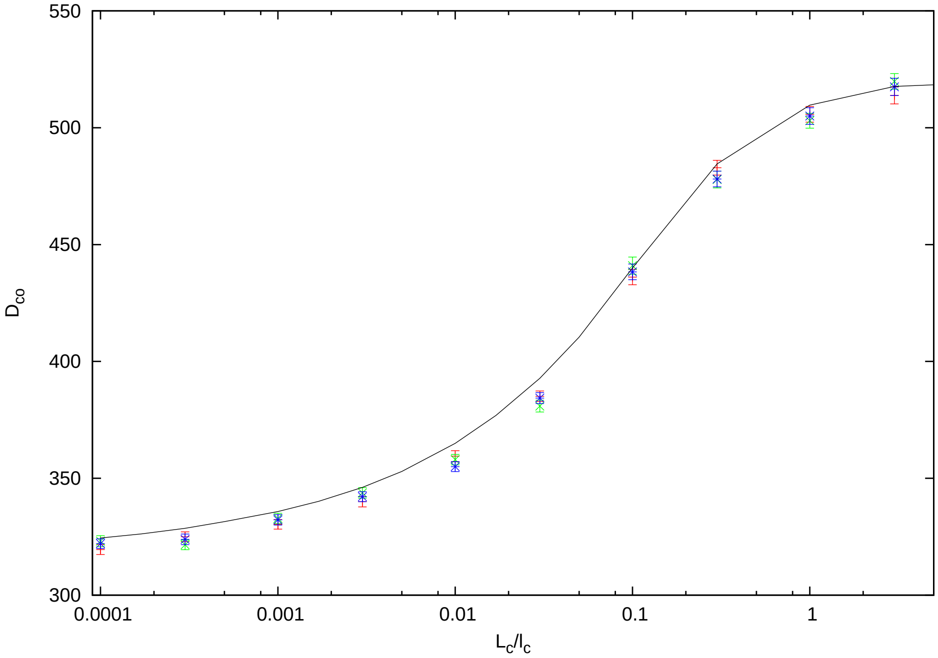

Figure 7.29: Normalized mono-energetic parallel conductivity coefficient D_{co} for HSX vs. collisionality parameter L_c/l_c at half plasma radius computed by NEO-MC (points) for $E_r/(vB) = 0$ (red), $1 \cdot 10^{-4}$ (green), $1 \cdot 10^{-3}$ (blue).

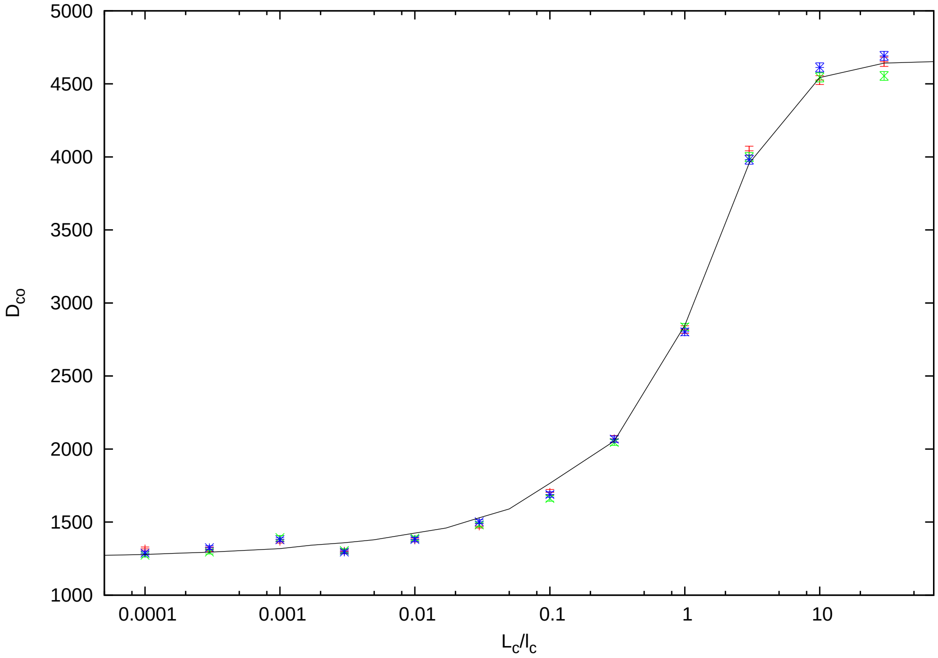

Figure 7.30: Normalized mono-energetic parallel conductivity coefficient D_{co} for QIPC vs. collisionality parameter L_c/l_c at half plasma radius computed by NEO-MC (points) for $E_r/(vB) = 0$ (red), $1 \cdot 10^{-4}$ (green), $1 \cdot 10^{-3}$ (blue).

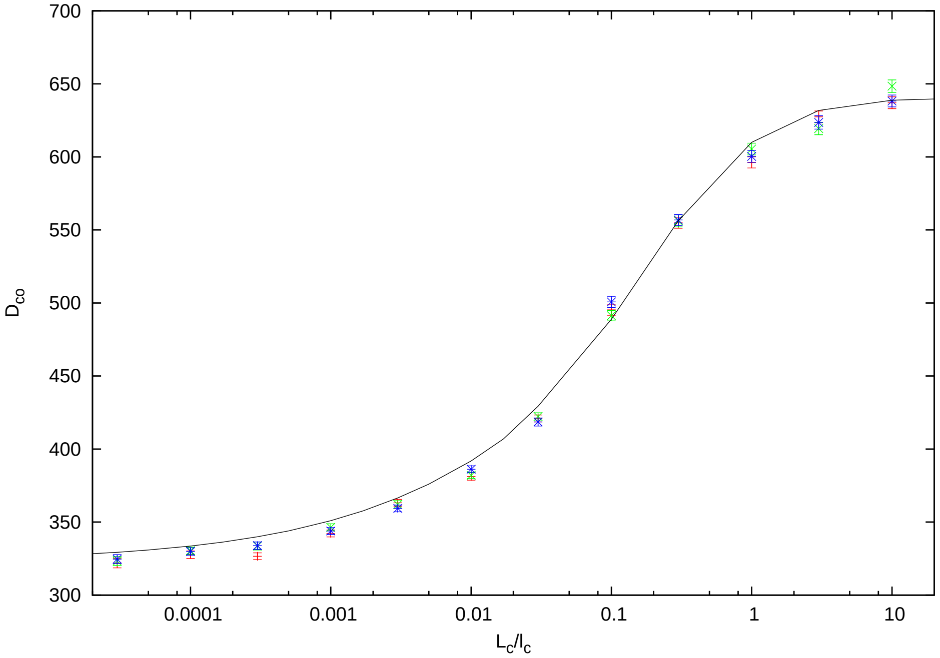

Figure 7.31: Normalized mono-energetic parallel conductivity coefficient D_{co} for TJ-II standard configuration vs. collisionality parameter L_c/l_c at half plasma radius computed by NEO-2 (line) and NEO-MC (points) for $E_r/(vB) = 0$ (red), $1 \cdot 10^{-4}$ (green), $1 \cdot 10^{-3}$ (blue).

Chapter 8

Conclusion

In this work, a specific δf Monte Carlo method for the computation of mono-energetic neoclassical transport coefficients in stellarators has been developed. One of these quantities, the bootstrap current, is of special interest because it can strongly influence the confinement properties of a stellarator. Transport coefficients associated to the bootstrap current are determined by small regions in phase space. Conventional methods usually don't identify this regions and apply an overall treatment which causes huge statistical errors in the computational results. The method developed in this work, NEO-MC, outperforms existing methods by weighting different phase space regions appropriately and by a sophisticated modeling of the physical processes in the trapped-passing boundary. In order to do so a re-discretization procedure and an importance sampling algorithm are employed. The method allows for highly efficient computations of plasma transport coefficients in confinement regimes which have hardly or not at all been accessible with existing methods. NEO-MC can be run on batch systems (e.g. Condor) as well as on parallel clusters (e.g. MPI). The computing time required for a given accuracy of the bootstrap coefficient scales as a mean free path in power of 3/2. The bias introduced by this method can be limited to very low values with small cost in terms of computing time. The method allows for simultaneous computations of the bootstrap coefficient and the diffusion coefficient. Also, the parallel conductivity coefficient can be computed. These three mono-energetic transport coefficients allow for a complete neoclassical description of stellarator plasmas. The results of computations for various stellarators and confinement regimes have been benchmarked with computations by other methods and stay in good agreement with these calculations and new results have been obtained for various stellarator configurations such as LHD, W7-X, NCSX, HSX, QIPC and TJ-II. At the research center CIEMAT in Spain the code NEO-MC is employed for the creation of a neoclassical database.

Appendices

Appendix A

Drift velocity

The equations of drift particle motion in stationary electric and magnetic fields are given by [2]

$$
\begin{aligned}
\frac{\mathrm{d}}{\mathrm{d}t}x^i &= \frac{\mathrm{d}}{\mathrm{d}t}z^i = V_g^i, && \text{(A.1)}\\
\frac{\mathrm{d}}{\mathrm{d}t}p &= \frac{\mathrm{d}}{\mathrm{d}t}z^4 = -em_0\frac{\gamma}{p}V_g^i\frac{\partial\Phi}{\partial x^i}, && \text{(A.2)}\\
\frac{\mathrm{d}}{\mathrm{d}t}\lambda &= \frac{\mathrm{d}}{\mathrm{d}t}z^5 = -\frac{1-\lambda^2}{\lambda}\left(em_0\frac{\gamma}{p^2}V_g^i\frac{\partial\Phi}{\partial x^i}+\frac{1}{2}V_g^i\frac{\partial\ln B}{\partial x^i}\right), && \text{(A.3)}\\
\frac{\mathrm{d}}{\mathrm{d}t}t &= \frac{\mathrm{d}}{\mathrm{d}t}z^6 = 1, && \text{(A.4)}
\end{aligned}
$$

where $i = 1\ldots 3$ and the variables $\mathbf{z}$ include the guiding center coordinates in a general curvilinear coordinate system, $z^i = x^i$, and the momentum space variables $z^4 = |\mathbf{p}|$ and $z^5 = \lambda = p_\parallel/|\mathbf{p}|$ which are the momentum modulus and pitch parameter, respectively, and $z^6 = t$ is the time. The contravariant components of the guiding center drift velocity V_g^i in coordinate-momentum-time space (phase-time space) are given by [114,115]

$$
V_g^i = \frac{1}{B_\parallel^*}\left(v_\parallel B^{*i} + \varepsilon^{ijk}\frac{cB_j}{B\sqrt{g}}\left(\frac{\partial\Phi}{\partial x^k}+\frac{\mu}{e\gamma}\frac{\partial B}{\partial x^k}\right)\right), \qquad \text{(A.5)}
$$

where

$$B_\parallel^*(\mathbf{z}) = n_i B^{*i}, \tag{A.6}$$

$$B^{*i} = B^i + \frac{c}{e}\frac{p\lambda}{\sqrt{g}}\varepsilon^{ijk}\frac{\partial n_k}{\partial x^j}. \tag{A.7}$$

Here, e is the particle charge, c denotes the speed of light, $\sqrt{g}$ is the metric determinant of the spatial coordinate system $\mathbf{x}$, Φ is the electrostatic potential, B^i are the contravariant components of the magnetic field, n_i are the covariant components of the unit vector along the magnetic field $\mathbf{n} = \mathbf{B}/B$ and ε^{ijk} is the completely anti-symmetric unit tensor (Levi-Civita symbol). The relativistic factor γ, the cyclotron frequency ω_c, the parallel velocity $v_\parallel$ and the magnetic moment μ are given by

$$\gamma = \sqrt{1 + \frac{p^2}{m_0^2 c^2}}, \tag{A.8}$$

$$\omega_c = \frac{eB}{m_0 c\gamma}, \tag{A.9}$$

$$v_\parallel = \frac{\lambda p}{m_0\gamma}, \tag{A.10}$$

$$\mu = \frac{p^2(1-\lambda^2)}{2m_0 B}, \tag{A.11}$$

where m_0 is the mass of a particle at rest and $v_\parallel$ as well as μ are expressed through p and λ according to equations (A.10) and (A.11), respectively. Using

$$\frac{1}{B_\parallel^*} \approx \frac{1}{B}\left(1 - \frac{B_\parallel^* - B}{B}\right), \tag{A.12}$$

equation (A.5) can be expanded up to the linear order in Larmor radius

$$V_g^i = \frac{1}{B}\left[v_\parallel B^{*i} - v_\parallel B^i \frac{B_\parallel^* - B}{B} + \varepsilon^{ijk}\frac{cB_j}{B\sqrt{g}}\left(\frac{\partial\Phi}{\partial x^k} + \frac{\mu}{e\gamma}\frac{\partial B}{\partial x^k}\right)\right], \tag{A.13}$$

which is in vector form

$$\mathbf{V}_g = \frac{1}{B}\left[v_\parallel \mathbf{B}^* - v_\parallel \mathbf{B}\frac{B_\parallel^* - B}{B} + \frac{c}{B}\mathbf{B}\times\left(\nabla\Phi + \frac{\mu}{e\gamma}\nabla B\right)\right], \tag{A.14}$$

where

$$B^*_\parallel = \mathbf{n}\cdot\mathbf{B}^* = B[1+\rho_\parallel\,\mathbf{n}\cdot(\nabla\times\mathbf{n})]\,, \tag{A.15}$$

and

$$\mathbf{B}^* = \mathbf{B} + \rho_\parallel B\;\nabla\times\mathbf{n}\,, \tag{A.16}$$

with $\mathbf{n} = \mathbf{B}/B$ and

$$\rho_\parallel = \frac{mcv_\parallel}{eB}\,. \tag{A.17}$$

Equation (A.14) is equivalent to the form of the the guiding center drift velocity given by [115, 116]

$$\mathbf{V}_g = v_\parallel\frac{\mathbf{B}}{B} + \frac{e\rho_\parallel}{mc}\left(\nabla\times(\rho_\parallel\mathbf{B}) - \frac{\mathbf{B}\left[\mathbf{B}\cdot\nabla\times(\rho_\parallel\mathbf{B})\right]}{B^2}\right)\,. \tag{A.18}$$

Multiplying equation (A.18) with $\nabla\psi$ and taking into account that $\mathbf{B}\cdot\nabla\psi = 0$ yields

$$\dot{\psi} = \mathbf{V}_g\cdot\nabla\psi = \frac{v_\parallel}{\omega_c}\left(\nabla\times v_\parallel\frac{\mathbf{B}}{B}\right)\cdot\nabla\psi\,, \tag{A.19}$$

where $\omega_c = eB/(mc)$ is the cyclotron frequency. Using the vector identity $\nabla\times(a\mathbf{A}) = a\nabla\times\mathbf{A} - \mathbf{A}\times\nabla a$ equation (A.19) becomes

$$\begin{aligned}
\dot{\psi} &= \frac{v_\parallel}{\omega_c}\nabla\psi\cdot\left[v_\parallel\left(\nabla\times\frac{\mathbf{B}}{B}\right) - \left(\frac{\mathbf{B}}{B}\times\nabla v_\parallel\right)\right] && \text{(A.20)}\\
&= \frac{v_\parallel}{\omega_c}\nabla\psi\cdot\left[v_\parallel\frac{1}{B}(\nabla\times\mathbf{B}) + v_\parallel\left(\mathbf{B}\times\frac{1}{B^2}\nabla B\right)\right. && \text{(A.21)}\\
&- \left.\left(\frac{\mathbf{B}}{B}\times\nabla v_\parallel\right)\right]\,. && \text{(A.22)}
\end{aligned}$$

The first term vanishes because the current $\mathbf{j}$

$$\nabla\times\mathbf{B} = \frac{4\pi}{c}\mathbf{j} \tag{A.23}$$

is perpendicular to $\nabla\psi$. The gradient of the parallel velocity $v_\parallel$

$$v_\parallel = \sigma\sqrt{v^2 - J_\perp B} \tag{A.24}$$

is given by

$$\nabla v_\parallel = -\frac{J_\perp}{2v_\parallel}\nabla B = -\frac{v_\perp^2}{2v_\parallel B}\nabla B\,, \tag{A.25}$$

therefore equation (A.22) can be expressed as

$$\begin{aligned}\dot\psi &= \frac{v_\parallel}{\omega_c}\nabla\psi\cdot\left[\frac{v_\parallel}{B^2}\left(\mathbf{B}\times\nabla B\right)+\frac{v_\perp^2}{2v_\parallel B^2}\left(\mathbf{B}\times\nabla B\right)\right] &\text{(A.26)}\\ &= \frac{1}{2\omega_c}(v_\parallel^2+v^2)\frac{1}{B^2}(\mathbf{B}\times\nabla B)\cdot\nabla\psi\,. &\text{(A.27)}\end{aligned}$$

Introducing the geodesic curvature k_G of the magnetic field line and $\mathbf{n}_\psi = \nabla\psi/|\nabla\psi|$

$$\begin{aligned}k_G &= \mathbf{n}_\psi\cdot(\mathbf{n}\times(\mathbf{n}\cdot\nabla)\mathbf{n}) &\text{(A.28)}\\ &= \frac{\nabla\psi}{|\nabla\psi|}\frac{1}{B^2}\left[\mathbf{B}\times(\mathbf{B}\cdot\nabla)\frac{\mathbf{B}}{B}\right] &\text{(A.29)}\\ &= \frac{\nabla\psi}{|\nabla\psi|}\frac{1}{B^2}\left\{\mathbf{B}\times\left[\frac{1}{B}\ (\mathbf{B}\cdot\nabla)\mathbf{B}\ +\mathbf{B}(\mathbf{B}\cdot\nabla)\frac{1}{B}\right]\right\} &\text{(A.30)}\\ &= \frac{\nabla\psi}{|\nabla\psi|}\frac{1}{B^2}(\mathbf{B}\times\nabla B)\,, &\text{(A.31)}\end{aligned}$$

the contravariant ψ-component of the guiding center drift velocity (A.27) can be represented as (see also [117, 118])

$$\dot\psi = \frac{1}{2\omega_c}(v^2+v_\parallel^2)k_G|\nabla\psi|\,. \tag{A.32}$$

Appendix B

Solution to the integral equation

An integral equation is given by (see equation (5.15)

$$F(\mathbf{z}) = \mathcal{K}\, F(\mathbf{z}) + Q(\mathbf{z})\,. \tag{B.1}$$

One can check by substitution that $F(\mathbf{z})$ can be expressed as an infinite sum

$$F(\mathbf{z}) = \sum_{k=0}^{\infty} \mathcal{K}^k\, Q(\mathbf{z})\,, \tag{B.2}$$

and $F(\mathbf{z})$ can be presented as

$$\begin{aligned} F(\mathbf{z}) &= \mathcal{K}\,[\mathcal{K}\, F(\mathbf{z}) + Q(\mathbf{z})] + Q(\mathbf{z}) && \text{(B.3)}\\ &= \mathcal{K}^2\, F(\mathbf{z}) + \mathcal{K}\, Q(\mathbf{z}) + Q(\mathbf{z}) && \text{(B.4)}\\ &= \mathcal{K}^3\, F(\mathbf{z}) + \mathcal{K}^2\, Q(\mathbf{z}) + \mathcal{K}\, Q(\mathbf{z}) + Q(\mathbf{z}) && \text{(B.5)}\\ &= \ldots\ldots && \text{(B.6)}\\ &= \mathcal{K}^M F(\mathbf{z}) + \sum_{k=0}^{M-1} \mathcal{K}^k\, Q(\mathbf{z})\,. && \text{(B.7)} \end{aligned}$$

Introducing the notation $\mathcal{K}^M = \mathcal{K}_{(M)}$ and

$$q_{(M)}(\mathbf{z}) \;=\; \sum_{k=0}^{M-1} \mathcal{K}^k\, Q(\mathbf{z})\,, \tag{B.8}$$

one gets from (B.7), (B.1) and (B.2)

$$\begin{aligned} F(\mathbf{z}) &= \sum_{k=0}^{\infty} \mathcal{K}_{(M)}^{k}\, q_{(M)}(\mathbf{z}) && \text{(B.9)} \\ &= \sum_{k=0}^{\infty} \mathcal{K}^{M\cdot k}\, q_{(M)}(\mathbf{z})\,. && \text{(B.10)} \end{aligned}$$

Arithmetic averaging of $F(\mathbf{z})$ given by (B.7)

$$\begin{aligned} F(\mathbf{z}) &= \mathcal{K}_{(1)}\, F(\mathbf{z}) + q_{(1)}(\mathbf{z}) && \text{(B.11)} \\ &= \mathcal{K}_{(2)}\, F(\mathbf{z}) + q_{(2)}(\mathbf{z}) && \text{(B.12)} \\ &= \ldots\ldots && \text{(B.13)} \\ &= \mathcal{K}_{(M)}\, F(\mathbf{z}) + q_{(M)}(\mathbf{z})\,, && \text{(B.14)} \end{aligned}$$

one finds

$$F(\mathbf{z}) = \frac{1}{M} \sum_{j=1}^{M} \mathcal{K}_{(j)}\, F(\mathbf{z}) + \mathcal{Q}_M(\mathbf{z})\,, \tag{B.15}$$

where $\mathcal{Q}_M(\mathbf{z})$ is defined as

$$\mathcal{Q}_M(\mathbf{z}) = \frac{1}{M} \sum_{j=1}^{M} q_{(j)}(\mathbf{z})\,. \tag{B.16}$$

Using (B.10) the quantity $F(\mathbf{z})$ can be written as

$$F(\mathbf{z}) = \frac{1}{M} \sum_{j=1}^{M} \sum_{k=0}^{\infty} \mathcal{K}^{j+M\cdot k}\, q_{(M)}(\mathbf{z}) + \mathcal{Q}_M(\mathbf{z})\,. \tag{B.17}$$

The summation in (B.17) can be simplified according to

$$\begin{aligned} F(\mathbf{z}) &= \frac{1}{M} \sum_{l=1}^{\infty} \mathcal{K}^{l}\, q_{(M)}(\mathbf{z}) + \mathcal{Q}_M(\mathbf{z}) && \text{(B.18)} \\ &= \frac{1}{M} \sum_{l=0}^{\infty} \mathcal{K}^{l}\, q_{(M)}(\mathbf{z}) + \Delta F_M(\mathbf{z})\,, && \text{(B.19)} \end{aligned}$$

where

$$\Delta F_M(\mathbf{z}) = \mathcal{Q}_M(\mathbf{z}) - \frac{q_{(M)}(\mathbf{z})}{M}\,. \tag{B.20}$$

Using (B.16) and (B.8) one gets

$$\begin{aligned}\Delta F_M(\mathbf{z}) &= \frac{1}{M}\left(\sum_{j=1}^{M} q_{(j)}(\mathbf{z}) - q_{(M)}(\mathbf{z})\right) && \text{(B.21)}\\ &= \frac{1}{M}\sum_{j=1}^{M-1} q_{(j)}(\mathbf{z}) && \text{(B.22)}\\ &= \frac{1}{M}\sum_{j=1}^{M-1}\sum_{k=0}^{j-1}\mathcal{K}^k\, Q(\mathbf{z})\,. && \text{(B.23)}\end{aligned}$$

The summation in (B.23) can be rewritten according to

$$\sum_{j=1}^{M-1}\sum_{k=0}^{j-1} = \sum_{k=0}^{M-2}\sum_{j=k+1}^{M-1}\,, \qquad \text{(B.24)}$$

and the quantity $\Delta F_M(\mathbf{z})$ can be written as

$$\begin{aligned}\Delta F_M(\mathbf{z}) &= \frac{1}{M}\sum_{k=0}^{M-2}\mathcal{K}^k\sum_{j=k+1}^{M-1} Q(\mathbf{z}) && \text{(B.25)}\\ &= \sum_{k=0}^{M-2}\left(1-\frac{k+1}{M}\right)\mathcal{K}^k Q(\mathbf{z}) && \text{(B.26)}\\ &= \sum_{k=0}^{M-1}\left(1-\frac{k+1}{M}\right)\mathcal{K}^k Q(\mathbf{z})\,. && \text{(B.27)}\end{aligned}$$

Using equation (B.8) and introducing $Q_M(\mathbf{z})$ according to

$$Q_M(\mathbf{z}) = \frac{1}{M} q_{(M)}(\mathbf{z}) = \frac{1}{M}\sum_{k=0}^{M-1}\mathcal{K}^k\, Q(\mathbf{z})\,, \qquad \text{(B.28)}$$

it follows from (B.19)

$$F(\mathbf{z}) = \sum_{l=0}^{\infty}\mathcal{K}^l Q_M(\mathbf{z}) + \Delta F_M(\mathbf{z})\,. \qquad \text{(B.29)}$$

The first term in this equation can be defined as

$$F_M(\mathbf{z}) = \sum_{l=0}^{\infty} \mathcal{K}^l Q_M(\mathbf{z}) \,, \tag{B.30}$$

and is a series solution to

$$F_M(\mathbf{z}) = \mathcal{K} F_M(\mathbf{z}) + Q_M(\mathbf{z}) \,. \tag{B.31}$$

Using (B.30), equation (B.29) can be written as

$$F(\mathbf{z}) = F_M(\mathbf{z}) + \Delta F_M(\mathbf{z}) \,. \tag{B.32}$$

Appendix C

Coulomb collision operator

As an outlook, a short overview of the steps necessary to implement a linearized Coulomb collision operator in the procedure is given. The kinetic equation in [1] is given by

$$\mathcal{L}_D \widehat{f} = \dot{\psi} \,, \tag{C.1}$$

where

$$\mathcal{L}_D = \frac{\partial}{\partial t} + \mathbf{V}_g \cdot \nabla - \mathcal{L}_C \,, \tag{C.2}$$

and $\mathcal{L}_C$ is a Lorentz operator. For the full collision operator one has to replace

$$\mathcal{L}_C \to \mathcal{L}_{CD} + \mathcal{L}_{CI} \,, \tag{C.3}$$

where $\mathcal{L}_{CD}$ is the diffusion part (scattering by a Maxwellian background), which includes also diffusion over energy. $\mathcal{L}_{CI}$ is the integral part of the collision operator (scattering of the background by test particles). Including the differential part into the dynamic operator

$$\mathcal{L}_D \to \mathcal{L}_D = \frac{\partial}{\partial t} + \mathbf{V}_g \cdot \nabla - \mathcal{L}_{CD} \,, \tag{C.4}$$

the kinetic equation (C.1) becomes

$$\mathcal{L}_D \widehat{f} = \dot{\psi} + \mathcal{L}_{CI} \widehat{f} \,. \tag{C.5}$$

The procedure in [1] in the paper describes the inversion of $\mathcal{L}_D$. Only moments are retained and the function $\widehat{f}$ itself is not computed. However, by scoring weights on the grid one can define

$$\widehat{f} = \mathcal{L}_D^{-1} Q \,, \tag{C.6}$$

where Q is an arbitrary steady ($\partial Q/\partial t = 0$) source ($Q = \dot{\psi}$ in Ref. [1]). Thus one can write an integral equation

$$\widehat{f} = \mathcal{L}_D^{-1} \psi + \mathcal{L}_D^{-1} \mathcal{L}_{CI} \widehat{f} \,, \tag{C.7}$$

where $\mathcal{L}_D^{-1}$ is known. A solution can be obtained by direct iterations

$$\widehat{f} = \sum_{k=0}^{\infty} \widehat{f}_k \tag{C.8}$$

$$\widehat{f}_0 = \mathcal{L}_D^{-1} \psi \tag{C.9}$$

$$\widehat{f}_{k+1} = \mathcal{L}_D^{-1} \mathcal{L}_{CI} \widehat{f}_k \,. \tag{C.10}$$

Thus, the algorithm is like this:

1. Find $\mathcal{L}_D^{-1} \psi$ with the same algorithm as in [1] , but with :
   (a) In addition to Lorentz diffusion, diffusion over energy is considered.
   (b) Re-discretization is done using a 4D grid (energy is an additional dimension).
   (c) The distribution function is also scored, one gets $\widehat{f}_0$.
2. From the known $\widehat{f}_0$ on the grid the new source term

   $$Q_1 = \mathcal{L}_{CI} \widehat{f}_0 \tag{C.11}$$

   on the same 4D grid can be computed (using Laguerre-Legendre expansion).
3. Repeating step 1 with the source Q_1 and one can find

   $$\widehat{f}_1 = \mathcal{L}_D^{-1} Q_1 \tag{C.12}$$

   $$\equiv \mathcal{L}_D^{-1} \mathcal{L}_{CI} \widehat{f}_0 \,, \tag{C.13}$$

   by scoring weights on the grid (as done for $\widehat{f}_0$).

4. Repeating step 2 with $\widehat{f_1}$ instead of $\widehat{f_0}$ one gets

$$Q_2 = \mathcal{L}_{CI}\widehat{f_1}\,. \tag{C.14}$$

5. Repeat step 3 with Q_2 instead of Q_1.
6. Steps 4 and 5 have to be repeated until convergence is reached.

Appendix D

δf method for SMT

The efficiency in computations of neoclassical transport coefficients in stellarators can be further improved by implementing a δf scheme in the Stochastic Mapping Technique [2]. The Stochastic Mapping Technique (SMT) is a highly efficient method to solve the five-dimensional Drift Kinetic Equation in the long-mean-free-path regime. It can be used for any problem where conventional Monte Carlo methods are applied and weighting schemes developed for conventional Monte Carlo methods are fully applicable to SMT. The dimensionality of the problem is reduced to four dimensions through a discretization in one dimension. Instead of tracing test particles in the whole phase space test particles are followed on particular Poincaré cuts. Precomputed maps for the magnetic field and for drift orbits are used to represent the continuous particle motion with a sequence of mappings of particle footprints and Coulomb collisions are modeled with random changes of velocity space variables. The computation time is reduced significantly compared to direct Monte-Carlo methods and the method is applicable to stellarators with arbitrary magnetic field geometries [2]. In this method the drift kinetic equation is represented as

$$V^i \frac{\partial f}{\partial Z^i} = \hat{L}_c f \, , \tag{D.1}$$

where f is the particle distribution function which depends on the coordinate space variables Z^i and on the velocity space variables V^i and $\hat{L}_c$ is a collision operator. The distribution function f is split into a background part f_0 which is taken to be a Maxwellian f_M

$$f_M(\psi, p) = n(\psi) \frac{1}{(2\pi m T(\psi))^{3/2}} \exp\left\{ -\frac{W - e\Phi(\psi)}{T(\psi)} \right\} , \tag{D.2}$$

and a deviation δf from the background. Here p, W, Φ, ψ, e, m, T and n are the particle momentum, total energy, electrostatic potential, flux surface label, elementary charge, mass, temperature and particle density, respectively.

Substituting $f = f_0 + \delta f$ into (D.1), taking into account that the part of the collision operator acting on the Maxwellian vanishes and multiplying the equation with $\delta(\psi - \psi_0)$ gives

$$\begin{aligned} V^i \frac{\partial \delta f\, \delta(\psi - \psi_0)}{\partial Z^i} \quad &- \quad V^i\, \delta f\, \frac{\partial}{\partial Z^i} \delta(\psi - \psi_0) = \\ &= \quad \delta(\psi - \psi_0)\, \hat{L}_c \delta f - V^i \frac{\partial \psi}{\partial Z^i} \frac{\partial f_M}{\partial \psi} \delta(\psi - \psi_0) \,. \end{aligned} \tag{D.3}$$

Introducing the distribution function δf_1 which is defined as

$$\delta f_1 = \delta f\, \delta(\psi - \psi_0) \,, \tag{D.4}$$

one gets

$$V^i \frac{\partial \delta f_1}{\partial Z^i} = \hat{L}_c\, \delta f_1 - V^i \frac{\partial \psi}{\partial Z^i} \frac{\partial f_M}{\partial \psi} \delta(\psi - \psi_0) \,. \tag{D.5}$$

The second term on the left hand side of (D.3) has been neglected, the last term defines a source Q

$$Q = -V^i \frac{\partial \psi}{\partial Z^i} \frac{\partial f_M}{\partial \psi} \delta(\psi - \psi_0) \,. \tag{D.6}$$

The equation for the particle flux perpendicular to the flux surface is given by

$$\begin{aligned} \Gamma_{n\perp} &= \int \mathrm{d}^3 r \int \mathrm{d}^3 p\, \delta f\, \delta(\psi - \psi_0) \mathbf{v}_g \cdot \nabla \psi && \text{(D.7)} \\ &= \int \mathrm{d}^3 r \int \mathrm{d}^3 p\, \delta f_1\, V^i \frac{\partial \psi}{\partial Z^i} && \text{(D.8)} \\ &= 2\pi \sum_{\mathbf{m}} \int \mathrm{d}^4 u\, \Gamma_{\mathbf{m}}(\mathbf{u})\, \overline{V^i \frac{\partial \psi}{\partial Z^i}} \,, && \text{(D.9)} \end{aligned}$$

where the formalism of the Stochastic Mapping Technique [2] has been introduced in the last step. The measure element d^4u is given by $\mathrm{d}u^1\mathrm{d}u^2\mathrm{d}u^3\mathrm{d}u^4 = \mathrm{d}x^1\mathrm{d}x^2\mathrm{d}p\mathrm{d}\lambda$, where x^i, p and λ are spatial coordinates, momentum and pitch angle cosine at Poincaré cuts which are placed at toroidal angles $\varphi = x^3$ where the magnetic field has a minimum along the field line. The cuts are numbered by vector indices $\mathbf{m} = (m, n)$ where m is the index of the field period and n is the index of the cut within the period. The quantity $\Gamma_{\mathbf{m}} = J_{\mathbf{m}} f$ is a pseudo scalar flux density and is related to the distribution function f by the Jacobian (D.13). The bar in equation (D.9) denotes an average over a bounce time $\tau_{b\mathbf{m}}$ which is defined by the time that a particle needs to transit from a cut with the index $\mathbf{m}$ to a cut with the index $\mathbf{m}'$. This can be either the next (previous) cut for a particle running in co (counter) direction or the same cut if the particle is trapped (details are given in the reference above)

$$\overline{V^i \frac{\partial \psi}{\partial Z^i}} = \int\limits_0^{\tau_{b\mathbf{m}}} \mathrm{d}\tau \, V^i \frac{\partial \psi}{\partial Z^i} = \int\limits_0^{\tau_{b\mathbf{m}}} \mathrm{d}\tau \frac{\mathrm{d}\psi}{\mathrm{d}\tau} = \delta\psi_{b\mathbf{m}} \approx \Delta x^i_{\mathbf{m}} \frac{\partial \psi}{\partial x^i} \, . \tag{D.10}$$

With the average (D.10) the source term (D.6) can be written as

$$\bar{Q}_{\mathbf{m}} = -\delta(\psi - \psi_0) \frac{\partial f_M}{\partial \psi} \int\limits_0^{\tau_{b\mathbf{m}}} \mathrm{d}\tau \, V^i \frac{\partial \psi}{\partial Z^i} \tag{D.11}$$

$$= -\delta(\psi - \psi_0) \frac{\partial f_M}{\partial \psi} \, \Delta x^i_{\mathbf{m}} \frac{\partial \psi}{\partial x^i} \, . \tag{D.12}$$

Multiplying this equation with the Jacobian $J_{\mathbf{m}}$ which is given by

$$J_{\mathbf{m}} = |v_\parallel| p^2 \frac{\hat{B}_\varphi(x^1, x^2, \varphi_n)}{B_{min\mathbf{m}}(x^1, x^2)} \, , \tag{D.13}$$

according to [2] defines the source term $\mathcal{Q}_{\mathbf{m}}$

$$\mathcal{Q}_{\mathbf{m}}(\mathbf{u}) = J_{\mathbf{m}} \bar{Q}_{\mathbf{m}}(\mathbf{u}) \, , \tag{D.14}$$

where $\hat{B}_\varphi$ is the physical component of the magnetic field in toroidal direction and $B_{min\mathbf{m}}$ is the module of the magnetic field at the minimum-B cut. From (D.12), (D.13) and (D.14) follows

$$\mathcal{Q}_{\mathbf{m}} = -\Delta x^i_{\mathbf{m}} \frac{\partial \psi}{\partial x^i} |\lambda| \frac{\hat{B}_\varphi(x^1, x^2, \varphi_n)}{B_{min\mathbf{m}}(x^1, x^2)} \frac{p^3}{m} \frac{\partial f_M}{\partial \psi} \, \delta(\psi - \psi_0) \, . \tag{D.15}$$

The source particles have to be uniformly distributed over the poloidal angle ϑ on the flux surface ψ_0. Using cylindrical coordinates $R(\psi, \vartheta)$ and $Z(\psi, \vartheta)$ the distribution $\delta(\psi(\mathbf{x}) - \psi_0)$ can be written as an average over the poloidal angle ϑ

$$\delta(\psi(\mathbf{x}) - \psi_0) = \tag{D.16}$$

$$= \int_{-\pi}^{\pi} \mathrm{d}\vartheta' \, \delta(\psi(\mathbf{x}) - \psi_0) \, \delta(\vartheta(\mathbf{x}) - \vartheta') \tag{D.17}$$

$$= \int_{-\pi}^{\pi} \mathrm{d}\vartheta' \, \delta(x^1 - R(\psi_0, \vartheta')) \, \delta(x^2 - Z(\psi_0, \vartheta')) \left(\frac{\partial(\psi, \vartheta)}{\partial(R, Z)} \right)^{-1} \tag{D.18}$$

$$= 2\pi \, \overline{\delta(x^1 - R(\psi_0, \vartheta')) \, \delta(x^2 - Z(\psi_0, \vartheta'))} \frac{\partial(R, Z)}{\partial(\psi, \vartheta)} \,, \tag{D.19}$$

where

$$\overline{(\ldots)} = \frac{1}{2\pi} \int_{-\pi}^{\pi} \mathrm{d}\vartheta' \, (\ldots) \,. \tag{D.20}$$

The Jacobian $\sqrt{g}$ is given by

$$\sqrt{g} = R \frac{\partial(R, Z, \varphi)}{\partial(\psi, \vartheta, \varphi)} = R \frac{\partial(R, Z)}{\partial(\psi, \vartheta)} \,, \tag{D.21}$$

where R, Z, φ are cylindrical coordinates and ψ, ϑ, φ are straight field line coordinates. Keeping the flux surface label ψ constant one gets from $\mathrm{div}\mathbf{B} = 0$

$$\left(\frac{\partial}{\partial \vartheta} \sqrt{g} B^{\vartheta} + \frac{\partial}{\partial \varphi} \sqrt{g} B^{\varphi} \right)_{\psi} = 0 \tag{D.22}$$

$$\left(\iota \, \frac{\partial}{\partial \vartheta} \sqrt{g} B^{\varphi} + \frac{\partial}{\partial \varphi} \sqrt{g} B^{\varphi} \right)_{\psi} = 0 \,, \tag{D.23}$$

where

$$\frac{\mathrm{d}\vartheta}{\mathrm{d}\varphi} = \frac{B^{\vartheta}}{B^{\varphi}} = \frac{\mathbf{B} \cdot \nabla \vartheta}{\mathbf{B} \cdot \nabla \varphi} = \iota(\psi) \tag{D.24}$$

has been used in the second step. Here, ι is the rotational transform. Equation (D.23) can be written as a total derivative along the field line

$$\frac{\mathrm{d}}{\mathrm{d}\varphi}\sqrt{g}B^{\varphi} = 0\,, \tag{D.25}$$

which suggests

$$\sqrt{g}B^{\varphi} = C(\psi)\,. \tag{D.26}$$

The quantity $C(\psi)$ is constant on the flux surface and can be written as

$$C = \frac{\Delta^2\Phi_t}{\Delta\psi\Delta\vartheta} = \frac{1}{2\pi}\frac{\Delta\Phi_t}{\Delta\psi}\,, \tag{D.27}$$

using (D.21), (D.26) and (D.27) one gets

$$\frac{\partial(R,Z)}{\partial(\psi,\vartheta)} = \frac{1}{2\pi\hat{B}_{\varphi}(x^1,x^2,\varphi_n)}\frac{\mathrm{d}\Phi_t}{\mathrm{d}\psi}\,, \tag{D.28}$$

where $\hat{B}_{\varphi} = RB^{\varphi}$. The source term (D.15) becomes with (D.19) and (D.28)

$$\begin{aligned} \mathcal{Q}_{\mathbf{m}} &= -\Delta x^i_{\mathbf{m}}\frac{\partial\psi}{\partial x^i}\frac{|\lambda|}{B_{min\mathbf{m}}(x^1,x^2)} \\ &\quad\times\overline{\delta(x^1-R(\psi,\vartheta))\delta(x^2-Z(\psi,\vartheta))}\frac{p^3}{m}\frac{\partial f_M}{\partial\psi}\frac{\mathrm{d}\Phi_t}{\mathrm{d}\psi}\,. \end{aligned} \tag{D.29}$$

Assuming that the Maxwellian is depending on ψ only through the particle density n suggests

$$\frac{\partial f_M}{\partial\psi} = \frac{\partial n}{\partial\psi}\frac{\partial f_M}{\partial n} = \frac{\partial n}{\partial r}\frac{\mathrm{dr}}{\mathrm{d}\psi}\frac{f_M}{n}\,. \tag{D.30}$$

The effective radius r associated to a flux surface ψ can be defined according to [119] with the relation between the volume dV enclosed by the flux surface and the area of the flux surface S

$$\mathrm{dr} = \frac{\mathrm{dV}}{S} = \frac{\mathrm{d}\psi}{\langle|\nabla\psi|\rangle}\,, \tag{D.31}$$

where angular brackets denote averages along the field line

$$\langle A\rangle = \lim_{L\to\infty}\left(\int_0^L \frac{\mathrm{d}l}{B}\right)^{-1}\int_0^L \frac{\mathrm{d}l}{B}\,A\,. \tag{D.32}$$

For the following considerations a mono-energetic particle distribution function

$$f_{\mathrm{mono}} = \frac{1}{4\pi}\frac{n}{p_0^2}\,\delta(p-p_0) \tag{D.33}$$

is used instead of a Maxwellian f_M

$$\frac{p^3 f_M}{n} \to \frac{p_0\delta(p-p_0)}{4\pi}\,. \tag{D.34}$$

Using the mono-energetic particle distribution the source term (D.29) becomes with (D.30), (D.31) and (D.34)

$$\mathcal{Q}_{\mathbf{m}} = -\hat{\mathcal{Q}}_{\mathbf{m}}\frac{p_0}{4\pi m}\delta(p-p_0)\frac{1}{\langle|\nabla\psi|\rangle}\frac{\mathrm{d}\Phi_t}{\mathrm{d}\psi}\frac{\partial n}{\partial r}\,, \tag{D.35}$$

where the quantity $\hat{\mathcal{Q}}_{\mathbf{m}}$ is defined as

$$\hat{\mathcal{Q}}_{\mathbf{m}} = \Delta x^i_{\mathbf{m}}\frac{\partial\psi}{\partial x_i}\frac{|\lambda|}{B_{min\mathbf{m}}(x^1,x^2)}\overline{\delta(x^1-R(\psi,\vartheta))\delta(x^2-Z(\psi,\vartheta))}\,, \tag{D.36}$$

and the pseudo scalar flux density $\Gamma_{\mathbf{m}}$ can be written as

$$\Gamma_{\mathbf{m}} = -\hat{\Gamma}_{\mathbf{m}}\frac{p_0}{4\pi m}\delta(p-p_0)\frac{1}{\langle|\nabla\psi|\rangle}\frac{\mathrm{d}\Phi_t}{\mathrm{d}\psi}\frac{\partial n}{\partial r}\,. \tag{D.37}$$

Diffusion coefficient

The particle flux density F_n perpendicular to a flux surface is given by the total particle flux (D.9) divided by the area S of the flux surface

$$F_n = \frac{1}{S}\Gamma_{n\perp} \tag{D.38}$$

$$= \frac{2\pi}{S}\sum_{\mathbf{m}}\int \mathrm{d}^4u\,\Gamma_{\mathbf{m}}(\mathbf{u})\Delta x^i_{\mathbf{m}}\frac{\partial\psi}{\partial x^i}\,. \tag{D.39}$$

The diffusion coefficient D can be written as

$$\begin{aligned} D &= -F_n \left(\frac{\partial n}{\partial r}\right)^{-1} && \text{(D.40)} \\ &= -\left(\frac{\partial n}{\partial r}\right)^{-1} \frac{2\pi}{S} \sum_{\mathbf{m}} \int \mathrm{d}^4 u \Gamma_{\mathbf{m}}(\mathbf{u}) \Delta x^i_{\mathbf{m}} \frac{\partial \psi}{\partial x^i} \,. && \text{(D.41)} \end{aligned}$$

Following [116] the area S of a flux surface ψ within one period is given by

$$S = \frac{2\pi}{N_p} \frac{\langle |\nabla\psi| \rangle}{\langle \mathbf{B} \cdot \nabla\varphi \rangle} \frac{\mathrm{d}\Phi_t}{\mathrm{d}\psi} \,, \tag{D.42}$$

where $\Phi_t = \int \mathrm{d}\mathbf{S} \cdot \mathbf{B}$ is the toroidal flux and N_p denotes the number of field periods. Using $\mathrm{d}l/B = \mathrm{d}\varphi/B^\varphi$ one can write the average in the denominator of (D.42) as

$$\langle \mathbf{B} \cdot \nabla\varphi \rangle = \lim_{L\to\infty} \frac{\int_0^L \frac{\mathrm{d}l}{B} B^\varphi}{\int_0^L \frac{\mathrm{d}l}{B}} = \frac{\int \mathrm{d}\varphi}{\int \frac{\mathrm{d}\varphi}{B^\varphi}} \,. \tag{D.43}$$

For a mono-energetic particle distribution one gets with (D.37) and (D.41)

$$\begin{aligned} D_{\text{mono}} &= \frac{2\pi}{S} \frac{p_0}{4\pi m} \frac{1}{\langle |\nabla\psi| \rangle} \frac{\mathrm{d}\Phi_t}{\mathrm{d}\psi} \\ &\times \sum_{\mathbf{m}} \int \mathrm{d}p \, \delta(p - p_0) \int \mathrm{d}^3 u \hat{\Gamma}_{\mathbf{m}}(\mathbf{u}) \Delta x^i_{\mathbf{m}} \frac{\partial \psi}{\partial x^i} \,. && \text{(D.44)} \end{aligned}$$

After integration over p and substitution of (D.42) one gets

$$D_{\text{mono}} = \frac{p_0 N_p}{4\pi m} \left(\frac{1}{\langle |\nabla\psi| \rangle}\right)^2 \langle \mathbf{B} \cdot \nabla\varphi \rangle \sum_{\mathbf{m}} \int \mathrm{d}^3 u \hat{\Gamma}_{\mathbf{m}}(\mathbf{u}) \Delta x^i_{\mathbf{m}} \frac{\partial \psi}{\partial x^i} \,. \tag{D.45}$$

The diffusion coefficient of the plateau collisionality regime is defined as

$$D_{\text{plateau}} = \frac{\pi v_0^3}{8\sqrt{2}\, \iota \, R_0 \omega_{c0}^2} = \frac{\pi p_0 \rho_L^2}{8\sqrt{2}\, \iota \, R_0 m} \,, \tag{D.46}$$

where the reference velocity v_0, reference momentum p_0, cyclotron frequency ω_{c0} for the reference magnetic field B_0 and Larmor radius ρ_L are given by

$$
\begin{aligned}
v_0 &= \sqrt{\frac{2T}{m}} && \text{(D.47)}\\
p_0 &= \sqrt{2mT} && \text{(D.48)}\\
\omega_{c0} &= \frac{v_0}{\rho_L} && \text{(D.49)}\\
\rho_L &= v_0\frac{mc}{eB_0} = \frac{p_0 c}{eB_0}\,. && \text{(D.50)}
\end{aligned}
$$

Using (D.45) and (D.46) the ratio of the mono-energetic and the plateau diffusion coefficient can be written as

$$
\begin{aligned}
\frac{D_{\text{mono}}}{D_{\text{plateau}}} &= \frac{2\sqrt{2}}{\pi^2}N_p\frac{\iota\!\!\!-R_0}{\rho_L^2}\left(\frac{1}{\langle|\nabla\psi|\rangle}\right)^2\\
&\times \quad \langle\mathbf{B}\cdot\nabla\varphi\rangle\sum_{\mathbf{m}}\int \mathrm{d}^3u\,\hat{\Gamma}_{\mathbf{m}}(\mathbf{u})\Delta x^i_{\mathbf{m}}\frac{\partial\psi}{\partial x^i}\,. && \text{(D.51)}
\end{aligned}
$$

Bootstrap coefficient

According to [86], an equation relating the parallel current density $j_\|$ to the gradient of the pressure p is given by

$$
\frac{\langle j_\| B\rangle}{\langle B^2\rangle} = -\lambda_b\frac{c}{B_0^2}\frac{\partial \mathrm{p}}{\partial r}\,, \qquad \text{(D.52)}
$$

where B is the module of the magnetic field, B_0 is some reference magnetic field and c is the velocity of light. The quantity λ_b is a geometrical factor which is of interest for the investigation of the confinement properties of magnetic field configurations. The brackets denote an average over a spatial volume $\Delta\mathrm{V}$ which is bounded by the flux surfaces ψ and $\psi+\Delta\psi$. The numerator of the left hand side of (D.52) can be written as

$$
\begin{aligned}
\langle j_\| B\rangle &= \frac{1}{\Delta\mathrm{V}}\int\limits_{\Delta\mathrm{V}}\mathrm{d}^3r\, j_\| B && \text{(D.53)}\\
&= \frac{1}{\int_{\Delta\mathrm{V}}\mathrm{d}^3r\,\delta(\psi(\mathbf{r})-\psi_0)}\int\limits_{\Delta\mathrm{V}}\mathrm{d}^3r\,\delta(\psi(\mathbf{r})-\psi_0)\,j_\| B\,, && \text{(D.54)}
\end{aligned}
$$

where the integration $\int_{\Delta \mathrm{V}} \mathrm{d}^3 r$ of a quantity A over the volume $\Delta\mathrm{V}$

$$\Delta \mathrm{V} = \int\limits_0^{2\pi} \mathrm{d}\vartheta \int\limits_0^{2\pi} \mathrm{d}\varphi \int\limits_{\psi}^{\psi+\Delta\psi} \mathrm{d}\psi \, \sqrt{g} \tag{D.55}$$

is defined as

$$\int\limits_{\Delta \mathrm{V}} \mathrm{d}^3 r \, A = \int\limits_0^{2\pi} \mathrm{d}\vartheta \int\limits_0^{2\pi} \mathrm{d}\varphi \int\limits_{\psi}^{\psi+\Delta\psi} \mathrm{d}\psi \, \sqrt{g} \, A \, . \tag{D.56}$$

The parallel current density is given by

$$j_{\|} = e \int \mathrm{d}^3 p \, v_{\|} \, \delta f \, . \tag{D.57}$$

Substituting δf_1 from (D.4) and $j_{\|}$ from (D.57) into (D.54) one gets

$$\begin{aligned} \left\langle j_{\|} B \right\rangle &= \frac{e}{\int \mathrm{d}^3 r \, \delta(\psi(\mathbf{r}) - \psi_0)} \int \mathrm{d}^3 r \int \mathrm{d}^3 p \, \delta f_1 \, B v_{\|} & \text{(D.58)} \\ &= 2\pi e \left(\frac{\mathrm{dV}}{\mathrm{d}\psi} \right)^{-1} \sum_{\mathbf{m}} \int \mathrm{d}p \int \mathrm{d}^3 u \Gamma_{\mathbf{m}}(\mathbf{u}) \, \overline{(B v_{\|})}_{\mathbf{m}} \, , & \text{(D.59)} \end{aligned}$$

where

$$\int \mathrm{d}^3 r \, \delta(\psi(\mathbf{r}) - \psi_0) = \frac{\mathrm{dV}}{\mathrm{d}\psi} \, , \tag{D.60}$$

has been substituted into (D.58). The quantities used in (D.59) are explained in the text after (D.9). The average in (D.59) is given by

$$\overline{(B v_{\|})}_{\mathbf{m}} = \int\limits_0^{\tau_{b\mathbf{m}}} \mathrm{d}\tau \, B v_{\|} \approx \left(\int\limits_0^{\delta l(\lambda)} \mathrm{d}l \, B \right)_{\mathbf{m}} \, . \tag{D.61}$$

According to (D.29), (D.30), (D.31) and (D.36) the source and the pseudo scalar flux density can be written as

$$\begin{aligned}
\mathcal{Q}_{\mathbf{m}} &= -\hat{\mathcal{Q}}_{\mathbf{m}} \frac{1}{m} \frac{p^4}{p_0} \frac{f_M}{n} \frac{1}{\langle|\nabla\psi|\rangle} \frac{\mathrm{d}\Phi_t}{\mathrm{d}\psi} \frac{\partial n}{\partial r} \qquad \text{(D.62)} \\
\hat{\mathcal{Q}}_{\mathbf{m}} &= \frac{p_0}{p} \Delta x^i_{\mathbf{m}} \frac{\mathrm{d}\psi}{\mathrm{d}x_i} \frac{|\lambda|}{B_{min\mathbf{m}}(x^1, x^2)} \\
&\times \overline{\delta(x^1 - R(\psi,\vartheta))\delta(x^2 - Z(\psi,\vartheta))} \qquad \text{(D.63)} \\
\frac{\Gamma_{\mathbf{m}}}{\hat{\Gamma}_{\mathbf{m}}} &= \frac{1}{m} \frac{p^4}{p_0} \frac{f_M}{n} \frac{1}{\langle|\nabla\psi|\rangle} \frac{\mathrm{d}\Phi_t}{\mathrm{d}\psi} \frac{\partial n}{\partial r} \,. \qquad \text{(D.64)}
\end{aligned}$$

Substituting (D.64) into (D.59) leads to

$$\begin{aligned}
\left\langle j_\parallel B \right\rangle &= 2\pi e \left(\frac{\mathrm{dV}}{\mathrm{d}\psi}\right)^{-1} \sum_{\mathbf{m}} \int \mathrm{d}^3 u \hat{\Gamma}_{\mathbf{m}}(\mathbf{u}) \, \overline{(B v_\parallel)}_{\mathbf{m}} \\
&\times \int \mathrm{d}p \frac{1}{m p_0} p^4 \frac{f_M}{n} \frac{1}{\langle|\nabla\psi|\rangle} \frac{\mathrm{d}\Phi_t}{\mathrm{d}\psi} \frac{\partial n}{\partial r} \qquad \text{(D.65)} \\
&= e N_p \left\langle \mathbf{B} \cdot \nabla\varphi \right\rangle \frac{1}{\langle|\nabla\psi|\rangle} \\
&\times \sum_{\mathbf{m}} \int \mathrm{d}^3 u \hat{\Gamma}_{\mathbf{m}}(\mathbf{u}) \, \overline{(B v_\parallel)}_{\mathbf{m}} \int \mathrm{d}p \frac{1}{m p_0} p^4 \frac{\partial f_M}{\partial r} \qquad \text{(D.66)} \\
&= e N_p \left\langle \mathbf{B} \cdot \nabla\varphi \right\rangle \frac{1}{\langle|\nabla\psi|\rangle} \\
&\times \sum_{\mathbf{m}} \int \mathrm{d}^3 u \hat{\Gamma}_{\mathbf{m}}(\mathbf{u}) \, \overline{(B v_\parallel)}_{\mathbf{m}} \frac{1}{2\pi p_0} \frac{\partial}{\partial r} \underbrace{\int \mathrm{d}^3 p \frac{p^2}{2m} f_M}_{\frac{3}{2} n T} \,. \qquad \text{(D.67)}
\end{aligned}$$

From (D.65) to (D.66) the relation

$$\frac{\mathrm{dV}}{\mathrm{d}\psi} = \frac{2\pi}{N_p} \frac{1}{\left\langle \mathbf{B} \cdot \nabla\varphi \right\rangle} \frac{\mathrm{d}\Phi_t}{\mathrm{d}\psi} \,, \tag{D.68}$$

has been used which has been obtained from (D.42) and (D.31). The current coefficient λ_b can be calculated with (D.52) and (D.67)

$$\begin{aligned}\lambda_b &= \frac{e}{c}\frac{B_0^2}{\langle B^2\rangle}N_p\left\langle \mathbf{B}\cdot\nabla\varphi\right\rangle \\ &\times \frac{1}{\langle|\nabla\psi|\rangle}\frac{3}{4\pi p_0}\sum_{\mathbf{m}}\int \mathrm{d}^3u\hat{\Gamma}_{\mathbf{m}}(\mathbf{u})\,\overline{(Bv_\parallel)}_{\mathbf{m}} \qquad \text{(D.69)} \\ &= \frac{3}{4\pi}\frac{B_0N_p}{\rho_L}\frac{\left\langle \mathbf{B}\cdot\nabla\varphi\right\rangle}{\langle B^2\rangle}\frac{1}{\langle|\nabla\psi|\rangle}\sum_{\mathbf{m}}\int \mathrm{d}^3u\hat{\Gamma}_{\mathbf{m}}(\mathbf{u})\,\overline{(Bv_\parallel)}_{\mathbf{m}}\,. \qquad \text{(D.70)}\end{aligned}$$

Making use of $\mathrm{d}l/B = \mathrm{d}\varphi/B^\varphi$, the flux surface averages in this equation can be written as

$$\frac{\left\langle \mathbf{B}\cdot\nabla\varphi\right\rangle}{\langle B^2\rangle} = \lim_{L\to\infty}\frac{\int_0^L \frac{\mathrm{d}l}{B}B^\varphi}{\int_0^L \frac{\mathrm{d}l}{B}}\frac{\int_0^L \frac{\mathrm{d}l}{B}}{\int_0^L \mathrm{d}lB} = \frac{\int_0^L \mathrm{d}\varphi}{\int_0^L \mathrm{d}lB}\,. \qquad \text{(D.71)}$$

Note, that the quantity λ_b is related to the mono-energetic bootstrap current coefficient λ_{bb} according to

$$\lambda_{bb} = \lambda_b\frac{\langle B^2\rangle}{B_0^2}\,. \qquad \text{(D.72)}$$

List of Figures

List of Acronyms

CIEMAT Centro de Investigaciones Energéticas, Medio Ambientales y Tecnológicas, Research Centre for Energy, Environment and Technology, located at Madrid, Spain

CPU Central Processing Unit

LDKE Linearized Drift Kinetic Equation

DKES Drift Kinetic Equation Solver

ECRH Electron Cyclotron Resonance Heating

GSRAKE General Solution of the Ripple Averaged Kinetic Equation

HSX Helically Symmetric Experiment

ICRH Ion Cyclotron Resonance Heating

IPP Institut für PlasmaPhysik der Max-Planck-Gesellschaft, Garching and Greifswald, Germany

LHD Large Helical Device

NBI Neutral Beam Injection

MC Monte Carlo

MPI Message-Passing Interface

NCSX National Compact Stellarator eXperiment

QIPC Quasi-isodynamic stellarator with poloidally closed contours of the magnetic field strength

Stellarator	STELLA geneRATOR, star generator in Latin
TJ-II	Torus JEN II
TOKAMAK	TOroidal'naya KAmera s MAgnitnymi Katushkami, toroidal chamber with magnetic coils in Russian
W7-AS	Wendelstein 7-Advanced Stellarator,
W7-X	Wendelstein 7-X

Bibliography

[1] K. Allmaier, S. V. Kasilov, W. Kernbichler, and G. O. Leitold. Variance reduction in computations of neoclassical transport in stellarators using a δf method. *Phys. Plasmas*, 15:072512–1–072512–9, 2008.

[2] S. V. Kasilov, W. Kernbichler, V. V. Nemov, and M. F. Heyn. Mapping technique for stellarators. *Phys. Plasmas*, 9(8):3508–3525, 2002.

[3] M. Sasinowski and A. H. Boozer. A δf Monte Carlo method to calculate plasma currents. *Phys. Plasmas*, 2(3):610–619, 1995.

[4] M. Sasinowski and A. H. Boozer. A δf Monte Carlo method to calculate plasma parameters. *Phys. Plasmas*, 4(10):3509–3517, 1997.

[5] W. X. Wang, N. Nakajima, M. Okamoto, and S. Murakami. A new δf method for neoclassical transport studies. *Plasma Phys. Control. Fusion*, 41:1091–1108, 1999.

[6] J. D. Williams and A. H. Boozer. δf method to calculate plasma transport and rotation damping. *Phys. Plasmas*, 10(1):103–111, 2003.

[7] M. Yu. Isaev, S. Brunner, W. A. Cooper, T. M. Tran, A. Bergmann, C. D. Beidler, J. Geiger, H. Maaßberg, J. Nührenberg, and M. Schmidt. VENUS+δf: A bootstrap current calculation module for 3-D configurations. *Fusion Science and Technology*, 50(3):440–446, 2006.

[8] S. E. Parker and W. E. Lee. A fully nonlinear characteristic method for gyrokinetic simulation. *Phys. Fluids B*, 5(1):77–86, 1993.

[9] Y. Chen and R. B. White. Collisional δf method. *Phys. Plasmas*, 4(10):3591–3598, 1997.

[10] Y. Chen and S. E. Parker. A δf particle method for gyrokinetic simulations with kinetic electrons and electromagnetic perturbations. *J. Comput. Phys.*, 189(2):463–475, 2003.

[11] W. Kernbichler, S.V. Kasilov, G.O. Leitold, V.V. Nemov, and K. Allmaier. Computation of neoclassical transport in stellarators with finite collisionality. In *15th International Stellarator Workshop, Madrid, 3–7 October, 2005*, pages P2–15. International Stellarator Workshop, 2005. to be published.

[12] W. Kernbichler, S. V. Kasilov, G. O. Leitold, V. V. Nemov, and K. Allmaier. Computation of neoclassical transport in stellarators using the full linearized coulomb collision operator. In F. De Marco and G. Vlad, editors, *33rd EPS Conference on Plasma Physics, Rome, 19–23 June 2006*, volume 30I of *ECA*, pages P–2.189. European Physical Society, 2006.

[13] K. Allmaier, S. V. Kasilov, W. Kernbichler, G. O. Leitold, and V. V. Nemov. Variance reduction in computations of neoclassical transport in stellarators using a δf method. In P. Gąsior and J. Wołowski, editors, *34th EPS Conference on Plasma Physics, Warsaw, Poland, July 2-6, 2007*, volume 31F of *ECA*, pages P–4.041. European Physical Society, 2007.

[14] K. Allmaier, S. V. Kasilov, W. Kernbichler, G. O. Leitold, and V. V. Nemov. Computations of neoclassical transport in stellarators using a δf method with reduced variance. In *16th International Stellarator/Heliotron Workshop 2007, Toki, Japan, 15–19 October, 2007*, pages P2–021. International Stellarator/Heliotron Workshop, 2007.

[15] K. Allmaier, C. D. Beidler, M. Yu. Isaev, S. V. Kasilov, W. Kernbichler, H. Maaßberg, S. Murakami, D. A. Spong, and V. Tribaldos. ICNTS - Benchmarking of bootstrap current coefficients. In *16th International Stellarator/Heliotron Workshop 2007, Toki, Japan, 15–19 October, 2007*, pages P2–029. International Stellarator/Heliotron Workshop, 2007.

[16] W. Kernbichler, S. V. Kasilov, G. O. Leitold, V. V. Nemov, and K. Allmaier. Recent progress in NEO-2 - A code for neoclassical transport computations based on field line tracing. In *16th International Stellarator/Heliotron Workshop 2007, Ceratopia Toki, Japan, 15–19 October 2007*, pages P2–022. International Stellarator/Heliotron Workshop, 2007.

[17] K. Allmaier, S. V. Kasilov, W. Kernbichler, and G. O. Leitold. δf Monte Carlo computations of neoclassical transport in stellarators with reduced variance. In *35th EPS Conference on Plasma Phys. Hersonissos, 9 - 13 June 2008*, volume 32D of *ECA*, pages P–4.017. European Physical Society, 2008.

[18] W. Kernbichler, S. V. Kasilov, G. O. Leitold, V. V. Nemov, and K. Allmaier. Recent progress in NEO-2 - A code for neoclassical transport computations based on field line tracing. *Plasma and Fusion Research*, 3:S1061–1–S1061–4, 2008.

[19] J. L. Velasco, K. Allmaier, W. Kernbichler, and F. Castejón. Calculation of the bootstrap current profile for the stellarator TJ-II. In C. McKenna, editor, *37th EPS Conference on Plasma Physics, Dublin, Ireland, June 21-25, 2010*, volume 34A of *ECA*, page P1.1099. European Physical Society, 2010.

[20] J. L. Velasco, J. M. García-Regaña, F. Castejón, K. Allmaier, A. Cappa, W. Kernbichler, N. B. Marushchenko, and M. Tereshchenko. Electron Bernstein driven and bootstrap current estimations in the TJ-II stellarator. In *23rd IAEA Fusion Energy Conference, Daejon, Korea Rep. of, 11-16 October 2010*, pages THW/P7–16, 2010.

[21] C. D. Beidler, K. Allmaier, M. Yu. Isaev, S. V. Kasilov, W. Kernbichler, G. O. Leitold, H. Maaßberg, D. R. Mikkelsen, S. Murakami, M. Schmidt, D. A. Spong, V. Tribaldos, and A. Wakasa. Benchmarking Results From the International Collaboration on Neoclassical Transport in Stellarators ICNTS. *Nucl. Fusion*, 51:076001–1–076001–28, 2011.

[22] J. L. Velasco, K. Allmaier, A. López-Fraguas, C. D. Beidler, H. Maaßberg, W. Kernbichler, and F. Castejón. Calculation of the

bootstrap current profile for the stellarator TJ-II. *Plasma Phys. Control. Fusion*, 53(11):115014–1–115014–16, 2011.

[23] K. Allmaier, S. V. Kasilov, and W. Kernbichler. Delta f monte carlo computations of parallel conductivity in stellarators. In *38th EPS Conference on Plasma Physics, Strasbourg, France, June 27th - July 1st, 2011*, volume 35G of *ECA*, page P1.112. European Physical Society, 2011.

[24] H. Maaßberg, W. Lotz, and J. Nührenberg. Neoclassical bootstrap current and transport in optimized stellarator configurations. *Phys. Fluids B*, 5(10):3728–3736, 1993.

[25] T. C. Hender, J. L. Cantrell, J. H. Harris, B. A. Carreras, V. E. Lynch J. F. Lyon, J. A. Fabregas, J. Guasp, A. López-Fraguas, and A. P. Navarro. Studies of a flexible heliac configuration. *Fusion Technol.*, 13:521–535, 1988.

[26] L. Spitzer, Jr. A proposed stellarator. U. S. Atomic Energy Commission Report No. NYO–993 (PM–S–1), 1951.

[27] L. Spitzer, Jr. The stellarator concept. *Phys. Fluids*, 1(4):253–264, 1958.

[28] http://physics.ucc.ie/∼pjm/trachtais_macleinn/
HughCallaghanPhD1999/node7.html
called at 17.04.2015.

[29] http://buon.fjfi.cvut.cz/fttf/evergreen/IPP_SU2007_script.pdf
called at 17.04.2015.

[30] http://www.uni-saarland.de/fak7/fze/AKE_Archiv/DPG2011-
AKE_Dresden/Vortraege/DPG2011_AKE4.2Wolf_Stellarator.pdf
called at 17.04.2015.

[31] http://www.uni-saarland.de/fak7/fze/AKE_Archiv/DPG2013-
AKE_Dresden/Buch/DPG2013_AKE1.2_Klinger_OptimizedStellarator_p19.pdf
called at 21.04.2015.

[32] https://www.dpg-physik.de/veroeffentlichung/ake-
tagungsband/tagungsband-ake-2013.pdf called at 17.04.2015.

[33] https://www.ipp.mpg.de/2523775/konzeptentwicklung called at 31.03.2015.

[34] A. Dinklage, T. Klinger, G. Marx, and L. Schweikhard, editors. *Plasma Physics. Confinement, Transport and Collective Effects.* Lecture Notes in Physics. Springer, Berlin Heidelberg, 2005.

[35] D. D.-M. Ho and R. M. Kulsrud. Neoclassical transport in stellarators. *Phys. Fluids*, 20(2):442–461, 1987.

[36] S. Hamada. Hydromagnetic equilibria and their proper coordinates. *Nucl. Fusion*, 2:23–37, 1962.

[37] J. M. Greene and J. L. Johnson. Stability criterion for arbitrary hydromagnetic equilibria. *Phys. Fluids*, 5(5):510–517, 1962.

[38] A. H. Boozer. What is a stellarator? *Phys. Plasmas*, 5(5):1647–1655, 1998.

[39] W. D. D'haeseleer, W. N. G. Hitchon, J. D. Callen, and J. L. Shohet. *Flux coordinates and magnetic field structure.* Springer Series in Computational Physics. Springer-Verlag, Berlin Heidelberg, 1991.

[40] A. I. Morozov and L. S. Solov'ev. The structure of magnetic fields. In Acad. M. A. Leontovich, editor, *Reviews of Plasma Physics*, volume 2, pages 1–101. Consultants Bureau, New York, 1966.

[41] S. P. Hirshman and D. J. Sigmar. Neoclassical transport of impurities in tokamak plasmas. *Nucl. Fusion*, 21(9):1079–1201, 1981.

[42] R. Balescu. *Transport processes in plasmas*, volume 2. Neoclassical transport theory. Elsevier Science, North-Holland, New York, 1988.

[43] K. C. Shaing and J. D. Callen. Boundary layer corrections to neoclassical ripple transport in tokamaks. *Phys. Fluids*, 25(6):1012–1019, 1982.

[44] K. C. Shaing, S. P. Hirshman, and J. S. Tolliver. Parallel viscosity-driven neoclassical fluxes in the banana regime in nonsymmetric toroidal plasmas. *Phys. Fluids*, 29(8):2548–2555, 1986.

[45] K. C. Shaing, S. P. Hirshman, and J. D. Callen. Neoclassical transport fluxes in the plateau regime in nonaxisymmetric toroidal plasmas. *Phys. Fluids*, 29(2):521–526, 1986.

[46] K. C. Shaing and J. D. Callen. Neoclassical flows and transport in nonaxisymmetric toroidal plasmas. *Phys. Fluids*, 26(11):3315–3326, 1983.

[47] http://www-users.york.ac.uk/∼bd512/teaching/media/mcf_lecture_06.pdf called at 16.03.2015.

[48] J. Geiger. Theoretical Modeling in Preparation of Wendelstein 7-X. In *14th European Fusion Theory Conference, Frascati, Italy, 26th - 29th September, 2011*, 2011.

[49] H. Wobig. Theory of advanced stellarators. *Plasma Phys. Control. Fusion*, 41:A159–A173, 1999.

[50] C. D. Beidler et al. In *Plasma Phys. Control Fusion Res. (Proc. 9th Int. Conf. Montreal, 1982) vol III (Vienna: IAEA)*, page 129, 1983.

[51] http://www.physics.ucla.edu/icnsp/Html/spong/w7x_with_coils.JPG called at 23.04.2015.

[52] R. Wolf. Operational limits in stellarators. Heraeus Seminar, Bad Honnef, 2013. http://www.iek-yig.de/531stweh/talks/i5_1_wolf.pdf called at 21.04.2015.

[53] C. D. Beidler, E. Harmeyer, F. Herrenegger, J. Kisslinger, Y. Igitkhanov, and H. Wobig. Stellarator fusion reactors – an overview. In *Toki Conf. ITC12*, 2001.

[54] http://www.ipp.mpg.de/44224/3_stellaratoren.pdf called at 14.04.2015.

[55] C. Gourdon, D. Marty, and E. K. Maschke et al. Configurations du type stellarator avec puit moyen et cisaillement des lignes magnetiques. In *Proc. of the 3rd IAEA Conference on Plasma Physics and Controlled Nuclear Fusion Research, vol 1, IAEA, Vienna 1969*, pages 847–861, 1969.

[56] http://www.ipf.uni-stuttgart.de/lehre/plasmaphys/p80_07.html called at 14.04.2015.

[57] S. Rehker and H. Wobig. A stellarator coil system without helical windings. In *Proc. of the 7th Symposium on Fusion Technology (SOFT-Grenoble) (Commission of the European Communities General Directorate for Dissimination of Knowledge for Information and Documentation, Luxembourg 1972)*, pages 345–357, 1972.

[58] J. Nührenberg and R. Zille. Stable stellarators with medium β and aspect ratio. *Phys. Lett. A*, 114(3):129–132, 1986.

[59] C. Beidler, G. Grieger, F. Herrnegger, E. Harmeyer, J. Kißlinger, W. Lotz, H. Maaßberg, P. Merkel, J. Nührenberg, F. Rau, J. Sapper, F. Sardei, R. Scardovelli, A. Schlüter, and H. Wobig. Physics and engineering design for Wendelstein 7-X. *Fusion Technol.*, 17:148–168, 1990.

[60] http://www.ipp.mpg.de/9792/stellarator called at 16.04.2015.

[61] R. D. Hazeltine and F. L. Waelbroeck. *The Framework of Plasma Physics*. Perseus Books, Reading, Massachusetts, 1998.

[62] R. Balescu. *Transport processes in plasmas*, volume 1. Classical transport theory. Elsevier Science, North-Holland, New York, 1988.

[63] A. A. Galeev and R. Z. Sagdeev. Theory of neoclassical diffusion. In Acad. M. A. Leontovich, editor, *Reviews of Plasma Physics*, volume 7, page 257. Consultants Bureau, New York - London, 1979.

[64] L. M. Kovrizhnykh. Neoclassical theory of transport processes in toroidal magnetic confinement systems, with emphasis on non-axisymmetric configurations. *Nucl. Fusion*, 24(7):851–936, 1984.

[65] F. L. Hinton and R. D. Hazeltine. Theory of plasma transport in toroidal confinement systems. *Rev. Mod. Phys.*, 48(2):239–308, 1976.

[66] S. P. Hirshman, K. C. Shaing, W. I. van Rij, C. O. Beasley, Jr., and E. C. Crume, Jr. Plasma transport coefficients for nonsymmetric toroidal confinement systems. *Phys. Fluids*, 29(9):2951–2959, 1986.

[67] P. Helander and D. J. Sigmar. *Collisional Transport in Magnetized Plasmas*. Cambridge Monographs on Plasma Physics. Cambridge University Press, 2002.

[68] R. J. Bickerton, J. W. Connor, and J. B. Taylor. Diffusion driven plasma currents and bootstrap tokamak. *Nature Physical Science*, 229:110–112, 1971.

[69] A. A. Galeev. Diffusion-electrical phenomena in a plasma confined in a tokamak machine. *Sov. Phys. JETP*, 32(4):752, 1971.

[70] M. C. Zarnstorff and S. C. Prager. Experimental observation of neoclassical currents in a plasma. *Phys. Rev. Lett.*, 53(5):454–457, 1984.

[71] K. C. Shaing, E. C. Crume, Jr., J. S. Tolliver, S. P. Hirshman, and W. I. van Rij. Bootstrap current and parallel viscosity in the low collisionality regime in toroidal plasmas. *Phys. Fluids B*, 1(1):148–152, 1989.

[72] K. C. Shaing, B. A. Carreras, N. Dominguez, V. E. Lynch, and J. S. Tolliver. Bootstrap current control in stellarators. *Phys. Fluids B*, 1(8):1663–1670, 1989.

[73] N. Nakajima and M. Okamoto. Neoclassical flow, current, and rotation in general toroidal systems. *Journal of The Physical Society of Japan*, 61(3):833–843, 1992.

[74] S. Nishimura and H. Sugama. Bootstrap current coefficients in stellarators. *J. Plasma Fusion Res. SERIES*, 6:437–441, 2004.

[75] A. G. Peeters. The bootstrap current and its consequences. *Plasma Phys. Control. Fusion*, 42:B231–B242, 2000.

[76] M. Kikuchi and M. Azumi. Experimental evidence for the bootstrap current in a tokamak. *Plasma Phys. Control. Fusion*, 37:1215–1238, 1995.

[77] K. Y. Watanabe, N. Nakajima, M. Okamoto, K. Yamazaki, Y. Nakamura, and M. Wakatani. Effect of collisionality and radial electric field on bootstrap current in the large helical device. *Nucl. Fusion*, 35(3):335–345, 1995.

[78] A. S. Ware, D. A. Spong, L. A. Berry, S. P. Hirshman, and Lyon J. F. Bootstrap Current in Quasi-Symmetric Stellarators. *Fusion Science and Technology*, 50(2):236–244, 2006.

[79] M. Murakami, B. A. Carreras, L. R. Baylor, G. L. Bell, T. S. Bigelow, A. C. England, J. C. Glowienka, H. C. Howe, T. C. Jernigan, D. K. Lee, V. E. Lynch, C. H. Ma, D. A. Rasmussen, J. S. Tolliver, M. R. Wade, J. B. Wilgen, and W. R. Wing. Bootstrap-current experiments in a toroidal plasma-confinement device. *Phys. Rev. Lett.*, 66(6):707–710, 1991.

[80] A. H. Boozer and H. J. Gardner. The bootstrap current in stellarators. *Phys. Fluids B*, 2(10):2408–2421, 1990.

[81] M. N. Rosenbluth, R. D. Hazeltine, and F. L. Hinton. Plasma transport in toroidal confinement systems. *Phys. Fluids*, 15(1):116–140, 1972.

[82] A. A. Galeev and R. Z. Sagdeev. Transport phenomena in a collisionless plasma in a toroidal magnetic system. *Sov. Phys. JETP*, 26(1):233–240, 1968.

[83] https://www.euro-fusion.org/wpcms/wp-content/uploads/2011/09/jg05-537-4c-960x511.jpg called at 23.04.2015.

[84] R. B. White. *The Theory of Toroidally Confined Plasmas.* Imperial College Press, second edition, 2001.

[85] Masahiro Wakatani. *Stellarator and heliotron devices.* Oxford University Press, New York & Oxford, 1998.

[86] S. V. Kasilov, V. V. Nemov, W. Kernbichler, and M. F. Heyn. Evaluation of the parallel current density in a stellarator using the integration technique along the magnetic field line. In K. Szegö,

T. N. Todd, and S. Zoletnik, editors, *27th EPS Conference on Contr. Fusion and Plasma Phys., Budapest, 12–16 June 2000*, volume 24B of *ECA*, pages 668–671. The European Physical Society, 2000.

[87] M. Taguchi. A method for calculating neoclassical transport coefficients with momentum collision operator. *Phys. Fluids B*, 4(11):3638–3643, 1992.

[88] H. Sugama and S. Nishimura. How to calculate the neoclassical viscosity, diffusion, and current coefficients in general toroidal plasmas. *Phys. Plasmas*, 9(11):4637–4653, 2002.

[89] H. Maaßberg, C. D. Beidler, and Y. Turkin. Momentum correction techniques for neoclassical transport in stellarators. *Phys. Plasmas*, 16:072504–1–072504–15, 2009.

[90] Y. Chen and S. E. Parker. Electromagnetic gyrokinetic δf particle-in-cell turbulence simulation with realistic equilibrium profiles and geometry. *J. Comput. Phys.*, 220(2):839–855, 2007.

[91] Y. Chen and S. E. Parker. Coarse-graining phase space in δf particle-in-cell simulations. *Phys. Plasmas*, 14(8):082301–1–082301–9, 2007.

[92] A. M. Dimits and B. I. Cohen. Collision operators for partially linearized particle simulation codes. *Phys. Rev. E*, 49(1):709, 1994.

[93] Z. Lin, W. M. Tang, and W. W. Lee. Gyrokinetic particle simulation of neoclassical transport. *Phys. Plasmas*, 2(8):2975–2988, 1995.

[94] Z. Lin, W. M. Tang, and W. W. Lee. Neoclassical transport in enhanced confinement toroidal plasmas. *Phys. Rev. Lett.*, 78(3):456–459, 1997.

[95] S. Brunner, E. Valeo, and J. A. Krommes. Collisional delta-f scheme with evolving background for transport time scale simulations. *Phys. Plasmas*, 6(12):4504–4521, 1999.

[96] S. Brunner, E. Valeo, and J. A. Krommes. Linear delta-f simulations of nonlocal electron heat transport. *Phys. Plasmas*, 7(7):2810–2823, 2000.

[97] G. Hu and J. A. Krommes. Generalized weighting scheme for δf particle-simulation method. *Phys. Plasmas*, 1(4):863–874, 1994.

[98] H. Qin, R. C. Davidson, and E. A. Startsev. Weight growth due to resonant simulation particles and a modified δf algorithm with smooth switching between δf and total-f methods. *Phys. Plasmas*, 15(6):063101–1–063101–7, 2008.

[99] A. H. Boozer and G. Kuo-Petravic. Monte Carlo evaluation of transport coefficients. *Phys. Fluids*, 24(5):851–859, 1981.

[100] http://research.cs.wisc.edu/htcondor called at 28.01.2015.

[101] O. Motojima, N. Ohyabu, A. Komori, O. Kaneko, H. Yamada, K. Kawahata, Y. Nakamura, K. Ida, T. Akiyama, N.Ashikawa, W.A. Cooper, A. Ejiri, M. Emoto, N. Ezumi, H. Funaba, A. Fukuyama, P. Goncharov, M. Goto, H. Idei, K. Ikeda, S. Inagaki, M. Isobe, S. Kado, H. Kawazome, K. Khlopenkov, T. Kobuchi, K. Kondo, A. Kostrioukov, S. Kubo, R. Kumazawa, Y. Liang, J.F. Lyon, A. Mase, S. Masuzaki, T. Minami, J. Miyazawa, T. Morisaki, S. Morita, S. Murakami, S. Muto, T. Mutoh, K. Nagaoka, Y. Nagayama, N. Nakajima, K. Nakamura, H. Nakanishi, K. Narihara, Y. Narushima, K. Nishimura, N. Nishino, N. Noda, T. Notake, H. Nozato, S. Ohdachi, Y. Oka, H. Okada, S. Okamura, M. Osakabe, T. Ozaki, B.J. Peterson, A. Sagara, T. Saida, K. Saito, S. Sakakibara, M. Sakamoto, R. Sakamoto, M. Sasao, K. Sato, M. Sato, T. Seki, T. Shimozuma, M. Shoji, H. Suzuki, Y. Takeiri, N. Takeuchi, N. Tamura, K. Tanaka, M.Y. Tanaka, Y. Teramachi, K. Toi, T. Tokuzawa, Y. Tomota, Y. Torii, K. Tsumori, K.Y. Watanabe, T.Watari, Y. Xu, I. Yamada, S. Yamamoto, T. Yamamoto, M. Yokoyama, S. Yoshimura, Y. Yoshimura, M. Yoshinuma, N. Asakura, T. Fujita, T. Fukuda, T. Hatae, S. Higashijima, A. Isayama, Y. Kamada, H. Kubo, Y. Kusama, Y. Miura, T. Nakano, H. Ninomiya, T. Oikawa, N. Oyama, Y. Sakamoto, K. Shinohara, T. Suzuki, H. Takenaga, K. Ushigusa, T. Hino,

M. Ichimura, Y. Takase, F. Sano, H. Zushi, T. Satow, S. Imagawa, T. Mito, I. Ohtake, T. Uda, K. Itoh, K. Ohkubo, S. Sudo, K. Yamazaki, K. Matsuoka, Y. Hamada, and M. Fujiwara. Recent advances in the LHD experiment. *Nucl. Fusion*, 43:1674 – 1683, 2003.

[102] S. Murakami, A. Wakasa, H. Maaßberg, C.D. Beidler, H. Yamada, K.Y. Watanabe, and LHD Experimental Group. Neoclassical transport optimization of LHD. *Nucl. Fusion*, 42:L19–L22, 2002.

[103] G. Grieger, W. Lotz, P. Merkel, J. Nührenberg, J. Sapper, E. Strumberger, H. Wobig, the W7-X Team, R. Burhenn, V. Erckmann, U. Gasparino, L. Giannone, H. J. Hartfuss, R. Jaenicke, G. Kühner, H. Ringler, A. Weller, F. Wagner, and the W7-AS Team. Physics optimization of stellarators. *Phys. Fluids B*, 4(7):2081–2091, 1992.

[104] G. Grieger, C. Beidler, E. Harmeyer, W. Lotz, J. Kißlinger, P. Merkel, J. Nührenberg, F. Rau, E. Strumberger, and H. Wobig. Modular stellarator reactors and plans for Wendelstein 7-X. *Fusion Technol.*, 21:1767–1778, 1992.

[105] M. C. Zarnstorff, L. A. Berry, A. Brooks, E. Fredrickson, G. Y. Fu, S. Hirshman, S. Hudson, L. P. Ku, E. Lazarus, D. Mikkelsen, D. Monticello, G. H. Neilson, N. Pomphrey, A. Reiman, D. Spong, D. Strickler, A. Boozer, W. A. Cooper, R. Goldston, R. Hatcher, M. Isaev, C. Kessel, J. Lewandowski, J. F. Lyon, P. Merkel, H. Mynick, B. E. Nelson, C. Nuehrenberg, M. Redi, W. Reiersen, P. Rutherford, R. Sanchez, J. Schmidt, and R. B. White. Physics of the compact advanced stellarator NCSX. *Plasma Phys. Control. Fusion*, 43:A237–A249, 2001.

[106] F. S. B. Anderson, A. F. Almagri, D. T. Anderson, P. G. Matthews, J. N. Talmadge, and J. L. Shohet. *Fusion Technol.*, 27:273, 1995.

[107] S. Gori and J. Nührenberg. Quasi-isodynamic stellarators with magnetic well and positive shear. In *Theory of Fusion Plasmas*, Editrice Compositori, Bologna, pages 473–480. Proceedings of the Joint Varenna-Lausanne International Workshop, 1998, 1999.

[108] A. A. Subbotin, M. I. Mikhailov, V. D. Shafranov, M. Yu. Isaev, C. Nührenberg, J. Nührenberg, R. Zille, V. V. Nemov, S. V. Kasilov, V. N. Kalyuzhnyj, and W. A. Cooper. Integrated physics optimization of a quasi-isodynamic stellarator with poloidally closed contours of the magnetic field strength. *Nucl. Fusion*, 46:921–927, 2006.

[109] W. Kernbichler, S. V. Kasilov, G. Kapper, A. F. Martitsch, V. V. Nemov, C. Albert, and M. F. Heyn. Solution of drift kinetic equation in stellarators and tokamaks with broken symmetry using the code NEO-2. *Plasma Phys. Control. Fusion*, 58:104001, 2016.

[110] C. D. Beidler, W. N. G. Hitchon, and J. L. Shohet. “hybrid” monte carlo simulation of ripple transport in stellarators. *J. Comput. Phys.*, 72:220–242, 1987.

[111] V. Tribaldos. Monte Carlo estimation of neoclassical transport for the TJ-II stellarator. *Phys. Plasmas*, 8(4):1229–1239, 2001.

[112] W. I. van Rij and S. P. Hirshman. Variational bounds for transport coefficients in three-dimensional toroidal plasmas. *Phys. Fluids B*, 1(3):563–569, 1989.

[113] C. D. Beidler and W. D. D’haeseleer. A general solution of the ripple-averaged kinetic equation. *Plasma Phys. Control. Fusion*, 37:463–490, 1995.

[114] C. Grebogi and R. G. Littlejohn. Relativistic ponderomotive Hamiltonian. *Phys. Fluids*, 27(8):1996–2004, 1984.

[115] A. I. Morozov and L. S. Solov’ev. Motion of charged particles in electromagnetic fields. In Acad. M. A. Leontovich, editor, *Reviews of Plasma Physics*, volume 2, pages 201–297. Consultants Bureau, New York, 1966.

[116] V. V. Nemov. The second adiabatic invariant and neoclassical transport in stellarators. *Phys. Plasmas*, 6(1):122–129, 1999.

[117] W. Kernbichler, V. V. Nemov, S. V. Kasilov, and M. F. Heyn. Evaluation of $1/\nu$ transport and parallel current density in stellarators using the integration technique along the magnetic field

line. In *Problems of Atomic Science and Technology*, volume 6, pages 8–12, 2000.

[118] W. Kernbichler, S. V. Kasilov, V. V. Nemov, G. Leitold, and M. F. Heyn. Neoclassical transport calculations for optimization studies. In *13th International Stellarator Workshop, Canberra, Feb 25 – Mar 1, 2002, Paper No. OV.9*, 2002.

[119] V. V. Nemov, S. V. Kasilov, W. Kernbichler, and M. F. Heyn. Evaluation of $1/\nu$ neoclassical transport in stellarators. *Phys. Plasmas*, 6(12):4622–4632, 1999.